*Advances in Physics*
Vol. 00, No. 00, Month-Month 200x, 1–148

arXiv:cond-mat/0609650v1 [cond-mat.stat-mech] 26 Sep 2006

# Statistical Models of Fracture

Mikko J. Alava[1], Phani K. V. V. Nukala[2], and Stefano Zapperi[3]

*(Received 00 Month 200x; In final form 00 Month 200x)*

Disorder and long-range interactions are two of the key components that make material failure an interesting playfield for the application of statistical mechanics. The cornerstone in this respect has been lattice models of the fracture in which a network of elastic beams, bonds or electrical fuses with random failure thresholds are subject to an increasing external load. These models describe on a qualitative level the failure processes of real, brittle or quasi-brittle materials. This has been particularly important in solving the classical engineering problems of material strength: the size dependence of maximum stress and its sample to sample statistical fluctuations. At the same time, lattice models pose many new fundamental questions in statistical physics, such as the relation between fracture and phase transitions. Experimental results point out to the existence of an intriguing crackling noise in the acoustic emission and of self-affine fractals in the crack surface morphology. Recent advances in computer power have enabled considerable progress in the understanding of such models. Among these partly still controversial issues, are the scaling and size effects in material strength and accumulated damage, the statistics of avalanches or bursts of microfailures, and the morphology of the crack surface. Here we present an overview of the results obtained with lattice models for fracture, highlighting the relations with statistical physics theories and more conventional fracture mechanics approaches.

[1] Laboratory of Physics,Helsinki University of Technology, FIN-02015 HUT, Finland

[2] Computer Science and Mathematic Division, Oak Ridge National Laboratory, Oak Ridge, TN 37831-6164, USA

[3] CNR-INFM, Dipartimento di Fisica, Università "La Sapienza", P.le A. Moro 2 00185 Roma, Italy

## Table of contents

1. Introduction 3
2. Elements of fracture mechanics 6
   2.1. Theory of linear elasticity 6
   2.2. Cracks in elastic media 8
   2.3. The role of disorder on material strength 11
   2.4. Extreme statistics for independent cracks 12
   2.5. Interacting cracks and damage mechanics 14
   2.6. Fracture mechanics of rough cracks 17
3. Experimental background 23
   3.1. Strength distributions and size effects 24
   3.2. Rough cracks 27
   3.3. Acoustic emission and avalanches 35
   3.4. Time-dependent fracture and plasticity 39
4. Statistical models of failure 42
   4.1. Random fuse networks: brittle and plastic 43
   4.2. Tensorial models 50
   4.3. Discrete Lattice versus Finite Element Modeling of fracture 52
   4.4. Dynamic effects 56
   4.5.Atomistic simulations 61
5. Statistical theories for fracture models 63
   5.1. Fiber bundle models 64
   5.2. Statistical mechanics of cracks: fracture as a phase transition 71
   5.3. Crack depinning 78
   5.4. Percolation and fracture 81
6. Numerical simulations 89
   6.1. The I-V characteristics and the damage variable 91
   6.2. Damage Distribution 95
   6.3. Fracture strength 107
   6.4. Crack roughness 114
   6.5. Avalanches 118
7. Discussion and outlook 121
   7.1. Strength distribution and size effects 124
   7.2. Morphology of the fracture surface: roughness exponents 126
   7.3. Crack dynamics: avalanches and acoustic emission 127
   7.4. From discrete models to damage mechanics 128
   7.5. Concluding remarks and perspectives 128

   Appendix: Algorithms 129
   References 140

## 1 Introduction

Understanding how materials fracture is a fundamental problem of science and engineering even today, although the effects of geometry, loading conditions, and material characteristics on the strength of materials have been empirically investigated from antique times. Probably the first systematic mathematical analysis of the problem dates back to the pioneering works of Leonardo da Vinci [1] and Galileo Galilei [2]. In Leonardo's notebooks one finds an interesting description of a tension test on metal wires [1]. Attaching a slowly filling sand bag to an end of the wire, Leonardo noticed that longer wires failed earlier (see Fig. 1). A simple analysis based on continuum mechanics, however, would suggest that wires of the same section should carry the same stress and hence display equal strength. This lead some later commentators to hypothesize that when Leonardo wrote *smaller length*, what he really meant was *larger diameter* [3]. As noted in Ref. [4], there is a simpler explanation: continuum mechanics treats the material as homogeneous, but this is often very far from the truth, especially for metal wires forged in the Renaissance. Disorder has profound effects on material strength, since fracture typically nucleates from weaker spots like preexisting microcracks or voids. The longer the wire, the easier it is to find a weak spot, hence the strength will decrease with length.

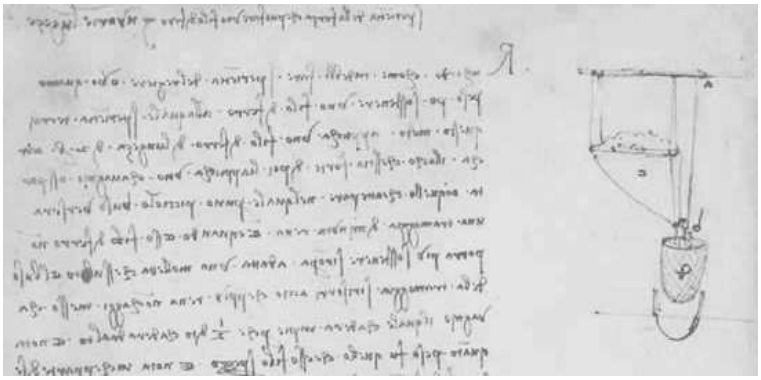

Figure 1. The setup devised by Leonardo da Vinci to test the strength of metal wires. One end of the wire is suspended and the other end is attached to a basket that was slowly filled with sand. When the wire breaks, one can weigh the sand collected in the basket, determining the strength. From the original notebook [1].

What we have just described is probably the first experimental verification of size effect in fracture. Size effects are rooted in disorder and hence necessitates a statistical treatment. In particular, different samples of the same material could generally be expected to display fluctuations in the strength. The importance of defects and fluctuations in fracture was first realized in the early twenties by the work of Griffith [5] and later formalized from the

statistical point of view by Weibull [6]. An excellent discussion of the history of strength up to the middle of the twentieth century can be found in the book by Timoshenko [7]. At present the importance of a statistical treatment in determining the strength of materials is certainly widely accepted, but despite this fact standard textbooks on fracture mechanics devote little attention to this problem. In addition experimental evaluations of strength distribution and other statistical properties are relatively scarce in the literature.

Besides the engineering aspects of the problem, in the last twenty years the statistical properties of fracture have attracted a wide interest in the statistical physics community [8–10]. In this context, fracture can be seen as the outcome of the irreversible dynamics of a long-range interacting, disordered system. Several experimental observations have revealed that fracture is a complex phenomenon, described by scale invariant laws [11]. Examples notably include the acoustic emission measured prior to fracture and the roughness of the fracture surface. The observation of scaling makes it attractive to discuss breakdown processes in terms of statistical mechanics and in particular to search for analogies with phase transitions and critical phenomena. These give rise to probability distributions that bear resemblance with the empirical observations on fracture, in particular "power-law" ones.

The statistical physics approach to fracture is often based on numerical simulation of lattice models, which allow for a relatively simple description of disorder and elasticity. The elastic medium is represented by a network of springs or beams. The disorder is modeled for instance by imposing random failure thresholds on the springs or by removing a fraction of the links. In this way the model retains the long range nature and the tensorial structure of the interactions. The local displacements can then be found by standard method for solving coupled linear equations. The lattice is loaded imposing appropriate boundary conditions and the fracture process can be followed step by step, in a series of quasi-equilibria. The cornerstone in this respect has been for the last twenty years the Random Fuse Network (or Model, RFM) [12], a lattice model of the fracture of solid materials in which as a further key simplification vectorial elasticity has been substituted with a scalar field.

As damage accumulates, one observes intriguing *history effects*: in brittle failure, microcracks grow via the failure of the weakest elements [6]. In ductile fracture, dislocations or plastic deformation accumulates, and in viscoelastic materials there is a variety of complex relaxation mechanisms of stress in addition to irreversible failure. Meanwhile, the stress field evolves and develops a more and more inhomogeneous structure. This arises in the simplest case from microcrack interactions that can shield each other or act jointly to enhance the local stress at various points in the material.

In addition to numerical simulations, lattice models are useful to obtain new theoretical ideas and approaches to the problem. The aim is to develop a

probabilistic description of fracture involving the interplay between "frozen" properties, such as microcracks, and "thermal" noise. The former is independent of time, quenched into a sample and is only affected by whatever external influences the sample is subjected to and their internal consequences (consider growing microcracks). The thermal noise comes from environmental effects and the coarse-grained fluctuations at the atomistic level. In this respect, so-called fiber bundle models represent a useful idealization and the basis for more complex theoretical developments [13,14]. The exactly solvable global load sharing model can be seen as a mean-field version of the RFM. As it is customary with phase transitions and critical phenomena, mean-field theory provides a qualitative picture of the transition. In general, however, for elastic, brittle failure the critical stress is ruled by the behavior of the extremal values of the stress distribution, the highest stress(es) present in any sample. This means that the highest moments of the distribution are crucial, contrary to what happens for other macroscopic properties such as the elastic moduli, which depend only on average mean-field quantities. One should be aware of this problem when trying to extend the results of fiber bundle models to more realistic cases.

At a more application-oriented level, network models provide a valid alternative to standard finite element calculations, especially in cases where structural disorder and inhomogeneities are particularly strong [15]. For instance, models of this kind are extensively used to model concrete [16–20]. This approach can be relevant for the predictability of structural failure, the design of stronger materials and optimization of structural composition.

The scope of this review is to present an introduction to statistical models of fracture. At the same time, the goal is to provide an overview of the current understanding gained with this approach. After at least twenty years of intense research in the subject, we feel the need for a summarizing work, complementing the early insight gained in the past with more reliable results obtained by large scale simulations, which became possible due to recent advances in computer power and novel computational algorithmic techniques. This allows to clarify some controversial issues, such as the scaling in the damage dynamics, the avalanches or bursts of microfailures, and the scaling of the fracture surface in lattice models. The access to better data and experimental progress has also created new unsolved problems. This work gives us thus an opportunity to outline both experimental and theoretical prospects. A research path that will not be pursued here is that of dielectric breakdown [21], which has many parallels with the RFM and the role of disorder is likewise important (see e.g. [9, 22]).

The review is organized as follows: a brief introduction to elasticity and fracture mechanics is reported in Sec. 2. While this does not represent by any means an exhaustive account of this very extended field, it has the primary purpose to set the formalism and the basic notation to be used in the fol-

lowing. In Sec. 3 we discuss the experimental background that motivates the introduction of statistical models of fracture. Thus particular attention will be devoted to those aspects that call for a statistical approach, such as the strength distributions and the related size effects, the crack roughness, and the acoustic emission. In Sec. 4 we proceed with a detailed description of network models for fracture, starting from the scalar RFM up to more complex beam models. We will highlight the connections with standard finite elements methods and atomistic calculations and discuss dynamic effects. This complements the main emphasis here, of general theories and scaling laws by pointing out what issues are left out on purpose from the models at hand.

The main theoretical approaches are reviewed in Sec. 5 starting from fiber bundle models as an illustration. We next discuss the general properties of phase transitions and point out the connections for fracture. Finally, we discuss the role of disorder in fracture model and introduce percolation concepts. Sect. 6 is devoted to a discussion of recent simulation results. We report results for the constitutive behavior, fracture strength and damage distributions, size effects, damage localization, crack roughness and avalanches. The discussion section (Sec. 7) outlines current challenges and possible future trends. An Appendix includes a description of the main numerical algorithms.

## 2 Elements of fracture mechanics

Fracture mechanics describes the formation and propagation of cracks in terms of macroscopic field equations, starting from the theory of linear elasticity. It is not our aim to review here the broad field of linear elastic fracture mechanics (LEFM). We provide only a short summary of the main concepts defining the basic terminology to be used in the following sections. In addition, we present a general discussion of the role of disorder in fracture.

### 2.1 *Theory of linear elasticity*

The theory of linear elasticity describes the small deformations of solid bodies under the action of external forces. Consider a solid at rest and parameterize it by a set of coordinates $\vec{r}$. Assuming that there is a direct relation between the coordinates $\vec{r'}$ of the deformed solid with those of the undeformed solid, we define the displacement field as $\vec{u} \equiv \vec{r}\,' - \vec{r}$. It is then convenient to introduce the the symmetric *strain tensor* as

$$\epsilon_{ik} \equiv \frac{1}{2}\left(\frac{\partial u_i}{\partial x_k} + \frac{\partial u_k}{\partial x_i}\right). \tag{1}$$

When a solid deforms under the action of external forces, interactions at the molecular scale provide restoring forces that tend to bring the solid back to its reference configuration. Each of the material particles of the solid is in equilibrium under the action of both internal force interactions and external applied forces. Since all the internal forces should cancel each other due the action-reaction principle, when the equilibrium of a volume element $dV$ is considered, we are left only with surface tractions that act on the surface $dS$ that contains the volume element $dV$ and externally applied body forces (such as gravity) that act over the volume element $dV$. In other words, the only non-vanishing contribution to the force should come from the tractions applied at the surface $dS$ and the external body forces that act over volume $dV$. Thus the external force vector $\mathbf{F}$ with components $\mathbf{F}_i$ is given by

$$\mathbf{F}_i = \int_V \mathbf{b}_i dV + \int_S \mathbf{t}_i dS \tag{2}$$

where $\mathbf{b}_i$ are the components of body forces per unit volume, and $\mathbf{t}_i$ are the components of the surface tractions (force per unit surface area). By notation, the bold symbols refer to vector or tensor quantities. Based on Cauchy's hypothesis, the surface tractions are given by $\mathbf{t}_i = \mathbf{n}_j \sigma_{ij}$, where $\mathbf{n}$ is the unit outward normal to the surface $dS$ and $\sigma$ is the Cauchy stress tensor with components $\sigma_{ij}$. Using the divergence theorem, Eq. 2 can be written as $\mathbf{F} = \int_V [\mathbf{b} + \nabla \cdot \sigma] \, dV$ (where $\nabla$ is the gradient operator), and in component form as

$$\mathbf{F}_i = \int_V \mathbf{b}_i dV + \int_V \sum_j \frac{\partial \sigma_{ij}}{\partial \mathbf{x}_j} \tag{3}$$

The equilibrium condition for the body implies $\mathbf{F} = \mathbf{0}$, which in terms of the stress tensor can be written as

$$\sum_j \frac{\partial \sigma_{ij}}{\partial \mathbf{x}_j} + \mathbf{b}_i = 0. \tag{4}$$

When the body forces $\mathbf{b}$ are absent, Eq. 4 reduces to

$$\sum_j \frac{\partial \sigma_{ij}}{\partial \mathbf{x}_j} = 0. \tag{5}$$

In the limit of small deformations, there is a linear relation between stress

and strain

$$\sigma_{ij} = \sum_{k,l} \mathbf{C}_{ijkl} \epsilon_{kl}, \tag{6}$$

where $\mathbf{C}_{ijkl}$ is the elastic moduli tensor. Eq. (6) is the most general linear expression relating the strain and the stress tensor, but it becomes much simpler in the case of isotropic media:

$$\mathbf{C}_{ijkl} = \lambda \delta_{ij} \delta_{kl} + \mu(\delta_{ik}\delta_{jl} + \delta_{il}\delta_{jk}) \tag{7}$$

where the parameters $\lambda$ and $\mu$ are known as Lamè coefficients, and $\delta_{ij} = 1$ when $i = j$ and is 0 otherwise. It is often convenient to write the strain tensor as the sum of a compressive strain, involving a volume change, and a shear strain, which does not imply any volume changes. Then the Hooke laws can be written as

$$\sigma_{ij} = K\delta_{ij} \sum_k \epsilon_{kk} + 2\mu(\epsilon_{ij} - \frac{1}{3}\delta_{ij} \sum_k \epsilon_{kk}). \tag{8}$$

where $K$ is the bulk modulus and $\mu$ is the shear modulus. Finally, another standard formulation of the Hooke law involves the Young modulus $E \equiv \frac{9K\mu}{\mu+3K}$ and the Poisson ratio $\nu \equiv \frac{1}{2}\left(\frac{3K-2\mu}{3K+\mu}\right)$

$$\sigma_{ij} = \frac{E}{(1+\nu)} \left( \epsilon_{ij} + \frac{\nu}{1-2\nu} \delta_{ij} \sum_k \epsilon_{kk} \right). \tag{9}$$

The equation for stress equilibrium for an isotropic elastic medium can be written, combining the Hooke law with Eq. (5), in terms of the displacement field $\vec{u}$ the Lamé coefficients $\lambda$ and $\mu$ as

$$(\lambda + \mu)\vec{\nabla}(\vec{\nabla} \cdot \vec{u}) + \mu \nabla^2 \vec{u} = 0, \tag{10}$$

with appropriate boundary conditions. Note that we have used both $\vec{()}$ notation and the bold face notation interchangeably to denote a vector quantity.

### 2.2 *Cracks in elastic media*

In mathematical terms, a crack can be seen as a boundary condition for the elastic strain field, with the additional complication that the precise shape of

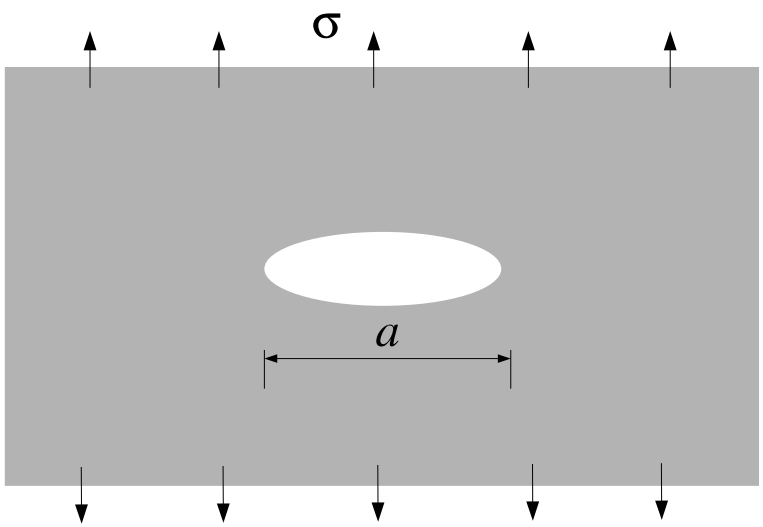


Figure 2. An elliptic crack in a two dimensional medium.

the crack is in principle unknown, and the shape depends on the stress field acting on it. To overcome this formidable problem, one can prescribe the crack geometry and then compute the stress field. This approximation can provide a useful guidance on the mechanism of crack propagation.

A simple illustrative example of this procedure is provided by the solution of the stress field around an elliptic crack placed under tensile stress in an infinite two dimensional medium (see Fig. 2). The solution of the elastic equation of equilibrium yields for instance the stress concentration at the edge of the ellipse

$$K_T \equiv \frac{\sigma_{max}}{\sigma} = 1 + \frac{2a}{b}. \tag{11}$$

where $\sigma$ is the nominal applied stress and $\sigma_{max}$ is the maximum stress, and $a$ and $b$ are major and minor radii of the ellipse. In reality cracks are not elliptical but typically display a sharp tip. If we rewrite Eq. (11) in terms of the curvature radius $\rho \equiv b^2/a$, we see that $K_T$ diverges as $1/\sqrt{\rho}$ as $\rho \to 0$, and hence the concept of stress concentration becomes useless.

It was first shown by Irwin that the stress around a crack tip follows

$$\sigma_{ij} = \frac{K_T}{\sqrt{2\pi r}} f_{ij}(\theta, \phi) \tag{12}$$

where $K_T$ is the *stress intensity factor* and $f_{ij}$ is a crack-tip function in terms of the angular variables $\theta$ and $\phi$. The particular values of $K_T$ and the func-

tional forms of $f_{ij}$ depend on the particular loading conditions (i.e. the way stress is applied to the body). In this respect, it is convenient to identify three fracture modes (see Fig. 3) corresponding to tensile (I), shear (II) and tearing (III) conditions (i.e., $K_T$ equals $K_I$ in mode I, $K_{II}$ in mode II, and $K_{III}$ in mode III). A generic loading rule can typically be split into an appropriate combination of the three modes. The presence of singularity around the crack tip, however, is an artifact of linear elasticity. Real materials can not sustain arbitrarily large stresses and in general close to the crack tip deformation is ruled by non-linear and inelastic effects. In practice it is customary to define a fracture process zone (FPZ) as the region surrounding the crack where these effects take place, while far enough from the crack one recovers linear elastic behavior, that is the long-range decay of perturbed displacement fields.

Knowing the stress field around a crack does not tell us directly how the fracture process would develop, but this information is necessary to build a model. A simple and clear argument to understand the stability of a crack was provided by Griffith almost a century ago [5]. The idea is to compute the energy needed to open a crack and see when this process becomes favorable. Considering for simplicity a two dimensional geometry, the elastic energy change associated with a crack of length $a$ is given by

$$E_{el} = \frac{-\pi\sigma^2 a^2}{2E}, \tag{13}$$

where $\sigma$ is the applied stress. Forming a crack involves the rupture of atomic bonds, a process that has an energy cost proportional to the crack surface

$$E_{surf} = 2a\gamma, \tag{14}$$

where $\gamma$ is the surface tension. Griffith noted that a crack will grow when this process leads to a decrease of the total energy $E = E_{el} + E_{surf}$. Thus the criterion for crack growth can be expressed as

$$\frac{dE}{da} = -\pi\sigma^2 a/E + 2\gamma < 0, \tag{15}$$

which implies that under a stress $\sigma$ cracks of size $a > a_c \equiv 2\gamma E/(\pi\sigma^2)$ are unstable. Equation (15) can also be written as $\sigma\sqrt{\pi a} > \sqrt{2E\gamma}$ and, noting that $K = \sigma\sqrt{\pi a}$ is the stress intensity factor of an infinite plate, we can reformulate the crack growth criterion in terms of a critical stress intensity factor $K_c \equiv \sqrt{2E\gamma}$, also known as the material toughness (i.e. the crack grows when $K > K_c$).

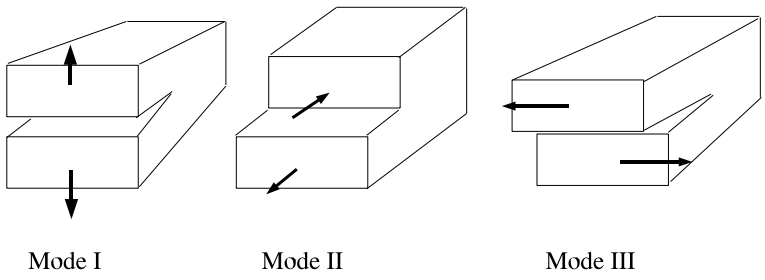


Figure 3. The three modes of fracture.

### 2.3 *The role of disorder on material strength*

The influence of randomness on fracture can have many disguises. It is useful to leave aside inelastic effects for awhile, and consider only brittle or "quasi-brittle" processes. In this case, we can generalize the discussion of section 2.2, using the concepts of long-range elastic fields, critical energy or crack size. There are several independent subcases that present different physics: one may consider a single crack and analyze the effect of disorder on material strength or, alternatively, one could study the dynamics of a whole crack population. In general, we can identify some key issues to address:

(i) what is the effect of disorder on the stability of a single crack, and how does the Griffith argument get modified?
(ii) in the presence of many cracks, how is the physics changed from the case of a single crack?
(iii) what is the effect of disorder on the propagation of a single crack?
(iv) what are the concepts, and statistical laws that operate in the case of many cracks of which no single one dominates over the others?

These four fundamental questions also touch upon a number of engineering mechanics and materials science issues, such as fracture toughness, crack arrest, defect populations, damage mechanics, and failure prediction.

The first two issues from the above list deal with *size scaling* and the statistics of strength. Figure 4 illustrates the schematic advancement of a two-dimensional crack from a pre-existing flaw (or a notch in a test). The presence of variation in the material structure can be presented ideally - in brittle materials - by locally varying elastic moduli, so that the stress-field becomes more complicated than the homogeneous LEFM solution. It can also be seen as a crack surface energy $\gamma_s(\vec{x})$ which has a fluctuating component. The issue of size effects amounts to computing the strength of a sample of linear size $L$. The answer of course depends on whether the sample has one dominating crack or more number of microcracks or flaws.

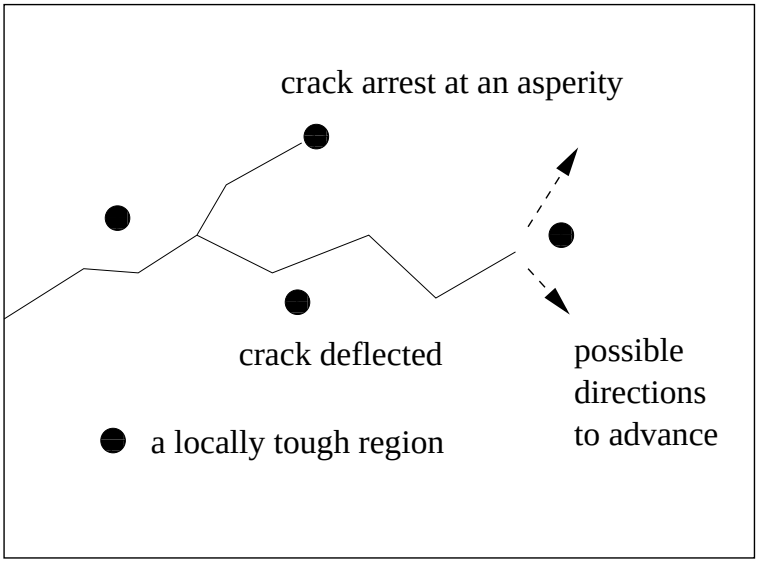


Figure 4. One-dimensional example of a crack propagating in a disordered environment. Included are crack arrest due to strong regions, deflection, branching and wandering.

In the case of a single dominating defect, the Griffith argument can be easily modified to account for a spatial variation of the elastic coefficients. The technical problem is to consider the distributions of the surface energy $\gamma_s$ and elastic modulus $E$, or, even the presence of dislocations in the sample. As a result, one gets instead of the deterministic critical crack length (for constant $E$ and $\gamma_s$) a probability for the crack to be stable under a given external stress. In other words, we can characterize the problem by a *strength distribution* which in the case of a single crack crucially depends on the microscopic randomness. For instance, Arndt and Nattermann [23] showed that an uncorrelated random $\gamma_s$ results in an exponential strength distribution. In general, however, $\gamma_s$ could also display spatial correlations, as measured by the two point correlator $\langle \gamma_s(\vec{x})\gamma_s(\vec{y})\rangle$, where the brackets denote a statistical average. Correlations in $\gamma_s$ imply that an increased crack opening will cost energy that not only depends on $\gamma_s$ at a single location but also depends on the presence of such correlations.

### 2.4 *Extreme statistics for independent cracks*

In the presence of many non-interacting defects, it becomes apparent that the physics is related to *extreme statistics* (see Fig. 5). The simplest starting point is to find the largest defect - or the most dangerous one - in the system. Later on in the context of random fuse networks we will return to this argument in

more detail. If the critical crack fails instantaneously, there is no pre-critical crack growth, and the cracks do not interact, then this is a sufficient condition for determining the statistical strength properties. In other words, we want to consider a dilute gas of non-interacting defects, and find the worst one using a Lifshitz type argument [6].

Consider a collection of $N_d$ defects, and assign to each of these a failure strength $\sigma_i$, where $i = 1, \ldots, N_d$. The whole sample fails if one of these defects can not stand the applied stress. Thus for the cumulative strength distribution $F(\sigma, N_d)$ one has that

$$1 - F(\sigma) = \prod_{i=1}^{N_d} [1 - P_i(\sigma)] \,. \tag{16}$$

If the cracks are independent so that $\sigma_i$ are random variables distributed according to $P_i = P(\sigma)$, then it follows that

$$1 - F(\sigma) \simeq \exp[-V\rho P(\sigma)] \tag{17}$$

where $\rho$ is the crack density and $V$ the sample volume. The crucial ingredients here are the $P(\sigma)$ and $N_d$ since they rule both the asymptotic form of the distribution $F$ as well as its form for finite $N_d$. Of these two issues, more interesting is the behavior of $F(\sigma)$ in the large $N_d$ limit. Then, the question boils down to the actual distribution of the $P(\sigma)$. For narrow distributions, one has the *Gumbel* scaling form

$$F(\sigma) \sim 1 - \exp\left[-V \exp p(\sigma)\right] \tag{18}$$

where the function $p(\sigma)$ follows from $P(\sigma)$ and depends on two things: the stress enhancement factor of a typical defect of linear size $l$, and the size distribution $P(l)$ of the defects. For example, an exponential $P(l)$ will thus result in this *Gumbel* scaling form.

The other possibility is to use a distribution $P(l)$ that makes the local stresses at crack tips to have a wide distribution as well. Using a length distribution $P(l) \sim l^{-g}$ changes the limiting distribution of the sample strength to a Weibull distribution. The reason is simple: assuming that the stress $\sigma$ at the crack tips grows as a power of crack length $l$, then the $P(\sigma)$ also becomes a power law distribution since $P(l)$ is a power law distribution. As a result, the celebrated Weibull distribution [6] (or its 3-parameter version) arises:

$$F(\sigma) \sim 1 - \exp\left(-V\sigma^m / A^m\right) \tag{19}$$

where $A$ is a normalization constant, and $m$ is the Weibull modulus, which

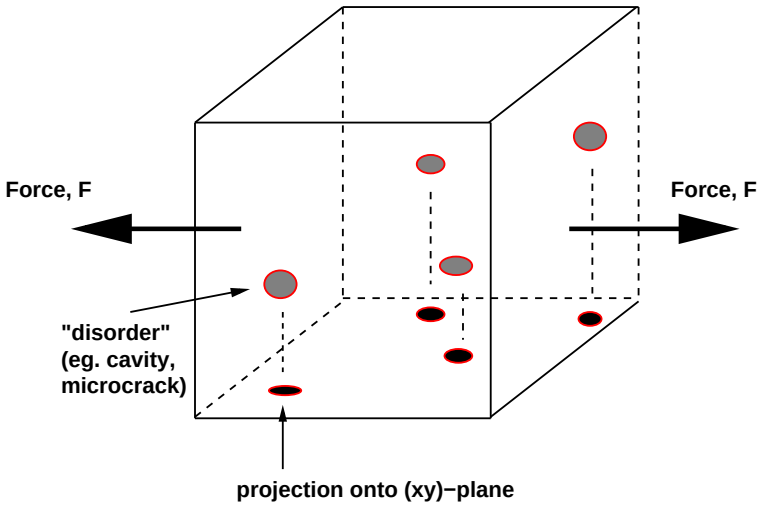


Figure 5. An example of a dilute defect population. These cracks each of some size $l$ are assumed in the simplest case to have no influence on each other, and they have a linear size distribution $P(l)$.

can be related to the strength of a defect of size $l$. In particular, we have that if $\sigma \sim l^{-1/2}$ then $m = 2g$. As usual, a small $m$ implies a heterogeneous material/sample as $g$ is then small as well. In any case, the distributions Eqs. (18), (19) allow now to distinguish between microscopic details in experiments, and predict the size-scaling of average strength. The Gumbel-form is apt to give a logarithmic size-effect, but note that this is only true in the absence of notches or dominating defects (see Sec. 6.3.3).

### 2.5 *Interacting cracks and damage mechanics*

The discourse on strength changes character if one allows for slow *average* crack growth. Here, we would like to focus on the case in which the fracture dynamics is continuous and slow, so that in spite of possibly very fast local developments, a sample can be considered in a quasi-equilibrium. This means that the sample internal state is either independent of time or evolves slowly with respect to the fast time-scale of the fracture process. Even in these conditions, treating explicitly the dynamics of interacting microcracks represents a formidable task: the growth of a microcrack can be either inhibited/screened or accelerated due to the presence of a neighboring microcrack. The outcome in general depends on the loading conditions, the crack geometry and other details, as discussed in the engineering mechanics literature.

To avoid all these complications, one can disregard the dynamics of individual microcracks and treat the damage at a coarse grained scale. This approach, known as "damage mechanics" [17,24,25], is valid when the interaction among

cracks is moderate. In the simplest case, one can consider the evolution of a scalar valued damage field $D(\vec{x})$, describing the local variations of the Hooke law

$$\sigma(\vec{x}) = E_0(1 - D(\vec{x}))\epsilon. \tag{20}$$

The idea behind damage mechanics is that all the complications of the fracture process can be encoded in the field $D$, that will then evolve according to a prescribed law, reflecting the internal microcracking in the material.

Simple models of statistical fracture can be used to check some of the typical assumptions and possible outcomes in damage mechanics. This is in particular applicable in "scalar fracture", described by the electrical analogue of the RFM. In order to apply the coarse-graining procedure, implied by Eq. (20), one assumes the presence of a length-scale over which the damage self-averages, meaning that its fluctuations become much smaller than the average. This scale is also known as the Representative Volume Element (RVE) above which it is possible to treat the damage as a smoothly varying variable.

Figure 5 depicts the typical scenario for damage accumulation. In this example we imagine a set of microcracks that will grow in a stable manner, and give rise to locally enhanced "damage" $D(\vec{x})$. One may now naturally define a *correlation length*, by measuring e.g. the two-point correlation function of a scalar $D$ via

$$C_D(\vec{r}) = \langle((D(\vec{x}+\vec{r}) - \langle D\rangle) - (D(\vec{x}) - \langle D\rangle))^2\rangle \tag{21}$$

which should decay, for a field $D$ which is uncorrelated over longer distances, asymptotically exponentially and thus defines a correlation length $\xi$ via $C_D \sim \exp(-r/\xi)$. An interesting issue is the "symmetry breaking" in damage accumulation: the direction of crack growth is mostly dictated by geometry and loading conditions. Thus, as illustrated by Fig. 5, it is necessary to consider separately the directions perpendicular and parallel to the external stress, which would then imply *two correlation lengths*, $\xi_\parallel$ and $\xi_\perp$.

Given a fracture process, in which damage grows in a controlled fashion one can then - in principle, at least in simulations - follow the development of $\xi$. This quantity will increase, making a sample effectively "smaller": as $\xi$ (and the RVE size ) increases $L/\xi$ diminishes, where $L$ is as usual the sample linear size. An additional complication comes from the damage anisotropy, since the two correlation lengths $\xi_\perp$ and $\xi_\parallel$ will follow different dynamics.

It is interesting to discuss what happens when one of the two becomes much larger than the other. In this case the sample becomes effectively much "larger" along the stress direction, becoming almost one-dimensional, which in other words indicates the presence of *damage localization*. The developments that

lead to and beyond this point are of course an interesting issue, with also materials science twists. Consider for instance the mechanics of fiber-reinforced composites: eventually one crack will dominate, but still the specimen may have a finite strength remaining thanks to fibers that bridge the crack and induce cohesion.

In general, it is a complicated question as to what kind of evolution would rule $\langle D \rangle$, even if the possibly very important role of fluctuations is neglected. That is, as the $\xi$ increases the damage inside the corresponding RVE should fluctuate more and more. Recall also the connection between $D$ and the sample effective elastic modulus, which implies that the two follow similar dynamics. One can postulate several possible scenarios for the damage dynamics, including so-called "finite-time singularities" (see e.g. [26, 27]). These imply a divergence of the strain under a linearly growing applied stress $\sigma \propto t$

$$\epsilon \sim 1/(t_c - t)^{\gamma}, \tag{22}$$

i.e. a power-law -like or pseudo-critical approach to the failure time $t_c$ and to the corresponding critical stress $\sigma_c \propto t_c$. In the context of damage mechanics, Eq. (22) would result from a stress dependent damage law of the type $1 - D \sim (\sigma_c - \sigma)^{\gamma}$. In cases with a dominant crack this law can be related to the crack growth rate as a function of $\sigma$. Another possibility is that the damage displays an abrupt jump at $\sigma_c$. The two possibilities are depicted in Fig. 6.

The statistical laws and geometry of damage accumulation can be studied both via laboratory experiments and the models that are the main scope of this review, and they often have also great importance for engineering applications. The typical engineering mechanics viewpoint of the previous discussion is to look at the rate of crack growth given just a single crack. The assumption is that the crack length $a$ evolves according to

$$\frac{\partial a}{\partial t} = A K_{eff}^{m} \tag{23}$$

where $K_{eff}$ is an effective stress intensity factor and the exponent $m$ typically varies between 30 and 50 [28]. Eq. (23), known as the "Charles law", is a way of generalizing the standard LEFM expression, in Eq. (12), for which $K_{eff} \sim a^{1/2}$. It implies that even a subcritical crack, in the sense of the Griffith argument, can slowly grow in some conditions such as creep or fatigue. Examples arise in non-brittle fracture, and in the presence of a diffuse crack population [29]. For $K_{eff} \sim L$ one gets a power-law growth in time by simple integration [30]. The possible roles of disorder here is a question which has not been studied systematically.

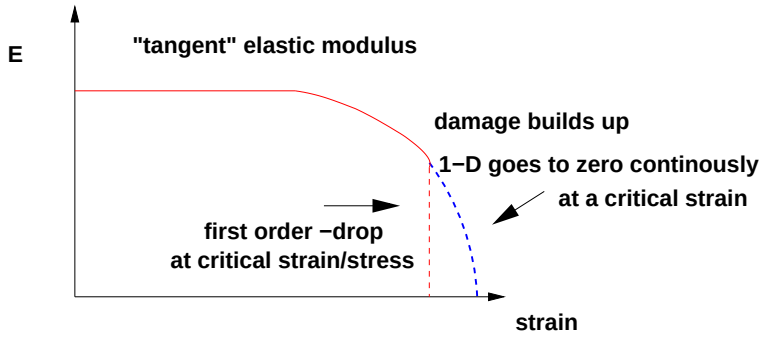


Figure 6. An example of a "first-order" and a critical scenario for damage build-up, via $E_{eff} = ED(\epsilon)$

.

### 2.6 *Fracture mechanics of rough cracks*

**2.6.1** ***Crack dynamics in a disordered environment: self-affinity and anomalous scaling.*** While damage mechanics treats fracture in disordered media at a coarse grained scale, it is often necessary to treat the dynamics of a single macroscopic crack. A simple example is to consider a medium containing regions with sufficiently high $\gamma_s$, locally, so as to stop crack growth. In these circumstances energetic considerations dictate that the crack path will deviate from the straight direction (see Fig. 4). The simple case is the two-dimensional one, when the vertical coordinate of the crack tip, $h(t)$, (where $t$ is the position along the horizontal projection of the crack path) wanders with equal probability up and down. This process corresponds directly to a random walk or Brownian motion. This fact implies that the crack surface, corresponding to the trajectory of the crack tip, displays a characteristic *roughness*. In the following we consider the fracture surfaces $\vec{h}(\vec{x}, t)$ in various cases. The following sub-cases can be distinguished:

(i) **2D crack**: the crack line grows as a *trail* of a zero-dimensional point-like particle, the effective crack point. For example, consider the growth of a crack from a pre-made notch.

(ii) **3D interfacial crack**: a crack line propagates in a plane $(xy)$, so that the $z$-direction can be neglected. If the average direction of propagation is in the $y$-direction, say, one is interested in the statistics of the rough line $h(x, \bar{y})$ where $\bar{y}$ is the time-dependent average position, and $h$ varies with $x$, in the $y$-direction.

(iii) **3D crack**: one has a crack line given by $\vec{r}(t)$. This leaves a trail as the time increases, which is a two-dimensional surface $h(x, y)$ where $h$ is along the $z$-axis. In general, $h$ is defined only for those $(x, y)$ for which the projection of $\vec{r}$ on the $xy$-plane, $((x', y'))$, is such that that for $x = x'$, $y' > y$. One

may now study the projections of $h$ to the $(xy)$- and $((xz))$-planes, defining thus the two components $h_{\parallel}(x,\bar{y})$ and $h_{\perp}(x,\bar{y})$ which lie in the respective planes.

The geometry of rough surfaces becomes particularly interesting when it turns out that they are self-affine fractals, or even more complicated versions thereof as discussed below. There are three core questions related to this kind of "roughening", in addition to the phenomenology of exponents and scaling relations, and the origins of such scaling:

- What are the the smallest length- (and time-) scales on which one can see such behavior?
- What is the largest scale, that of "saturation", where the roughness becomes independent of scale? What leads to the saturation, in particular if one is concerned about the microstructure?
- How does the roughness evolve? A crack is often induced in the laboratory from a notch, which is "flat". The roughness of the crack will develop as new crack surface is created. Thus one must be careful in considering a posteriori surfaces from experiment or simulations.

Let us now study the separate possibilities. Of these, case (ii) from above is conceptually the easiest one. Assume that the crack front advances on average with a constant velocity $v$, so that $\bar{y} = vt$. The simplest quantity used to characterize the roughness is the global surface width

$$W(L,t) = (\langle (h(x,t) - vt)^2 \rangle_x)^{1/2} \tag{24}$$

which simply measures the standard deviation around the mean position. The global width is a quantity often considered in kinetic roughening of surfaces, for instance in molecular-beam epitaxy or in the propagation of slow combustion fronts in paper. In these cases, it happens that the dynamics of $h(x,t)$ is ruled by a Langevin equation and one can expect the so-called Family-Vicsek-scaling [31]. This implies the presence of an unique spatial scale, the correlation length $\xi$, and an associated time-scale. In practice one writes

$$W(L,t) \sim t^{\beta} f(L/t^{1/z}). \tag{25}$$

Eq. (25) describes the roughening of $h$ from an initial condition, which is usually a flat one, although one can also consider the influence of an arbitrary profile $h(x, t = 0)$. The initial transient is governed by the growth exponent $\beta$, until correlations build up, as $\xi$ reaches $L$, and the roughness saturates at the value $W \sim L^{\zeta}$. This implies that the scaling function $f(x)$ is a constant, except for $x$ small. The self-affine scaling relates now $\beta$, $\zeta$, and the dynamic

exponent $z$ through

$$\beta z = \zeta. \tag{26}$$

Note that one can have further constraints, such as the so-called Galileian invariance for the Langevin equation, coupling the exponents ($2 - 1/\beta = \zeta$ in 2D).

If we consider separately the profiles $h_{\parallel}(x, \bar{y})$ and $h_{\perp}(x, \bar{y})$ (again, one may substitute $\bar{y} = vt$), in the simplest imaginable case, the Family-Vicsek picture applies to both, separately, with six separate exponents $\beta_{\parallel}$, $z_{\parallel}$, $\zeta_{\parallel}$, and $\beta_{\perp}$, $z_{\perp}$, $\zeta_{\perp}$, respectively, that are coupled by the relation Eq. 26. In section 5.3, we overview line models of cracks, according to scenario (iii), such that they might relate to this scenario.

The existence of a correlation length begs the question of where it stems from in the crack growth dynamics, or in other words if one measures the exponents experimentally what is the equation underlying the roughening process. This is apparent if we consider the generalization of the one-dimensional example of a Brownian "crack" trail to case (iii), which is the most relevant for experiments. The idea is to represent the opening of a crack by a moving one-dimensional line which leaves a two-dimensional surface $h(x, y)$ trailing after itself. Thus in the intermediate fracture stage one has a line separating the untouched part and the crack - with two open faces. Considering the case slow fracture, one could then write equations of motion for the fluctuating components of the crack line, taking into account the pertinent physics as the presence of randomness, and the coupling due to elasticity of the fluctuations, both in-plane and out-of-plane. Such an approach also contains the idea that the physics in the bulk, as in the fracture process zone, can be neglected or incorporated again as a long-range elasticity along the crackline. Similar models that include further complications such as dynamical overshoots along the crack front have also been studied to a great extent (see section 5.3).

Scalings such as that implied by Eq. (25) are to be understood in the average sense. That is, one has to sample the stochastic process sufficiently in order to ensure the convergence of quantities. This is naturally a problem in fracture, where it may be difficult to collect enough samples. There are other measures that can be used to extract the exponents, such as the local width, the correlation functions, and the structure factor [32], but notice that the discussion assumes that the profile $h$ is translation-invariant, which may be invalidated by the presence of boundary effects.

An example thereof is the case (i) from above, which in the simplest imaginable case might be equivalent to Brownian motion. Now, $h(x)$ resembles the case of a propagating one-dimensional crack-front, but is actually different in several ways. First, the already-formed profile is frozen in time (unless one

has microscopic processes that change the free crack surfaces). Second, as in the Family-Vicsek picture of Eq. (25), one may assume that there are initial transients. Their character and the appropriate scaling picture would depend on the details. For instance, one can consider a Brownian motion confined to a maximum excursion, so that eventually the roughness would saturate. In reality, one should keep in mind that due to the presence of long range elastic fields, the dynamics of the crack tip is never a simple uncorrelated random walk in 2D. The interplay between elasticity and disorder gives in general rise to *avalanches* or stick-slip motion, as it is typical of non-linear driven systems. One may imagine that in 2D the crack is arrested at obstacles, slowing it down till a deviating path is found and the crack tip speeds up till the next obstacle. Such avalanches can be detected through acoustic emission and we will discuss this issue further in Sec. 3.

In real experiments, as in many that relate to case (iii) from above, one can also observe two complicated scenarios than Family-Vicsek scaling: *anomalous scaling* and *multiscaling*. To this end, we should consider more elaborate measures of rough surface profiles $h(\vec{x})$, measured over a window of size $l < L$ ($\vec{x}$ implies, that we will not distinguish the various crack-inspired scenarios). In full generality we can define the q-moments and assume that they scale as power-laws

$$w_q(l,t) \equiv \langle\langle \delta h(\vec{x})^q \rangle\rangle^{1/q} \sim l^{\zeta_q} \text{ for } l < \xi(t). \tag{27}$$

where $\delta h = h - \bar{h}$ is the deviation of $h$ *inside a window* of size $l$, and $\xi$ is the correlation length at which $w_q$ becomes a constant. The brackets imply again an ensemble average. The simplest case is encountered when all the $q-$order roughness exponents $\zeta_q$ are the same (i.e. $\zeta_q \equiv \zeta$ for all $q$), corresponding to self-affine scaling. The opposite possibility is referred to as *multiscaling*. In the context of kinetic interface roughening multiscaling implies that additional mechanisms create large height differences which are measured more sensitively by the higher $q$-moments (an example of this will be discussed in Sec. 5.4.4).

In terms of the local roughness, the Family-Vicsek scaling can be written as

$$w(l,t) = \alpha(t)\ \xi(t)^{\zeta}\ \mathcal{W}\left(\frac{l}{\xi(t)}\right). \tag{28}$$

with the scaling function $\mathcal{W}(x) \sim x^{\zeta}$ for $x < 1$ and a constant for $x \gg 1$. Notice that the exponent $\zeta$ can also be obtained by the structure factor, or

spatial power spectrum

$$S(\mathbf{k},t) \equiv \langle |h(\mathbf{k},t)|^2 \rangle \sim \begin{cases} k^{-(2\zeta+d)} \text{ for } k \gg 1/\xi(t) \\ \xi(t)^{2\zeta+d} \text{ for } k \leq 1/\xi(t) \end{cases} \tag{29}$$

where $h(\mathbf{k},t)$ denotes the spatial ($d$-dimensional) Fourier transform of $h(\vec{x},t)$. Alternatively, one can use the height difference correlation function

$$G_2(\vec{x},t) \equiv \langle |h(\vec{x},t) - h(0,t)|^2 \rangle^{1/2} = \int_{\mathbf{k}} S(\mathbf{k},t) \left(1 - \cos(\mathbf{k}\cdot\vec{\mathbf{x}})\right), \tag{30}$$

which for large separations scales as $|x|^{\zeta}$.

If in Eq. (28) the amplitude $\alpha(t)$ increases with time, *anomalous scaling* ensues [33], and if $\zeta > 1$ one talks about *superroughness* [33, 34]. The quenched Edwards-Wilkinson equation in $d = 1$, describing the "depinning" of a line with local elasticity is a classical example of this [35–39]. Anomalous scaling usually implies that the roughness of a self-affine object (e.g. a crack) develops a power-law dependence on the system size $L$ [33, 34]. One should thus define two different exponents $\zeta$ and $\zeta_{\rm loc}$: the first exponent describing the dependence of the global roughness on the system size, while the second encodes the scaling of the local roughness on the measuring window. In particular, the local width scales as $w(l) \sim l^{\zeta_{loc}} L^{\zeta-\zeta_{\rm loc}}$, so that the global roughness $w(L)$ scales as $L^{\zeta}$ with $\zeta > \zeta_{\rm loc}$. Consequently, the power spectrum scales as $S(k) \sim k^{-(2\zeta_{\rm loc}+d)} L^{2(\zeta-\zeta_{\rm loc})}$. Notice also that Eqs. 29 and 30 reflect only the local roughness exponent $\zeta_{\rm loc}$. This implies that for fracture surfaces with two (independent) projections, one can define no less than four independent roughness exponents, and thus there could be eight exponents describing this case.

An interesting issue here is how ordinary LEFM changes in the presence of a crack with a "rough" or self-affine geometry. The same problem can also be restated in the presence of general damage or a population of self-affine microcracks. All in all, there are at least three different possibilities. One can consider the stress-field in the proximity of a "fractal crack", but then one has to remember that Nature does not create a priori such objects - they grow because of some stable crack growth process. This takes place in the presence of elastic fields possibly modified from LEFM predictions due to the fractal geometry [40–42]. A particular version is to consider the Lamé equation, Eq. (10), in the presence of a given self-affine boundary. This can be solved in some cases to illuminate possible changes from LEFM, but is of course outside of fracture. Finally, a promising avenue is given by the work of Procaccia and collaborators [43–45], in which conformal mapping techniques developed in the context of Laplacian growth problems are combined with two-dimensional

elasticity. This allows to grow relatively large cracks iteratively, accounting for a stochastic "annealed" growth probability on the crack perimeter.

**2.6.2** ***Crack roughness and fracture energy.*** The reasons why the roughening of cracks is interesting are multiple. First of all, as discussed below, there is the usual interest in possible universality classes depending on dimension, fracture mode, and material (disorder, average response). Second, it has also an engineering implication. Consider a crack which "starts flat" and then undergoes a process which indicates a scaling behavior similar to Eq. (25). An infinitesimal crack opening will now cost *more surface energy* than in the usual case, and thus the Griffith argument (Eq. (15)) is modified in a way that accounts for the roughness exponent $\zeta$, the maximal extent of fluctuations $\xi_{max}$, and possibly also the modified elastic energy due to the rough crack. In the case of anomalous scaling (see Eq. (28) again), the extra scale also would enter the argument, further changing the amount of surface energy needed for infinitesimal crack advancement. This implies a non-trivial "R-curve", or crack resistance, since the energy consumed via forming new crack surface depends not only on the full set of exponents but again on the distance propagated [46, 47].

An expression can be written down using solely geometric arguments and the exponents as given below:

$$\Delta h(l,y) \simeq A \begin{cases} l^{\zeta_{loc}}\, \xi(y)^{\zeta-\zeta_{loc}} & \text{if} \quad l \ll \xi(y) \\ \xi(y)^{\zeta} & \text{if} \quad l \gg \xi(y) \end{cases}$$

where $\xi(y) = By^{1/z}$ is the distance to the initial notch $y$. There are two different regimes: for $l \gg \xi(y)$, $\Delta h(l,y) \sim y^{\zeta/z}$, and for $l \ll \xi(y)$, which is characterized by the exponent $(\zeta - \zeta_{loc})/z$. Important here is presence of anomalous roughening so that $\Delta h(l, y \gg y_{sat}) \simeq A\, l^{\zeta_{loc}}\, L^{\zeta-\zeta_{loc}}$.

Since the effective area from which surface energy follows is

$$G\ \delta A_p = 2\gamma\ \delta A_r \tag{31}$$

where $\delta A_r$ is the real area increment and $\delta A_p$ its projection on the fracture mean plane, the growth of roughness implies

$$G_R(\Delta a \ll \Delta a_{sat}) \simeq 2\gamma \sqrt{1 + \left(\frac{AB^{\zeta-\zeta_{loc}}}{{l_o}^{1-\zeta_{loc}}}\right)^2 \Delta a^{2(\zeta-\zeta_{loc})/z}}$$

and the resistance to fracture growth becomes

$$G_{RC}(\Delta a \gg \Delta a_{sat}) \simeq 2\gamma\sqrt{1+\left(\frac{A}{{l_o}^{1-\zeta_{loc}}}\right)^2 L^{2(\zeta-\zeta_{loc})}}.$$

For rough cracks, this is the simplest analytical attempt to consider size-effects (take $l/L$ constant) and the effect of exponents describing self-affine roughness on fracture energy.

Many authors have argued for the presence of "fractal" effects in the energy consumption (see e.g. [40]), while it seems clear that the relevant framework for calculating the true surface energy ($\gamma_s$) for the energy balance in the Griffith argument is a self-affine one [48, 49] (here we neglect the complications of multiscaling or anomalous scaling for simplicity). This can be argued for simply since the experimental situation seems clear-cut: usually cracks are self-affine (if not flat, but see also Ref. [50]). The attraction of (self-affine) fractal scaling ideas here is that they allow to understand the energy consumption mechanism(s) simply via an interpretation of the roughness exponent $\zeta$ or the fractal dimension $D_f$. The models to be discussed in later sections are a toolbox for testing the influence of disorder on strength, since these models lead to rough, self-affine cracks. If one allows for mesoscopic plasticity, one would still expect the same kind of problems, but further theoretical questions are expected.

## 3 Experimental background

To give a reference point for the theoretical and numerical ideas discussed later, we next overview shortly some relevant experimental quantities, focusing on fracture properties for which disorder and stochasticity are crucial. When necessary we refer to the concepts presented in the Introduction, or point forward to the theoretical state-of-the-art presented in later sections. We would like to emphasize rather generally that the statistical aspects of fracture processes - scaling, exponents, distributions - are not understood even in the sense of a synthesis of experiments, with the main exception of the roughness behavior. This is by force reflected in the discussion that follows.

The first of the issues is strength, both in terms of its probability distributions and the scaling with sample size. As noted in the previous section, from the theory viewpoint, the statistics of strength depend crucially on the presence of disorder. Next, we consider crack roughness, which has an application to the question of the origins of the fracture toughness. As pointed out already in Sec. 2.6.2, this is due to at least two reasons. The energy consumption that takes place when a crack increases in size is due to the product of surface

energy and the new area. Both can be affected by disorder, as in the case of Griffith-like energy arguments and in the idea of crack surface area increasing with scale for self-affine cracks. In the case of fracture strength, disorder can be easily reinterpreted as a "flaw population", whereas for cracks that roughen, disorder plays the role of "noise" during crack dynamics. This noise can either be "quenched", i.e., exists in the sample from the beginning in many disguises, or be created dynamically via for instance void-formation.

A very important topic from our point of view is represented by acoustic emission (AE) in fracture experiments, a nice example of *crackling noise*. The released elastic energy in fracture is a revealing diagnostic for the temporal aspects of fracture processes, and is used in applications as a monitoring tool for damage assessment. In addition, it has been long since realized that the AE signal appears to be *critical*: the energy of AE events often exhibits a power-law -like probability distribution. In contrast to thermal imaging or displacement field analysis, AE is not limited to sample surfaces and is sensitive to even very minute events. The two fundamental questions that concern us are: i) how to connect the AE behavior to the other fracture properties, and ii) how to understand theoretically the AE statistics.

In the last part of this section, we briefly outline phenomena that exhibit time-dependent response, and often go beyond the scope of brittle fracture. This concerns the role of microscopic but collective effects on crack growth resistance ("R-curve") due to plasticity, and slow fracture processes with history effects such as creep and fatigue failure. We mostly omit discussing the spatial aspects of plastic deformation such as shear bands that bear some similarity to damage localization and fracture development in brittle and quasi-brittle fracture.

### 3.1 *Strength distributions and size effects*

Measuring the scale-dependent properties of strength is difficult mainly because of sample-to-sample fluctuations. In addition, samples have free surfaces, and though one often compensates by adjusting the test geometry for the resulting free boundary effects (Poisson contraction), materials often display surface defects, giving rise to additional disorder. We can thus expect that the strength distribution will be a superposition of cases where surface-induced defects lead to failure and cases where bulk defects rule the process. Obviously, separating the two mechanisms can be difficult. In the classical approach, the sample strength and the size effect is measured with a prepared notch. To obtain reliable results, one should have access to a large enough range of sample sizes.

Fig. 7 presents experimental data from brittle ceramics, wherein the data are plotted according to different extremal statistics distributions [51]. In this

particular case, the Gumbel form fits the data better than the Weibull distribution [51]. The latter is traditionally used in the engineering literature in the analysis of fracture statistics and size effects in strength [52, 53]. One should pay attention to the fact that a Weibull scaling can be ascertained more reliably by tests with varying sample sizes. One should note (see also Sec. 2.4) that there is a priori no reason why a material should fulfill the prerequisites of belonging to any of the classes following from extremal statistics, be it Weibull or Gumbel.

Various recent attempts to characterize the strength distribution in materials with intrinsic disorder such as paper [54,55], concrete [56] and others [57,58] illustrate clearly the inherent difficulties in interpreting the data. Fig. 8 demonstrates this for concrete samples with a 1:32 size range. In this particular case, in addition to the inherent disorder and randomness, one has to deal with systematic stress gradients present in these samples. This appears to be a generic problem that persists among various experimental studies (see e.g. [59]).

In the engineering mechanics literature, the scaling of strength with sample size is usually discussed with the aid of three-point bending or tensile tests, done on samples in which the ratio $a_0/L$ of notch size to sample size is constant. Clearly, in the absence of any other effects, the square-root -like enhancement $K \sim \sqrt{a_0}$ for the stress intensity factor will eventually win the competition over the disorder, so that the strength will decay as expected by an inverse square-root law: $\sigma_c \sim 1/\sqrt{a_0}$. For small enough $a_0$ the situation is, however, not so simple since the stress enhancement due to the notch competes with the disorder. In this respect, Fig. 9 demonstrates an example of data from concrete, where one can observe clear deviation from the ideal behavior.

In the presence of disorder and/or plasticity the scaling with a constant aspect ratio may be complicated by one issue. Using engineering mechanics language, the fracture process zone (FPZ) size $\xi_{FPZ}$ may not be constant as a function of $a_0$ and $L$. Thus the energy balance (Griffith's) argument develops a size-dependence, which can be understood considering that the energy needed for crack growth changes with the volume of the FPZ. Such complications should depend on the details of the processes that make the FPZ change size. There is an extensive literature on the connection of microscopic and mesoscopic mechanisms to the size-effect, analyzing the possible behaviors of $\xi_{FPZ}$ for various materials. Many of these exhibit "strain-softening", but other processes as crack bridging by fibers or precipitates etc. are surprisingly general as well from composites to concrete [60–75]. This kind of analysis often also takes into account the role of free surfaces, which modify the FPZ geometry if the crack is close to a free surface. From our viewpoint, one should note that the presence of disorder can simply make small enough cracks irrelevant [76], masking the presence of such defects. Simply put, the randomness can correspond to an effective flaw size $a_r$, so that for $a_0 < a_r$ a flaw is so small

as to not change the general behavior.

In conclusion, the issue of fracture strength from the statistical physics viewpoint appears to still lack, to a large degree, physics-oriented experiments, which would help to connect scaling theories to reality. It would for instance be of immense interest to have empirical characterizations of the "disorder" (as a microcrack population) from sample to sample, and a concomitant measurement of the sample strengths.

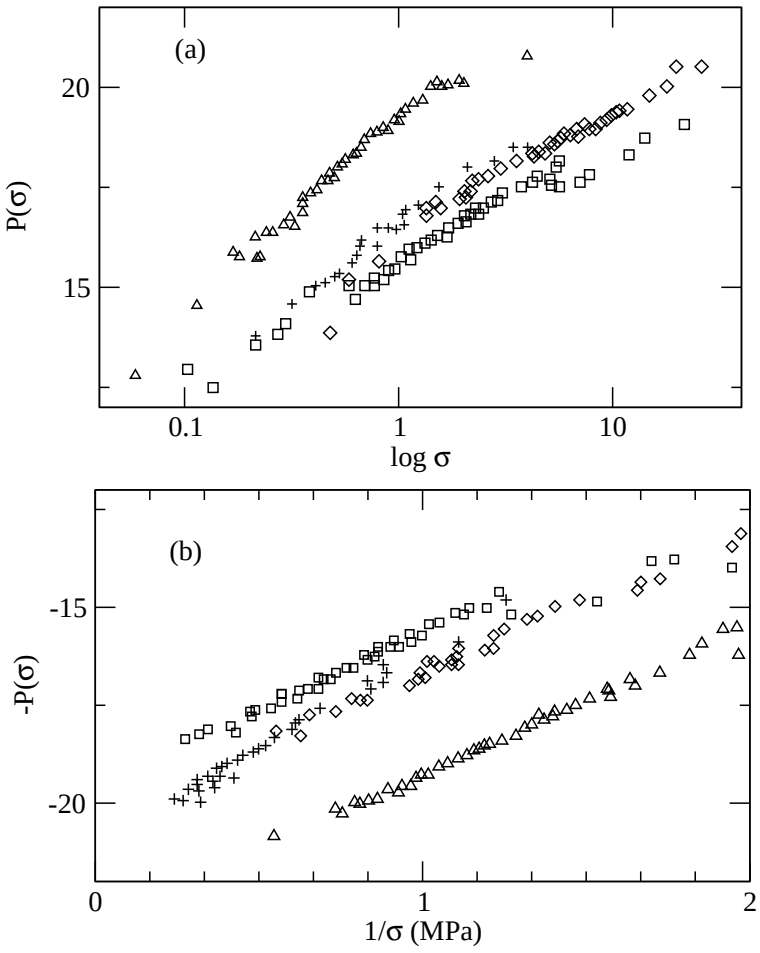


Figure 7. Examples of trial scaling plots for strength distributions of porous, brittle ceramics (from Ref. [51]). By plotting the distributions in various scales one can try to establish whether the shape resembles the Gumbel or Weibull form the best.

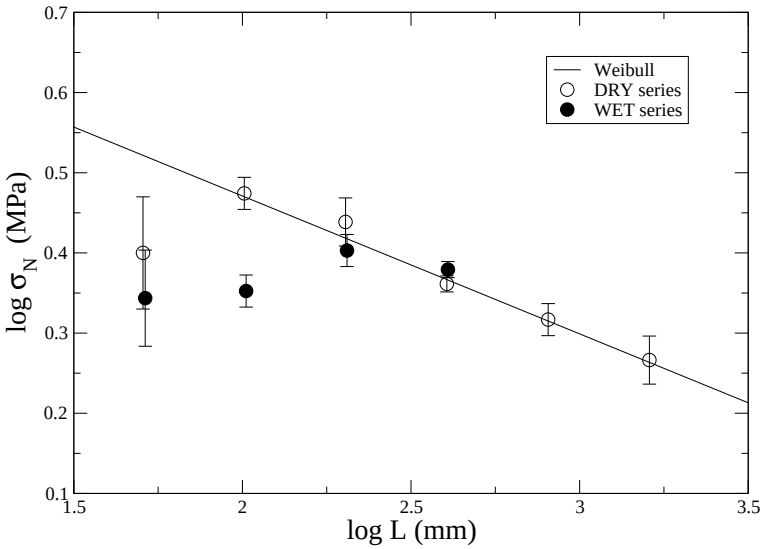


Figure 8. The size-dependence of concrete for two different ambient conditions (adapted from [56]` size $D$ (for $D$ cture.

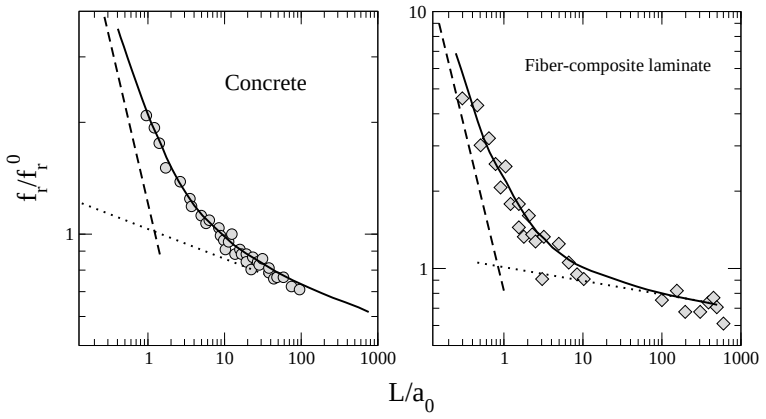


Figure 9. The typical size-effect from various experiments on concrete. It is clear that the data for flexural strength, $f_r$, exhibits a cross-over to a scaling as a function of $D$, that may (perhaps) follow the Weibull size effect for large $D$ values [74].

### 3.2 *Rough cracks*

There are many different experimental signs of self-affine scaling for crack surfaces in various scenarios reminiscent of those overviewed in Sec. 2.6.1. An excellent review by Elisabeth Bouchaud summarizes the major results up to 1998 [77]. In general, one has two main issues: first, understanding the scal-

ing, depending on the details such as spatial dimension, material characteristics and loading state. In the language of self-affine geometry, this implies determining experimentally the scaling exponents, such as the $\beta$, $z$, and $\zeta$ of the simplest Family-Vicsek scaling. Ultimately, a determination of the behavior in terms of the exponents and scaling functions would point out the right stochastic equation that governs the process, including the noise that is present. Second, whatever the truth be about universality, one can search for the mechanisms that lead to the formation of rough interfaces, and try to understand the consequences of self-affine crack surfaces. In other words, regardless of whether one can write down an equation describing the dynamics of a crack front, the process is intimately coupled to other physical characteristics as acoustic emission, and damage mechanics. We classify various experimental results according to the dimensionality of the scenario described in Sec. 2.6.1.

The conceptually simpler case of crack roughening is in general provided by case (i), where a the final crack path is given by a one-dimensional curve $h(x)$ in two dimensions. Two typical examples are shown in Figures 10 and 11 from paper fracture. These illustrate the diffusive nature of fracture, such that it is clear that the asymptotic *scaling* of $h(x)$ can only be attained beyond some microscopic lengthscale $\xi_m$ in $x$ and $h$. That is, this might imply that $h(x)$ exhibits rms fluctuations (local width) with $w(l) \sim l^{\zeta}$ only for $l \gg \xi_m$. An example is provided of such behavior in Fig. 11.

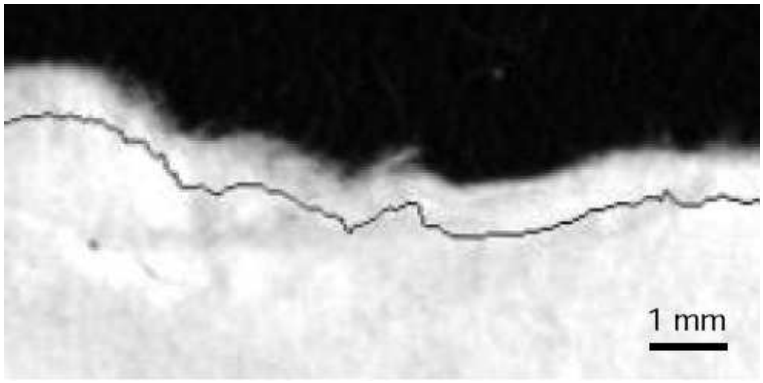


Figure 10. The diffuse crack surface in paper (a two-dimensional material) and the thresholded "interface", shifted down for clarity (courtesy of L. Salminen, HUT). Here, the issue concerns how to define an unique $h(x)$ in the case the damage field is continuous (one can see individual fibers in the image on the other hand).

More quantitatively, the existing results point out towards a 2D (local) roughness exponent in the range $\zeta \simeq 0.6 - 0.7$ [78–80]. A number of observations can be made: the measured value is higher than a random walk or a Brownian motion value $\zeta_{RW} = 1/2$, and $\zeta > 1/2$ implies interesting posi-

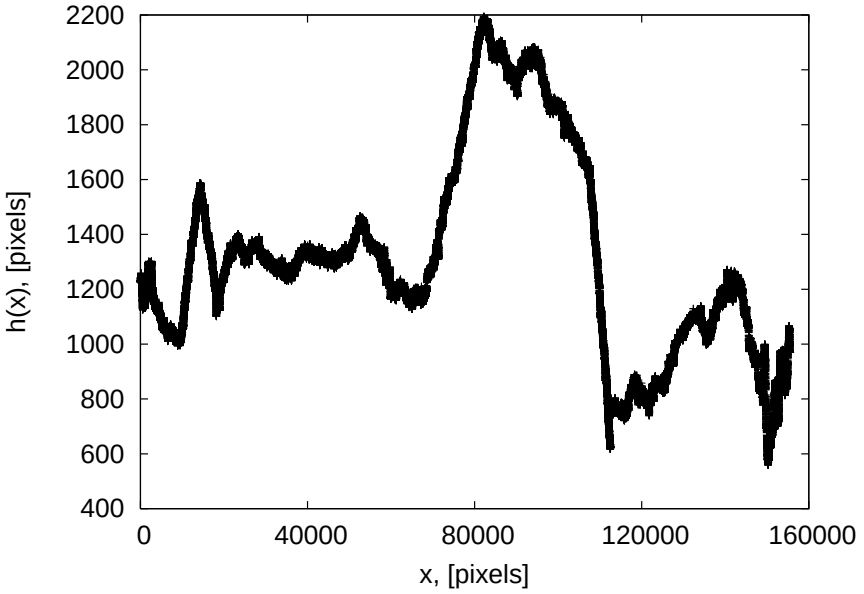


Figure 11. An example of a 2D crack-line from a paper web, of width 6500 $mm$ [78]. The sample has an *effective* exponent of about 0.6 as shown by various measures, but only above a scale of about 2-3 $mm$ ($\propto$ 30 pixels in the lateral direction).

tive correlations for the motion of the crack tip. The value is also close to the numerical predictions of various models, both theoretical ones and the RFM as discussed in Sec. 6.4. However, even for ordinary, industrial paper itself there are numerous values available that are significantly higher than say 0.7 (examples are found in Ref. [81]). It is not known at this time whether this reflects the difficulty of experimentally measuring $\zeta$, or the fact that the result is not "universal" but depends on material parameters as for instance ductility and anisotropy. In addition Bouchbinder et al. have indicated a scenario in which the $h(x)$ has more complicated structure, exhibiting *multifractal* behavior (implying a $q$th-order dependent $\zeta_q$ for the various $q$-momenta of roughness measures, see Sec. 2.6.1) [82]. An alternative explanation is simply a crossover below $\xi_m$ as suggested above [78]. Note that the values of $\zeta$ can not simply be interpreted as fractional Brownian motion, since history effects in $h(x)$ are more complicated.

Complicating our understanding of the problem is the fact that the role of kinetics (velocity, dependence on the loading scenario) has not been studied systematically. When experiments are started from a notch, the useful conceptualization is to consider the $h(x)$ to be a trail of a particle, the crack tip. Then, there are two issues of immediate relevance: the role of the average crack tip velocity, and the translational invariance of the profile. The former

is important since various kinetic effects might be crucial, even for slow failure as in, for example, creep or fatigue fracture. The crack tip velocity is even more relevant for fast fracture where the timescales of sound waves are not well separated from the velocity. In analogy to the discussion in Sec. 2.6.1 the crack dynamics is expected to follow a scaling that depends on the distance to the crack tip, so that translational invariance is broken for $x < \xi$, before eventual saturation. This caveat is in particular relevant if one considers a case where there is a FPZ whose size, and thus $\xi_m$ changes with crack length $l$.

When a crack front propagates between two elastic blocks, the dynamics is enforced to be quasi-two-dimensional and one can again define an interface $h(x)$ separating the intact from the failed region. The theoretical models for this experimental setup, referred as case (ii) in Sec. 2.6.1, are dealt with separately in Sec. 5.3. The interest here lies with the roughness exhibited by $h$ and the associated dynamics as $\bar{h}$ changes slowly with some average velocity. Knut Måloy and collaborators have performed experiments on a couple of joined Plexiglas plates, previously sandblasted to induce a randomness. The dynamics of the crack is followed using a camera. As demonstrated in Fig. 12, the crack front moves by avalanches, whose areas are distributed according to a power law distribution $P(A) \sim A^{-1.8}$ (Fig. 13). The authors have also estimated the roughness exponent using different methods and the result is $\zeta \simeq 0.6$ [83–87]. Notice that this value is similar to the one measured in case (i) but the geometry and the elastic interactions are completely different. Thus there is no apparent reason to identify the two values.

Most studies performed in the past, starting from the first pioneering work of Mandelbrot et al. [88], refer to three dimensional fracture, case (iii) according to Sec. 2.6.1. The evidence collected during the first decade of experiments on several materials suggested the presence of a universal roughness exponent in the range $\zeta \simeq 0.75 - 0.85$ [77]. The scaling regime over which this result is obtained is quite impressive, spanning five decades as it is shown in Fig. 14. In some cases, namely metals, it has been shown that a different exponent (i.e. $\zeta \simeq 0.4 - 0.5$) describes the roughness at small scales, with a crossover to the large-scale value. Fig. 15 displays an example of both the short-scale and large-scale regimes in a typical (fatigue) experiment. This crossover has been initially explained as a dynamic effect: the small scale exponent would reflect the quasistatic limit and the large scale exponent the effect of finite velocities [77]. Notice, however, that the short-scale value is sometimes not observed, even at very low velocities as for silica glass [89], while in other cases, namely in granite and sandstones, the large-scale exponent is not seen even at high velocities [90].

Since the crack surface is separated from the intact part of a sample by a line that can fluctuate both in the out-of-plane and in-plane directions, one can in principle measure two exponents $\zeta_\parallel$ and $\zeta_\perp$ (see Sec. 2.6.1). This was first

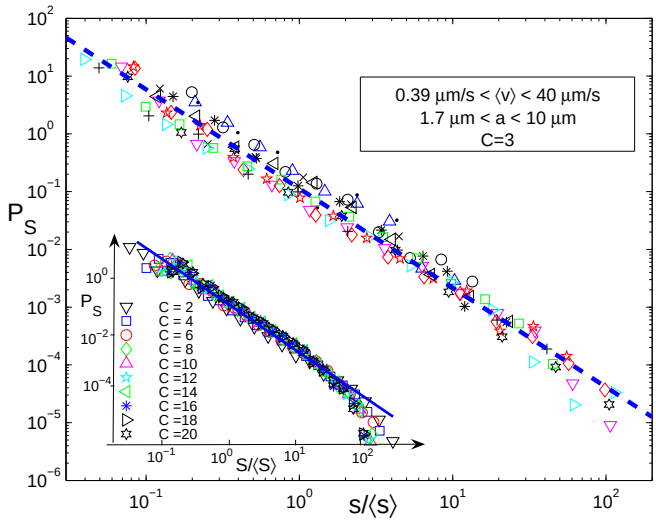


Figure 12. Examples of crack fronts in a quasi-two-dimensional setup where a rough interface between two elastic plates is used as the substrate for the crack line. Notice the avalanche-like localized advancement of the line between subsequent frames. These can be used to measure locally the roughness exponent $\zeta$ via the relation $\Delta h \sim l^{\zeta}$ where $\Delta h$ is the average displacement, and $l$ is the lateral extent of the region which moved [87].

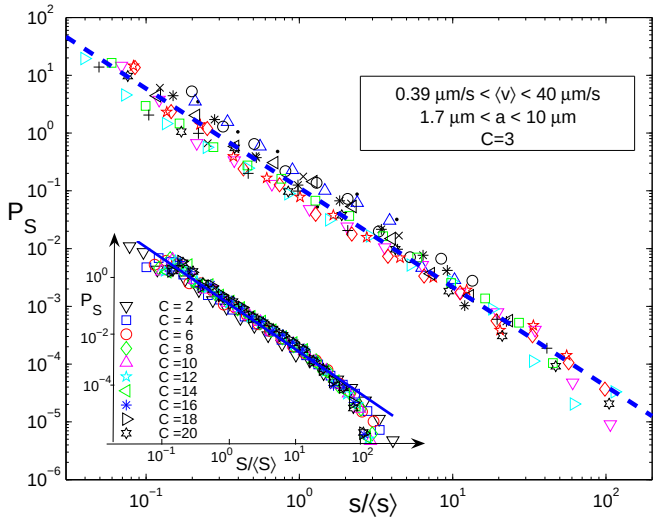


Figure 13. The avalanche size distribution $P(A)$ in the Plexiglas experiment of Ref. [87]. Notice the independence of the scaling exponent of the actual average crack velocity.

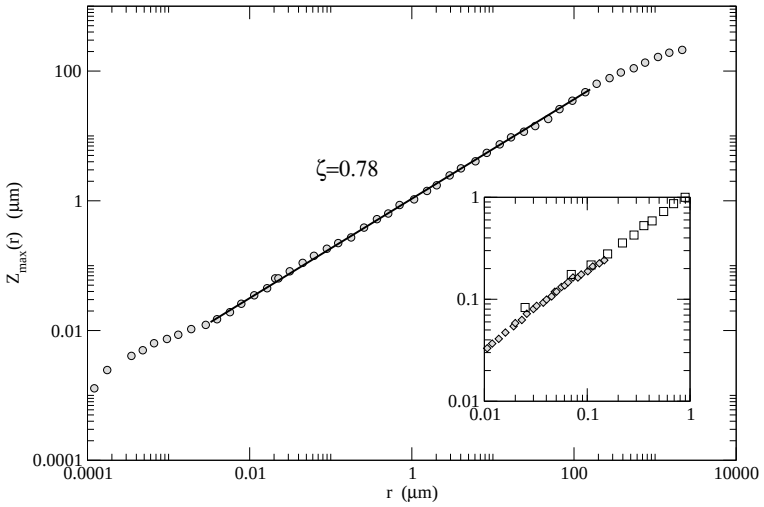


Figure 14. Roughness scaling measured in a metallic alloy broken in tension. $Z_{max}(r)$, the maximum $h$-value difference inside a window of size $r$ shows scaling over five decades with an exponent of $\zeta \simeq 0.78$. The inset shows the overall between two different measuring techniques (from Ref. [77]).

attempted via elaborate experiments by stopping the experiment and cleaving the sample ( [77]). Very recent research has brought new light into these issues. Ponson, Bouchaud, and co-workers have tested the line propagation scenario on four materials with very different microstructural and brittleness/ductility properties [89, 92]: silica glass, an aluminum alloy, mortar, and wood. Fig. 16 shows an example of the correlation functions and the appropriate exponents, that seem to be valid for all these cases, and independent of the detailed mode of fracture (tensile, two-point bending, fatigue etc.). The parallel scaling is in agreement with earlier $\zeta$-results. It is noteworthy that in both cases one has the same dynamical exponent $z$, so that the two-dimensional correlation functions (to use the notation of Ponson et al., where $x$ is the direction of propagation) would follow the scaling Ansatz. Ponson et al. find that $z \sim 1.25$ which together with the Family-Vicsek relation then sets the three exponents (see Fig. 17)

$$\begin{aligned} &\Delta h(\Delta z, \Delta x) = \Delta x^{\beta} f(\Delta z / \Delta x^{1/z}) \\ &\text{where} \quad f(u) \sim \begin{cases} 1 & \text{if u}\ll 1 \\ u^{\zeta} & \text{if u}\gg 1 \end{cases} \end{aligned} \tag{32}$$

Thus, in this framework, the direction of crack propagation has the role of the time axis and is thus described by a growth exponent $\beta \equiv \zeta_{\perp}$. This is because

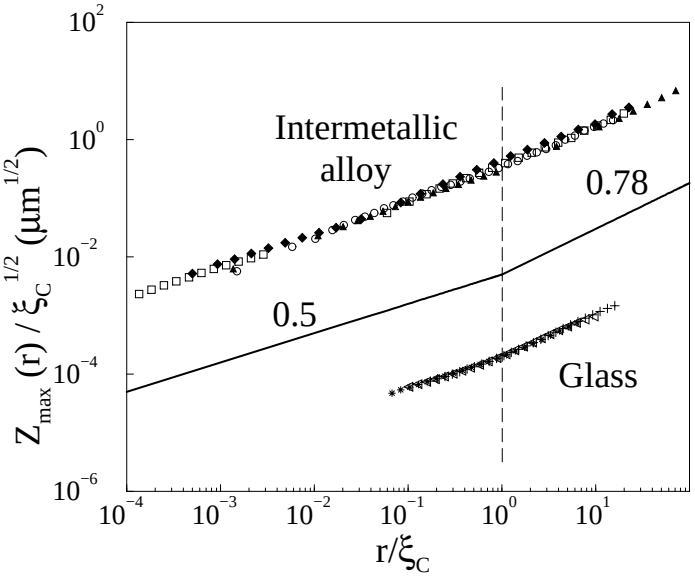


Figure 15. $Z_{max}(r)/\sqrt{\xi_c}$, the maximum $h$-value difference inside a window of size $r/\xi_c$ for two materials. Here $\xi_c$ is a cross-over scale that can be determined separately and may be thought of as the FPZ scale. As can be seen for both cases and for various velocities of crack growth, there seems to be two different regimes of roughness with $\zeta \simeq 0.5$ at small scales and $\zeta \simeq 0.8$ at larger scales ( [91]).

the fracture surface results indeed from the trail left by the crack front and the dynamic scaling properties of the roughness are encoded in the perpendicular component.

The role of microstructural disorder for fracture roughness is still debated. Recent experiments point out the difference of intergranular-transgranular fracture [93], and in many materials crack bridging should play a role in roughening. Some steps towards a more complete understanding come from the seemingly irrelevant role of crack growth velocity [94], and the fact that the same values for the roughness exponent can be measured from a very brittle material such as amorphous glass [95, 96] where the role of plasticity is negligible, and $\xi_{FPZ}$ being of the order of a hundred nanometers. Thus the roughness may originate from void formation, a process that has not been studied much from the viewpoint of statistical fracture. Bouchaud et al. [97] noted that in intergranular fracture, one sees similar geometric phenomena as in tree-like directed percolation clusters of statistical physics. The ideas of branching critical cracks have not been studied systematically since then. One should bear in mind that it is only the 2d projection of the 3d crack structure that is directly analogous to such a "percolation cluster".

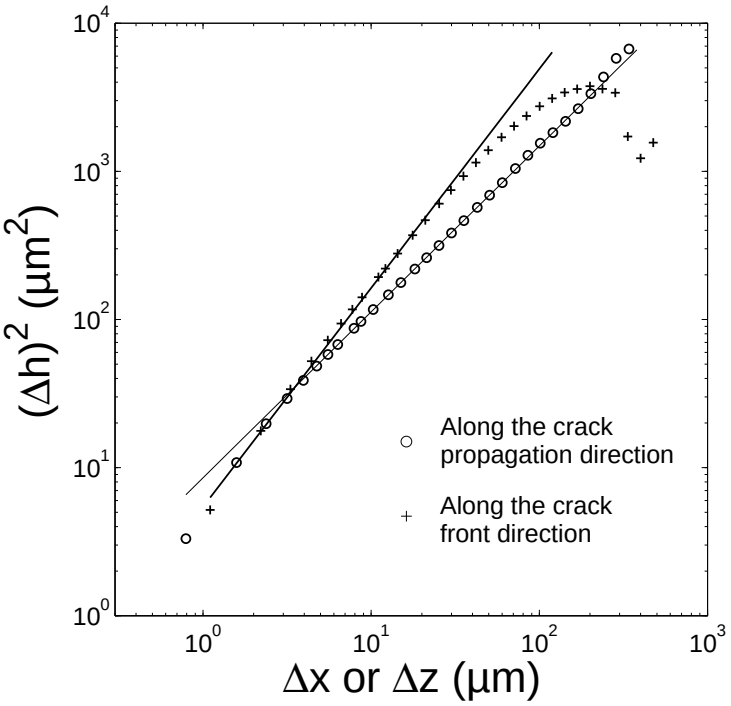


Figure 16. 1D height-height correlation functions for $h_{\|}$ and $h_{\perp}$, in the notation of Sec. 2.6.1 for an aluminum alloy fracture surface [89]. The apparent scaling exponents are $\zeta \equiv \zeta_{\|} \simeq 0.75$ and $\beta \equiv \zeta_{\perp} \simeq 0.58$.

We should also mention that there are signs of anomalous scaling from crack propagation experiments in three dimensions [33,98–100]. Thus the commonly measured local roughness at a distance $l$ does not obey Family-Vicsek scaling, but we would need an additional independent exponent to describe the coupling to sample size, $L$, as discussed in Sec. 2.6.1. The origin of these scaling laws still remain to be understood, possibly in the framework of line depinning -models. Note that Bouchbinder et al. have recently suggested that the actual scaling picture is not simply self-affine, but one would need to resort to structure functions as in turbulence [101].

Finally, Fig. 18 demonstrates how the crack growth resistance (as measured by the energy release rate $G_{RC}$) depends on sample size $L$ in 3D experiments on two kinds of wood [46,47]. This can be compared to the theoretical scaling given in Sec. 2.6.1. This implies, that the self-affine picture of crack surface geometry would be directly useful in engineering applications if a mathematical relationship can be established between $G_{RC}$ (or $K$) and $\zeta$ and the material in question. One should keep in mind two issues: the complete absence of a

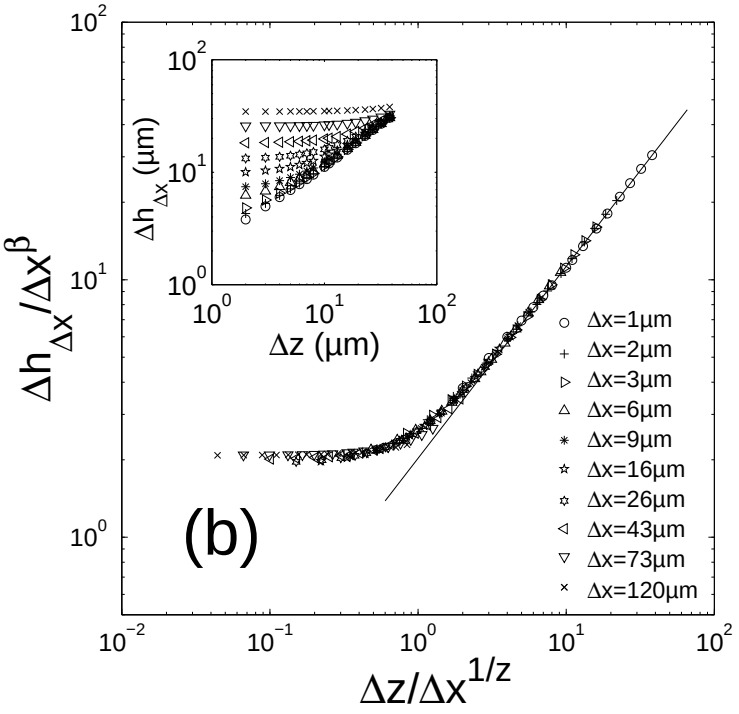


Figure 17. 2D height-height correlation functions $\Delta h_{\Delta z}(\Delta x)$ for various $\Delta x$, $\Delta z$ for a fracture surface of an aluminum alloy ( [89]). The collapse uses the form suggested by Ponson et al., Eq. (32)

.

theory to explain the value of $\zeta$ and the anomalous scaling picture, and the fact that quite possibly the microscopic mechanism that makes $G_{RC}$ increase with $L$ also has a role to play in setting the actual value of $\zeta$. An engineer's way to explain this is that it is simply the prefactor that matters to first order, in $K$, not $\zeta$, in particular if $\zeta$ would prove to be universal.

To conclude, we note that fractography is becoming a mature sub-branch of fracture mechanics, trying to establish links between the qualitative processes and the phenomenology of surface geometry on one hand, and on the other hand between crack topography and materials parameters such as fracture toughness and orientational effects (a good reference is the book by Hull [102]). There has been little effort to couple the statistical signatures of other quantities to those of crack surface roughening, however, regardless of whether one starts from the statistical physics or materials science viewpoints.

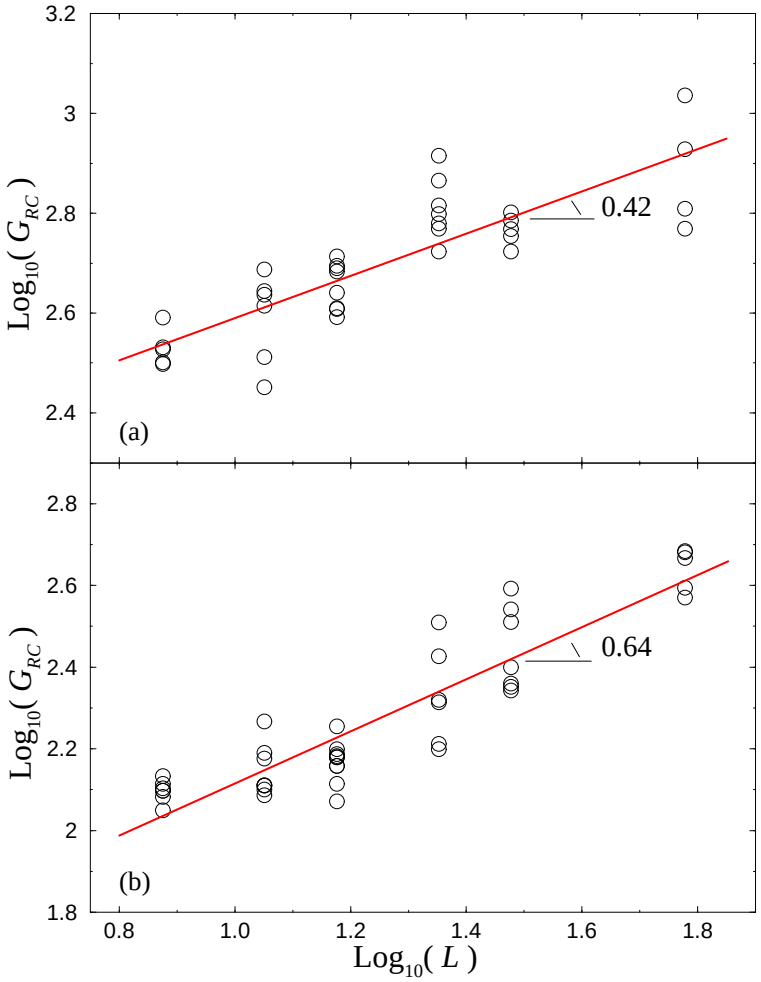


Figure 18. Size effect on critical energy release rate $G_{RC}$ for two kinds of samples: pine (a), and spruce (b). The expected slopes are using the associated roughness exponents $\zeta - \zeta_{loc} = 0.47 \pm 0.17$ for pine (a), and $0.73 \pm 0.17$ for spruce (b) (from [47]).

### 3.3 *Acoustic emission and avalanches*

The microscopic processes that take place in a fracturing system with one or with many cracks are difficult to follow experimentally. Some of the possibilities available are thermal imaging, electromagnetic diagnostics, surface strain measurements including digital interferometry, elastic modulus diagnostics [103], and three-dimensional tomography [104]. All of these have their disadvantages including lacking spatial and temporal resolution, inability to access bulk dynamics, and the presence of several noise sources that make

interpreting data difficult.

Here we concentrate on perhaps the best way to characterize microfracturing dynamics, acoustic emission (AE). This is an example of "crackling noise" which has gained considerable attention in other contexts, from the viewpoint of statistical physics. Acoustic emission arises in brittle fracture due to the release of elastic energy, but can also originate from internal friction or dislocation motion, to name a few possible other causes. In the geophysics literature [105] in particular it has been discussed in the context of scaling and patterning of fault systems and fracture networks [106–108], and the growth laws of the same [109,110]. In analogy to the simple statistical models discussed in this review the simplest theoretical interpretations concern the relation of released elastic energy to the detected AE. However, in most cases the models at hand do not take into account the discrete statistical and noisy nature of the AE data which is, here as well as in the context of earthquakes, really important.

A typical AE experiment is based on detecting acoustic activity via piezoelectric sensors that convert the sound into an electrical signal. Various levels of sophistication exist, that allow to distinguish between exact waveforms and to triangulate the wavesource(s). After noise thresholding, the essential point is the existence of well-separated "events" such as depicted in Fig. 19. It shows two subsequent events from a tensile test on a paper sample, and demonstrates the most important quantities that relate to such a signal: quiet times, event durations and event energies. In a slow fracture experiment one has a separation of timescales, except perhaps close to the final catastrophic breakdown. The events as detected by an experimental system are difficult to interpret because of attenuation [111, 112], measurement system response, and dispersion including reflections from (internal) surfaces. Hence, only the simplest quantities such as energy, amplitude, and silent intervals are relatively easy to analyze. Nevertheless there is a considerable body of work on the relation of AE to microscopic fracture mechanisms and damage accumulation versus material composition, including for instance concrete and metal-matrix and fiber composites where the contrast between the fibers and the matrix, allow such a distinction [113–119].

Figure 20 depicts two tensile tests for paper samples, illustrating the typical dynamics of AE in a test. The interesting questions are, quite similar to crack roughness, how does the statistics depend on rate of loading, dimensionality, material, and fracture mode? At the simplest level the integrated acoustic energy should tell about the loss of elastic energy content, and thus be proportional to $(1 - D)$ (in terms of a scalar damage variable) if one assumes that attenuation and acoustic coupling do not change as failure is approached. From a variety of experiments that include a variety of loading conditions including tension, compression, and shear, and in addition under creep loading

conditions, and different materials it has been found that the silent times $\tau$ and the acoustic event energies $E$ follow analogies of earthquake statistical laws. For the energy, one has

$$P(E) \sim E^{-\beta}, \tag{33}$$

and for the intervals

$$P(\tau) \sim \tau^{-\alpha}, \tag{34}$$

where the exponents $\alpha$ and $\beta$ are akin to those of the Gutenberg-Richter and Omori laws of earthquakes. Typical values for $\alpha \sim 1 - 1.5$ and $\beta \sim 1 - 1.3$ are then a target for theoretical models [120–125]. An example of the energy statistics is given in Fig. 21, for paper as an example of a two-dimensional test material. In an in-plane experiment, $\beta \sim 1.8$ has been found [126] which is intriguingly close enough to the avalanche exponent of crack lines in Plexiglas (see Fig. 13 [87]).

The example of Fig. 20 hinted already about one particular aspect of typical fracture AE: the lack of time-translational invariance since e.g. the activity gets stronger as the $\sigma_c$ is approached (though in special cases, as in "peeling" [126] this can be circumvented). This presents both a challenge in order to understand the statistics - recall that often one does not have access to large quantities of data - and implies that the AE timeseries contains clues about the microscopic dynamics.

Fig. 22 (ref. [127]) demonstrates how the *amplitude* statistics changes as one follows a fracture experiment along the stress-strain curve. Here, the "b-value" or the analogous $\beta$-exponent becomes smaller signaling that there are larger and larger energy releases as $\sigma_c$ is approached. The b-value is one of the targets of theoretical analysis based on averaged damage and crack-growth laws, and is based on a "$K_{eff}$", which would predict energy release rates as the catastrophic fracture gets closer. These models can of course be tuned so as to match with the general trends of detecting larger amplitudes as the final fracture is approached. Still, the agreement is qualitative and the possible "universality" of the signatures remains unclear [128–134]. Similar b-value studies have outlined e.g. the role of pre-existing cracks in statistics [135], followed damage [136] and discussed the crack velocity's role [137].

The changes in behavior as sample failure is approached and the concomitant changes in data can be discussed in a variety of ways. One way to consider the matter is to try to do actual localization experiments. These often suffer from the fact that dead-times of the apparatus and uncertainties in localization make it difficult to follow all the developments (in contrast to plastic deformation [138], or steady-state fracture where the possibility of a quasi-steady

state exists [126]). Nevertheless, it can be convincingly be demonstrated how damage localizes to the final process zone, or to the proximity of an advancing crack in the final stages of stable crack growth.

One can also check when or up to which point the assumption of slow failure is valid, in that the events remain uncorrelated on the fast timescale of inverse sound velocity [139]. The spatial clustering of events has been extensively discussed in rock mechanics [140–143] and correlation analysis is often performed on the AE timeseries [144, 145]. The latter presents a technical problem due to the non-stationarity of the time-series, as the AE event density often most varies during the experiment, and thus one should apply caution. In the spatial case, one can also do entropy analysis to distinguish between random, Poissonian statistics and real clustering [122]. This is demonstrated in Fig. 24 where one can see the development of correlations in the locations of AE events "in the plane", when a planar sample is subjected to an effective tensile load. The final failure surface is circular, as can be seen in Fig. 24a. The same samples (of wood) also allow to look at the clustering of the event locations via "entropy analysis" (Fig. 24b) in analogy to what we discuss about damage development in the numerical models below. An open question is, whether one can by spatial analysis say something about the dynamics inside and formation of the FPZ [146] and determine the "Representative Volume Element" size (see e.g. [147]).

Another consideration is to link the AE activity to final crack formation and properties, but unfortunately so far this has not been attempted (in paper, one can relate the jerky advancement of a crack tip - which is easy to demonstrate, see Ref. [148] - to AE activity, though). Instead, several authors have considered the AE energy release rate, or the integrated energy as a simplest way to see the approach to final failure. This naturally tells about the correlations in the damage development, and the nature of the final crack growth. Conflicting evidence exists, and Figure 23 shows that in some cases experimental data can be used to justify the possibility of a "critical divergence", in that the data seems to fit a scenario where $\partial E/\partial t \sim (t_c - t)^{-a}$, where $t_c$ is a failure mode -dependent critical time (e.g. equivalent to a critical strain). In some cases, this seems not to work so well (an exponential increase is rather indicated) [149], moreover such data has also been used to justify the presence of collective dynamics in the process via "log-periodic oscillations", [150, 151]. Such collective phenomena, of unknown exact origin, would be of importance since they would allow to consider AE as a diagnostic for sample life-time or failure predictability.

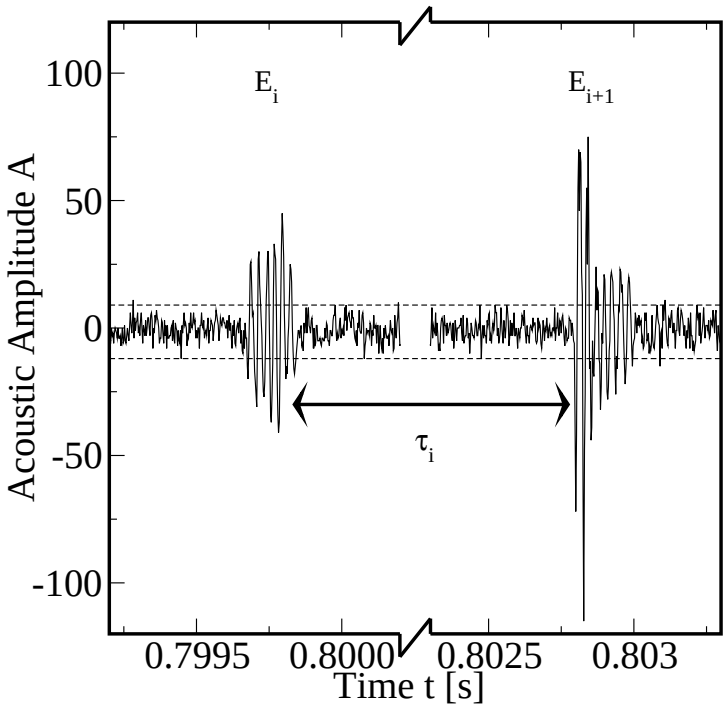


Figure 19. A typical example of the crackling noise of acoustic emission (courtesy of L. Salminen, HUT). The two events that are detected are often well-separated in time and are characterized by duration intervals $\tau_i$ and energy $E_i$. Note the presence of noise in the setup, which means one has to threshold the data to define events.

### 3.4 *Time-dependent fracture and plasticity*

Creep, fatigue and ductile failure extend the theoretical questions one meets within brittle or quasi-brittle fracture. Dislocations, activated dynamics, and frictional response (fiber pull-out in fiber composites, crack surface interactions) can be combined with the presence of "disorder" (the emphasis of this article) to repeat many of the relevant questions: how to describe the statistics of strength, how to understand the properties of crack surfaces, and how to interpret damage mechanics via acoustic emission. In fact in many of the experimental references cited above one can not so easily label the material or test at hand as purely brittle or "ductile". In some cases the physics is changed "relatively little": the existence of ductility and plastic deformation is interpretable in terms of a FPZ size $\xi_{FPZ}$ inside of which the divergence of the stress-field of LEFM is cut off.

The two classical problems of fatigue and creep should also be affected by disorder. Indeed, the "Paris' law" which states that the lifetime $t_f$ of a sample

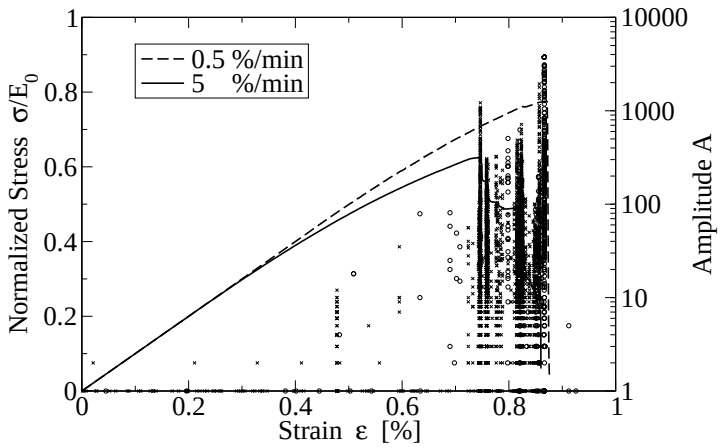


Figure 20. Two examples of acoustic data series (crosses and circles) for two strain rates of paper samples in tensile testing. The stress-strain curves change with the strain rate (from Ref. [125]).

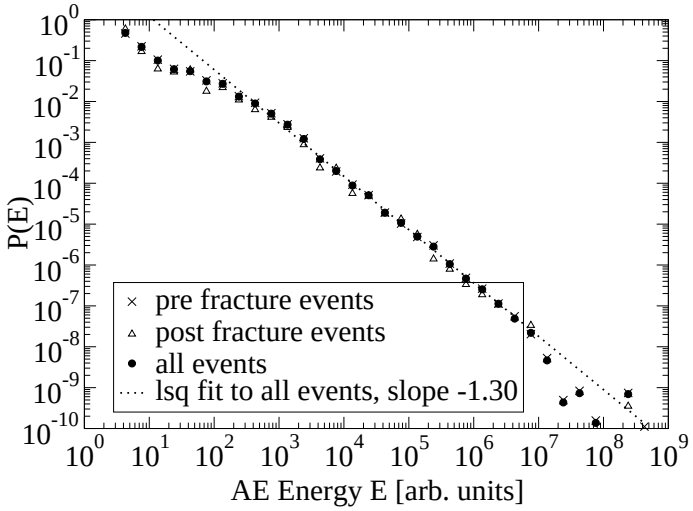


Figure 21. Three different energy distributions from a tensile AE test for paper ($\dot{\epsilon} = 1.0$ [%/min]). The data is separated in addition to the total distribution for the post- and pre-maximum stress parts (from Ref. [125]).

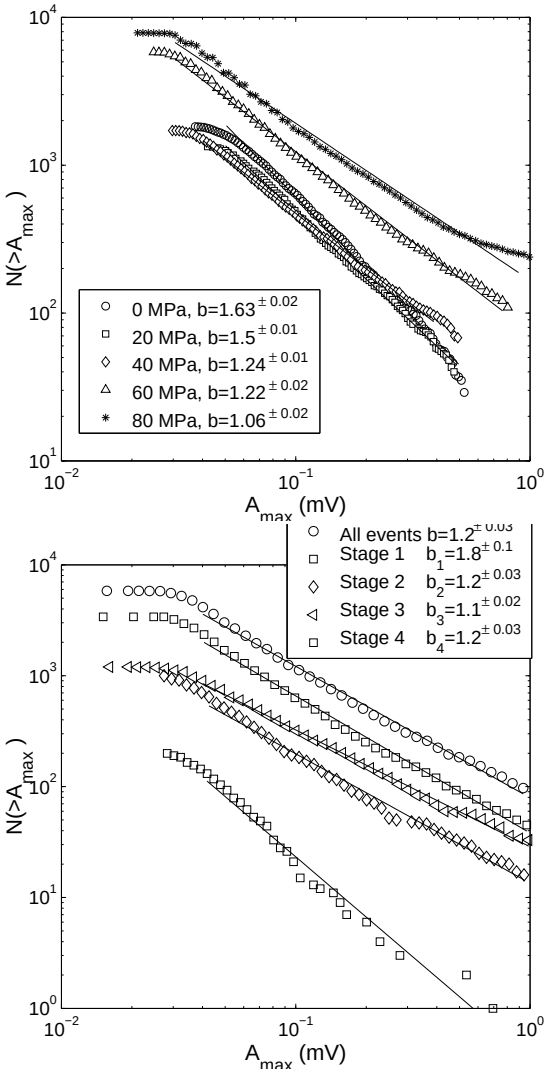


Figure 22. "b-values" or the corresponding amplitude distributions for acoustic emission from rock samples. It is noteworthy how the exponent of the cumulative distribution becomes smaller (from "stage 1") as the maximum point along the stress-strain curve is approached [127].

in stress-cycled experiment, with a variation $\Delta K$ for the stress intensity factor scales as $t_f \sim (\Delta K)^n$ where $n$ is the Paris' law exponent, can be measured in various non-crystalline materials which are certainly inhomogeneous [152]. Likewise, the physics of creep in disordered materials as paper or composites is affected in some yet to be understood way by the randomness. This can be seen in the stick-slip -like advancement of cracks in creep [153] and in

the statistics of creep times and the related acoustic emission [154]. In these directions, much more careful experimental work is called for.

In the case of pure dislocation plasticity, outside of "fracture" there are collective effects (see the review of Zaiser for an outline [155]), which often need to be treated with the tools of statistical mechanics. Examples of collective behavior are the Portevin-LeChatelier effect [156], and the temporal and spatial fluctuations in dislocation dynamics [138, 157]. One would like to understand the laws of damage accumulation and how to define a RVE or correlation length [134, 158–162]. The plastic deformation develops in non-crystalline materials patterns, whose statistical structure is largely not understood (see e.g.. Ref. [163]) though simple models have been devised [164]. These questions could also be studied again via statistical mechanics ideas and models.

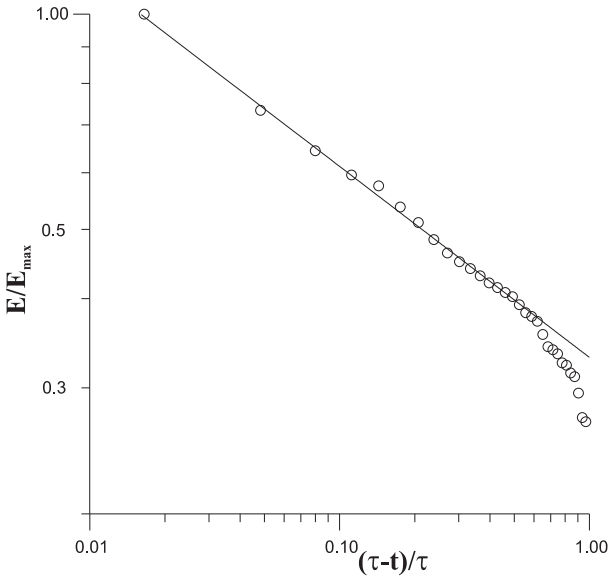


Figure 23. The cumulative energy E, normalized to $E_{max}$, as a function of the reduced control parameter $(\tau - t)/\tau$, plotted in the proximity of the failure in the case of a constant applied load (pressure). The circles are the averages, for 9 wood samples. The solid line is a trial fit $E = E_0 \left(\frac{\tau - t}{\tau}\right)^{-\gamma}$. According to Ref. [124], $\gamma = 0.26$, is independent of the "load". Note the range of $E$ in which the scaling seems to apply.

## 4 Statistical models of failure

In the following we establish the rules of the game. We consider models with interacting elements, whose coarse-grained behavior captures the key features of fracture processes in the presence of *randomness*, that can be either *annealed*

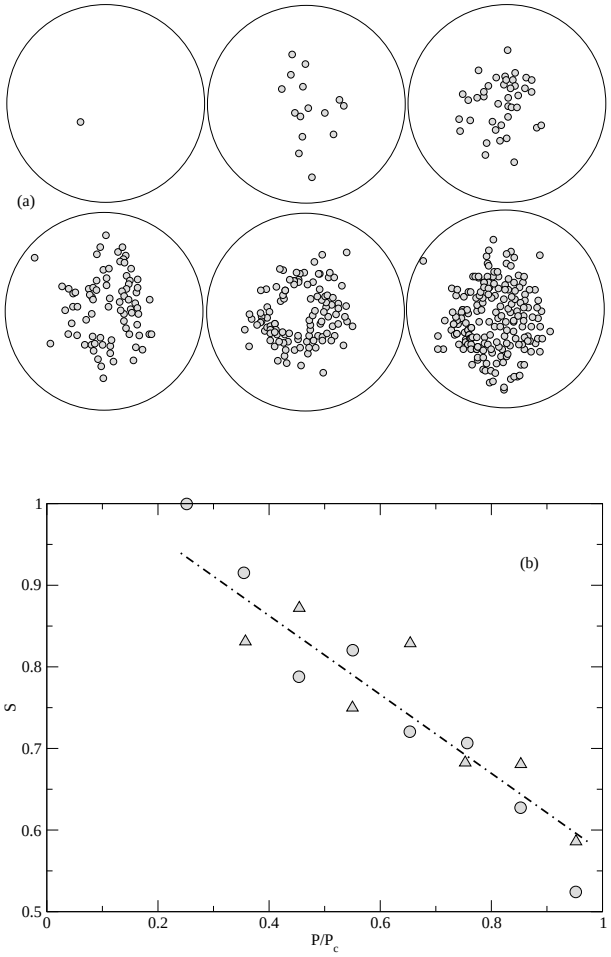


Figure 24. a): the microfractures localize (in 2D) as the control parameter is increased. The final panel has all the located events from the five equidistant intervals in five subplots (from Ref. [122]). Note that any localization experiment typically misses some events that can not be placed with certainty. b): The entropy, which decays roughly linearly from one (corresponding to random locations) as the final fracture is approached for the pressure (control parameter) value of $P/P_c = 1$.

(thermal) or *quenched* (frozen). Moreover one may consider models in which one incorporates a history effect. A typical case would be where the damage accumulated by individual elements would be a monotonically increasing stochastic function of its stress-history. The simple rules used are then intended to capture the behavior of materials on the mesoscopic level ranging from brittle to perfectly plastic to viscoelastic. Another extension concerns models with inertia, so that sound waves are included. We also briefly take up the issue of connecting these abstract models to the finite element simulations practiced in engineering fracture mechanics and to atomistic simulations. Note

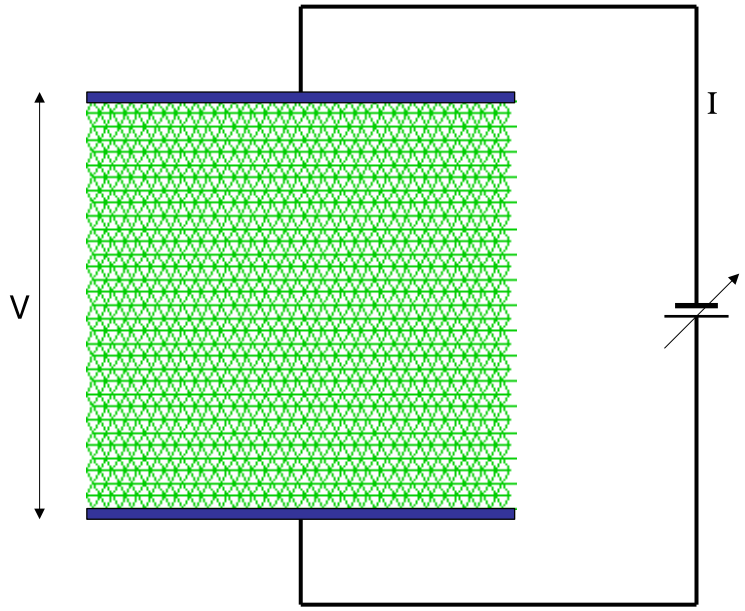


Figure 25. Random thresholds fuse network with triangular lattice topology. Each of the bonds in the network is a fuse with unit electrical conductance and a breaking threshold randomly assigned based on a probability distribution (for example, a uniform distribution). The behavior of the fuse is linear up to the breaking threshold. Periodic boundary conditions are applied in the horizontal direction and a unit voltage difference, $V = 1$, is applied between the top and bottom of lattice system bus bars. As the current $I$ flowing through the lattice network is increased, the fuses will burn out one by one.

again that in this review we on purpose leave aside the well-established field of dielectric breakdown, in spite of its close connections to scalar fracture [22].

### 4.1 *Random fuse networks: brittle and plastic*

The simplest truly interacting fracture models are variations of the scalar analogy of fracture captured by the random fuse model (RFM) [8, 12]. The equations governing the RFM can be considered as a discretization of the continuum Laplace equation

$$\nabla^2 V = 0 \tag{35}$$

with appropriate boundary conditions (see Fig. 25). This scalar electrical analogy of elasticity is a simplification over the Lamé equations (Eq. (10)) described in Sec. 2, and formally corresponds to an antiplanar shear deformation scenario. In the discrete version, the currents and voltages over the nodes $x_{ij}$ satisfy the Kirchhoff and Ohm's laws and depend on the local conductivities

$\sigma_{ij}$ for the links (or resistors between the nodes). The fuse is then simply an element with a property of irreversibility (see Fig. 26): once a critical current (or similarly a voltage drop across the fuse, but if $\sigma_{ij} \equiv 1$ the two cases are perfectly equivalent) $i_c$ is reached, the conductivity goes to zero. Clearly, a model with such fuses is appropriate to describe the failure of very *brittle* media. The failure becomes more gradual in the presence of disorder, since not all the links would fail at the same time. Although much of our focus is on the RFM, many of the issues that we consider are directly applicable to other discrete models as well.

Quenched randomness is usually introduced in the RFM in different ways:

(i) *random thresholds*, extracting the thresholds $i_{c,ij}$ of each link from a probability distribution $p(x)$;
(ii) *random dilution*, removing a fraction $p$ of the links at the beginning of the simulation;
(iii) *random conductivities*, extracting the conductivities $\sigma_{ij}$ of each link from a probability distribution $p_\sigma(x)$.

All these three methods allow to tune the amount of disorder present in the system by changing the distributions or the dilution ratio.

The crossover from weak to strong disorder is mostly studied in the framework *random thresholds* (case 1) using either a uniform distribution in $[1-R, 1+R]$ [165] or a power law distribution $p(x) \sim x^{-1+1/\Delta}$ in $[0,1]$ [166]. The first case interpolates between no disorder ($R = 0$) to strong disorder ($R = 1$), while the second case allows for extremely strong disorder, since for $\Delta \to \infty$ the distribution becomes non-normalizable. The case $R = 1$ is probably the most studied in the literature. Alternatively it is also possible in principle to connect the disorder in the model to a realistic material microstructure by prescribing the fuse properties based on the morphology of the material microstructure (see Sec. 4.3). The effect of percolation type disorder (*random dilution*, case 2) on fracture will be explored in Sec. 5.4. The scenario of quenched *random conductivities* poses an interesting question on how different disorder phases would need to be defined in the case of a RFM [167]. In general, analogous to elastic media with locally varying elastic constants [168] or simply percolative disorder, quenched conductivity variations create correlations among local currents $i$ even in the linear IV-regime. The largest current or stress variations are related to specific, "funnel"-like defects (see e.g. [169]), which plays an important role in the weak disorder limit. Similarly, the use of irregular lattices is analogous to a percolation type disorder. These type of irregular lattice systems have been carried out using spring and beam-type lattice models [20, 170].

The brittle RFM scenario is usually considered in the limit of time scale separation. This implies that the equilibration time of the currents is much

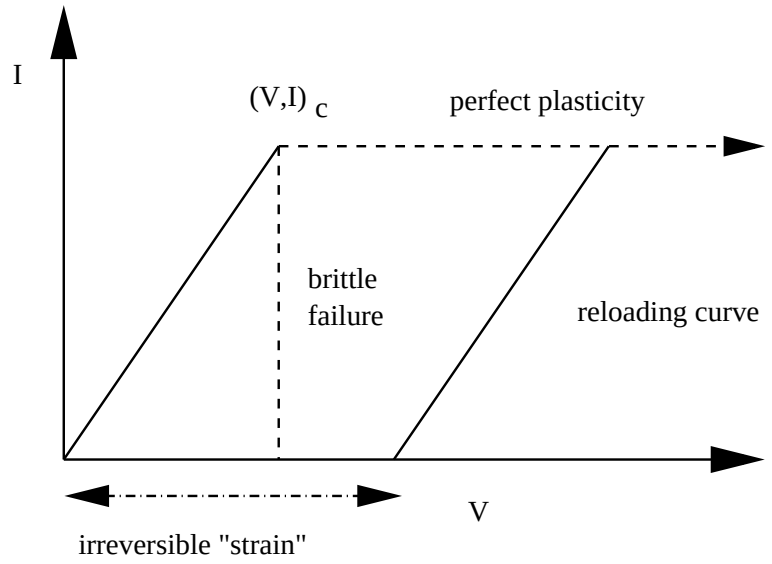


Figure 26. Examples of perfectly brittle and plastic fuses. A fuse undergoes an irreversible transformation from $(V, I)_c$ to $(V_c, 0)$ in the case of a brittle fuse or keeps its current at the yield current ($I_c$ or $I_y$) in the case of a plastic fuse. In the brittle fuse case the response is linear up to $(V, I)_c$. On the other hand, in the plastic fuse case, the unloading tangent modulus is same as the original tangent modulus, and in the fully unloaded state (zero current) there is a remnant "strain" or voltage in the bond.

faster than the ramp-up rate of external potential or current. Moreover, any type of possible overshoots in the local currents $i_{t,ij}$ are neglected (see Sec. 4.4 for discussion on inertial effects). The dynamics is then defined by finding the quantity

$$\max_{ij} \ \frac{i_{t,ij}}{i_{c,ij}} \tag{36}$$

at each timestep $t$. This is an example of *extremal* dynamics, similar to many toy-models that result in "avalanches" of activity. Here the physics ensues from the combination of local current enhancements and disorder, in the thresholds $i_c$. The question is then, whether the latter plays any role or not, and, if it does, what are the consequences for a statistical and dynamical properties of fracture. Instead of successive bond failures of one at a time, for computational convenience, it is also possible to increase the external voltage in steps, and then let *all* the fuses for which the ratio of Eq. (36) exceeds unity fail at once. This of course neglects the small adjustments of the static electric/elastic field that would take place in the usual one-by-one fuse failure dynamics.

This discussion should at this point be made more precise by defining the pertinent quantities. Figure 27 shows a schematic of the $I - V$ behavior of

a RFM. Note that the series of fuse failures defined by Eq. (36) is unique given the set of thresholds $i_c$. The $I-V$ characteristics depends, however, on the way the system is driven: two different $I-V$ curves ensue depending on whether the system is driven by constantly increasing current or voltage. The figure implies that in the voltage driven scenario, there is the possibility of a weakening tail (the regime of $I < I_{max}$ and $V > V(I_{max})$), whereas in the current driven scenario, the curve stops at $(V, I)_{max}$. Hence, depending on the loading scenario, there are two failure points. Under current control all the fuses in the post-peak regime (beyond the peak current $I_{max}$) break at once, whereas in the voltage case fuses in the post-peak regime fail gradually. The schematic presented in Fig. 27 corresponds to a typical simulation in which failure of one bond at a time occurs. In order to obtain the average $I-V$ response, a naive averaging of the $I-V$ responses at constant number of broken bonds may not be the best option since such an averaging will smoothen out the maximum, exactly as if many such systems were in parallel. One way to overcome this problem would be to center first the voltage axis on the breakdown point $V(I_{max})$ of each realization and then average. Alternatively, an average of the envelopes of the $I-V$ curves can be performed at constant voltage values (see Sec. 6.1).

An interesting variant of the RFM is given by the perfectly plastic one. The corresponding fuse response is pictured in Fig. 26: a blown fuse, instead of failing, "yields" so that its current is set to a constant. In this case, the yield iteration proceeds until there is a connected yield path crossing the system, which then blocks any further increase. These systems can be simulated via a "tangent-algorithm" envisioned by Roux and Hansen. The crucial point is that after a fuse yields any further progress along the $I-V$ curve can be considered in a state in which the yielded fuses are simply removed. Then, the $I-V$ behavior will be composed of piece-wise linear parts. The important thing here is the $i_{t,ij}/i_{y,ij}$ ratio, and during each step one subtracts from $i_{y_i j}$ the already existing current. Meanwhile permanent strain (or actually voltage) $V_{pl}$ develops. The tangent modulus or conductivity stays still at the initial value, which means that if the system is allowed to unload to zero current then there will be a remnant voltage, $V_{pl}$, in each of the plastic fuses. Consequently, local *internal stresses* develop in each of the fuse of the lattice system. All this rich behavior arises in a model with simple scalar plasticity and without any time-dependent deformation.

Since the final yield current is connected to the presence of a yield surface, it is possible to understand its properties *without* resorting to actual RFM simulations. The path is given by the solution of the following optimization problem: minimize the value of the path-cost, over all possible configurations,

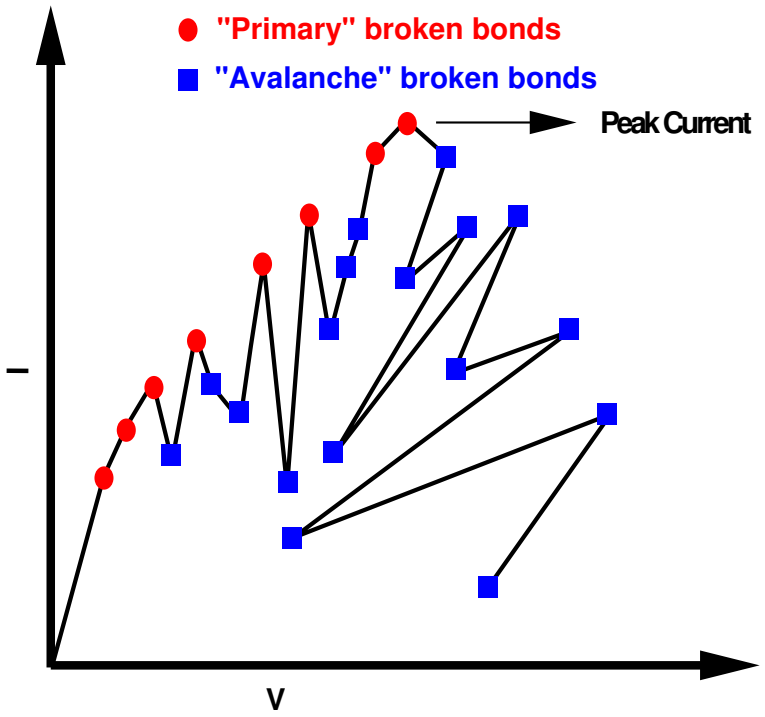


Figure 27. The schematic of a current-voltage curve using RFM. Two alternatives, current- and voltage-driven, are outlined. The schematic corresponds to a failure process in which one bond at a time fails.

when the path energy is given by

$$\langle \sigma_y \rangle L = \sum_{path} \sigma_{ij \in path}. \tag{37}$$

This is exactly the energy of the random bond Ising Hamiltonian at zero temperature (groundstate), so a number of properties are apparent (see [171] for a review). The yield surfaces in $2D$ and $3D$ are self-affine, with the scaling exponents $\zeta_{2D} = 2/3$ and $\zeta_{3D} \sim 0.41$. These can be affirmed by using a mapping (in $3D$) to the max-flow/min-cut problem of combinatorial optimization, and in $2D$ the task maps to the directed polymer in a random medium (DPRM) partition function, which can be connected to the Kardar-Parisi-Zhang equation (KPZ) of kinetic interface roughening [172]. The KPZ problem is exactly solvable, and thus the $\zeta_{2D}$ follows. Further consequences for yield surfaces are the fact that the yield strength fluctuates, with the standard deviation scaling as $L^{\theta}$, where $2\theta = 2\zeta + d - 3$, and $d$ is the dimension ($d = 2$ for 2D and $d = 3$ for 3D). Also, the exact nature of the probability distribution func-

tion (pdf) of fuse yield thresholds is irrelevant, as long as the thresholds are not too strongly spatially correlated, and the pdf does not have too fat a tail (power-law distribution, scaling as $P(i_y) \sim i_y^{-a}$ with $a < 4$).

Finally, it should be noted that simulations of brittle-plastic networks of the kind depicted in Fig. 26 have not been carried out so far. Such networks would present interesting problems to analyze from the theory viewpoint since the scaling properties of fracture surfaces, say $\zeta_{2D}$, are expected to be different. From a computational point of view, one problem is that unloading due to fuse failure causes yielded elements to return to elastic/linear behavior. Furthermore, returning to zero external load nevertheless creates *internal stresses* along with irreversible deformation [173].

It is interesting to mention here that there is a way to interpolate between fully brittle and plastic response. Instead of removing a fuse, it is possible to just reduce its conductivity (akin to softening) by $\sigma_{ij} \to (1 - D)\sigma_{ij}$, where $D$ refers to damage. This leads naturally to crack arrest [174], and thus to distributed damage. If one iterates the procedure ( [175]) so that continuous damage (Eq. (20)) is created by several fracture events per bond, one can observe an effectively plastic $I - V$ curve. Note that the tangent modulus is reduced, but there is no irreversible deformation. Models of this type have been found effective to model biological materials [176], but could also be useful for modeling softening of concrete.

Finally we notice that there are some experimental studies of systems corresponding to realizations of the RFM. Otomar et al. build a network of fuses similar to the numerical models considered in Sec. 6 [177], while a thermal fuse model has been worked out experimentally in Ref. [178]. Such attempts, while being laudatory, also highlight the difficulty of reaching substantial system sizes. Otomar et al. have studied the $I - V$ curves and the dependence of the strength on the effective disorder, which was varied by putting together samples differently. Their experimental results are all comparable to the numerical results presented in Sec. 6.

### 4.2 *Tensorial models*

Following the general strategy of the RFM, several models with more realistic elastic interactions (see Sec. 2.1) have been proposed in the past. The simplest possibility is provided by central force systems, where nodes are connected by elastic springs [179–182]. The random spring model (RSM) is defined by the Hamiltonian

$$H = \sum_{ij} \frac{K}{2} (\vec{u}_i - \vec{u}_j)^2, \tag{38}$$

where $\vec{u}_i$ is the displacement of node $i$ and $K$ the spring constant. The elastic equilibrium is obtained by minimizing Eq. (38), and disorder is introduced in the standard way by either random dilution, random threshold, or random elasticity. Despite the fact that the RSM suffers from the caveats associated with the presence of soft modes, it is still considered quite often in the context of fracture. In terms of continuum elasticity, the discrete triangular central-force lattice model represents an isotropic elastic medium with a fixed Poisson's ratio of 1/3 in two-dimensions, and 1/4 in three-dimensions.

A similar slightly more complicated model is the Born model, defined by the Hamiltonian

$$H = \frac{1}{2} \sum_{(i,j)} \left[ \alpha (\vec{u_i} - \vec{u_j})_{\parallel}^2 + \beta (\vec{u_i} - \vec{u_j})_{\perp}^2 \right]. \tag{39}$$

where $(i, j)$ represents the nearest neighbors of the node $i$, and the summation is carried out over all the nodes in the lattice system. The quantities $(\vec{u_i} - \vec{u_j})_{\parallel}$ and $(\vec{u_i} - \vec{u_j})_{\perp}$ represent the relative displacement of the node $j$ in the directions parallel and perpendicular to the bond $(i, j)$ respectively. In this case, there is a primitive competition between stretching and bending the "bond" between two nodes on a lattice. Note that in the limit $\alpha = \beta$ the Born model reduces to the random spring network (if $u$ is scalar, then it reduces to random fuse network), but otherwise it still lacks one fundamental property of real elastic systems that local rigid rotations cost energy (see Refs. [183,184]).

The most used (and most physically correct) models in this respect are the so-called beam and bond-bending models. One may view this kind of a system as a lattice of massless particles interacting (or connected) by a beam to their nearest neighbors [185]. In the beam models, each beam is capable of sustaining longitudinal ($F$) and shear forces ($S$), and a bending moment ($M$). Following the notation of Ref. [186], one can define three effective parameters $a = l/EA$, $b = l/GA$, and $c = l^3/EI$. For a more generic treatment of 2D and 3D beam models, refer to Ref. [187]. Using standard beam theory, it is possible to relate the beam displacements and rotations ($x$ and $y$ displacements and rotation) to the three forces $F$, $S$, and $M$ using the parameters $a$, $b$, and $c$. The out-of-plane deformations or "buckling" of $2D$ beam lattice models have however not been dealt thoroughly in the literature so far. In the literature, the beam models have often been used to describe the fracture of random fiber networks, as lattice models of composites and paper. In terms of continuum elasticity, the beam models correspond to discretization of Cosserat continuum elasticity. The bond-bending model, on the other hand, attempts to be a generalization

of the central force model [181, 188, 189], whose Hamiltonian is given by

$$H = \sum_{ij} \frac{K}{2}(\vec{u_i} - \vec{u_j})^2 + \sum_{ijk} \frac{B}{2}(\Delta\theta_{jk})^2 \tag{40}$$

where $K$ and $B$ are extensional and rotational rigidities. In the above Hamiltonian, the first term corresponds to the usual extensional energy between neighbors $i$ and $j$, and the second term corresponds to the changes in the angle between two "neighboring bonds" emanating from $i$ to $j$ and $j$ to $k$. This has of course the effect of making such angles rigid and thus resisting local rotations of bonds. The corresponding reactions of the bond bending model are longitudinal ($F$) and shear forces ($S$) that can be sustained by each of the elements of the lattice, and a twisting moment or torque ($M$) at each of the nodes of the lattice system.

The inclusion of bond-bending terms into a triangular lattice system result in a conventional 2D isotropic elastic medium with varying Poisson's ratio values [190]. In particular, even the square lattice system with bond bending terms and next to nearest neighbor interactions is equivalent to a 2D isotropic elastic continuum [190]. On the other hand, the triangular beam model lattice system represents a Cosserat continuum.

The failure condition of these bond-bending and beam lattice models depends on the combination of local torque, longitudinal and shear forces in beam models, or on central and angular forces in the bond bending model. In the beam case a typical fracture criterion is of the type

$$[\frac{F}{t_F}]^2 + \frac{\max(|M_i|, |M_j|)}{t_M} \geq 1 \tag{41}$$

where $t_F$ and $t_M$ are force and moment thresholds respectively, which can be chosen separately for each bond. Similar to the RFM, one can then tune the system by scaling the external load so that only one bond fails at each time. In addition, it is possible to control the relative roles of the two fracture mechanisms by either adjusting the magnitudes of $t_F$ and $t_M$ or adjusting the beam elasticity (slenderness or relative extensional and bending rigidities of the beams). It should be noted that Eq. (41) resembles the von Mises yield criterion. In this respect it is worth pointing out once again that there are no studies of plasticity or elastic-plastic fracture using these vectorial formulations for interactions.

### 4.3 *Discrete Lattice versus Finite Element Modeling of Fracture*

Traditionally both discrete lattice models and standard continuum finite element models are often used for modeling progressive damage evolution in quasi-brittle materials, leading to macroscopic fracture or crack propagation. In the discrete lattice models, the continuum is approximated *a priori* by a system of discrete elements such as central-force spring and beam elements.

With regard to fracture, the standard continuum based finite elements are especially suitable for modeling progressive damage evolution or fracture of homogeneous (at least at the length scale of interest) materials. Simulation of fracture in heterogeneous materials is however complicated by the presence of disorder, whose presence naturally leads to statistical distributions of failure stresses, accumulated damage, acoustic activity, crack shapes and so on. Standard continuum constitutive equations are based on mean-field or homogenization considerations, and hence do not capture the effect of fluctuations as has been briefly discussed in Sec. 2. A few of the recent continuum based investigations however have made progress in explicitly modeling the material disorder to account for its influence on dynamic crack propagation [191–194].

In the discrete lattice modeling of fracture, the disorder can be explicitly modeled. As discussed in Sections 4.1 and 4.2, the medium is described by a discrete set of elastic bonds with randomly distributed failure thresholds, or in the electrical analogy via the fuse model. In the elastic case one can resort according to the continuum elastic description desired to bond-bending models, the RSM, or the beam-type models. These have been used extensively in the mesoscopic modeling of progressive damage evolution in quasi-brittle materials. Sections 4.1 and 4.2 describe how statistical effects of fracture and disorder may be modeled using these discrete lattice systems. Applications of central-force spring elements to model fracture of homophase and heterophase composite materials is presented in Refs. [195–197]. Similarly, Refs. [16–19] present the application of beam lattice models for modeling fracture of concrete structures.

On the other hand, in the continuum mechanics based finite element models, the disorder is quite often implicitly modeled using the homogenization concepts over RVE and by degrading the overall constitutive response (stiffness) of the material based on effective stress and damage variable definitions [17, 24, 25]. In the continuum sense, the fracture of quasi-brittle materials is studied from two different perspectives, namely, the continuum damage mechanics and the continuum fracture mechanics. The continuum damage mechanics deals with the study of crack formation and growth from an initially flaw or defect free structure. In particular, it describes the progressive loss of material integrity due to the propagation and coalescence of microcracks, microvoids, and similar defects. On the other hand, the continuum fracture

mechanics studies how a preexisting crack-like flaw or defect would grow.

Two continuum damage mechanics based approaches are commonly employed at the macroscopic level for modeling damage evolution. In these approaches, the bulk behavior of the material is described by either a phenomenological model [17, 24, 25] or a homogenized micro-mechanics based model. As described in Sec. 2, damage is described by a scalar damage state variable $D$ (or a generic tensorial $\mathbf{D}$). The phenomenological models are based on the notion of an effective stress and the constitutive response of the bulk material is described by a phenomenological strain energy function. An evolution law for damage is prescribed along the gradient of a damage loading surface. Broadly speaking, the continuum damage mechanics formulation parallels that of standard plasticity theories except that the effects of strain softening must be considered in modeling damage evolution leading to fracture.

Homogenized micro-mechanics based damage models [198–201] consider an averaged response of the material microstructural features. In these models, the macroscopic damage description is obtained by homogenizing the material response over a *representative volume element* (RVE) unit cell. The homogenization of the material response, however, is valid only as long as the material is statistically homogeneous. While accounting for short-range local stress fluctuations and multiple crack interactions, the homogenized micromechanics models suffer from the same shortcomings as the phenomenological damage models. In particular, these formulations do not include long-range spatial correlations of cracks and stress fluctuations [198]. In the crack growth and coalescence stages of damage evolution, statistical fluctuations become dominant and homogenization based approaches are not applicable.

It is useful again to compare the RVE size, $a_{RVE}$, to the correlation length, $\xi$. In practice, one needs $\xi \ll a_{RVE}$ for the homogenization to be accurate. Beyond the correlation length, $\xi$, the material can be regarded as statistically local and homogeneous. With the increasing value of correlation length, i.e., as $\frac{\xi}{a_{RVE}} \to 1$, finite size corrections are necessary for homogenization, and the material response changes from a *local* to *nonlocal* behavior [198]. Within the scale $\xi$, statistical fluctuations are dominant, and hence homogenization is not valid. Close to macroscopic fracture, the extreme moments of statistical distribution of microcracks and the corresponding correlation lengths dominate the material response. Under these circumstances, the densities become irrelevant and the concept of RVE ceases to make sense. This drawback in homogenized methods has enabled the more recent investigations to explicitly model the microstructural disorder in finite element simulations [192–194].

An example of continuum damage mechanics based finite element model applied to the fracture of disordered materials such as concrete is the smeared crack approach [17], wherein the cracks are not explicitly modeled. Instead, the constitutive properties of the finite elements where a crack is supposed to

develop are degraded according to some continuum law. That is, instead of considering the crack explicitly as a discrete displacement jump, the effect of crack is smeared over all the Gauss points of the finite elements that contain the crack by degrading the corresponding material properties at the Gauss points. Many such finite element models based on continuum damage mechanics are in common use for modeling damage evolution including strain softening behavior of materials.

On the other hand, in continuum fracture mechanics based finite element models such as the the discrete crack method [17], an explicit modeling of the crack is considered using appropriate interface elements and crack-tip finite elements. The zero thickness interface elements are in general embedded between the edges of two adjacent finite elements and/or along probable crack paths that are decided upon *a priori*. The constitutive behavior of an interface element is governed by a traction-displacement cohesive law, which is used to evaluate interface traction in terms of normal and tangential displacement jumps, or a non-dimensional displacement jump parameter which is zero at the traction free state and equals unity at interface failure. The progressive failure of these interface elements simulates crack propagation. When the remeshing is not performed during crack propagation, the crack path is restricted along the edges of the finite elements. This results in a finite element mesh-orientation dependency of the numerical solution. On the other hand, remeshing in each load step may be considered to alleviate the problem of crack path propagation on mesh layout. However, remeshing techniques [202], which model a discontinuity or crack by modifying the finite element mesh topology to explicitly capture a discontinuity, are computationally expensive and not readily applicable for non-linear problems. Alternative fictitious crack model [203] approaches based on ideas using Dugdale-Barenblatt plastic crack-tip zones are also in common use; however these approaches suffer from similar drawbacks.

During strain localization and softening, the deformation concentrates in regions of finite size. The modeling of this localization process using continuum finite elements is fraught with serious difficulties, both from mathematical and numerical points of view. Mathematically, the onset of strain softening leads to ill-posedness of the rate boundary value problem of the continuum equations [204]. In particular, the governing set of partial differential equations in the standard rate-independent continuum lose their ellipticity for quasi-static loading conditions, while hyperbolicity may be lost locally for dynamic conditions [204]. In analytical solutions, strain softening is characterized by the appearance of infinite strains of a set of measure zero. When the problem is modeled and discretized with finite elements, the localization concentrates in the volume of material capable of representing the set of measure zero, which is a one element in one-dimensional problems or a one element wide line in two-dimensional problems. From a numerical perspective, this ill-posedness

manifests itself in severe mesh dependence of the finite element solution in terms of mesh size and alignment. Hence, the problem of mesh dependency is not intrinsically numerical but stems from the change of the character of the underlying differential equations of the continuum description.

In order to allow for modeling of localization and strain softening in the continuum description, approaches based on strain localization limiters are proposed. The essential idea is to change the character of the equations so that the region of localization does not generate to the set of measure zero but to the physical region that can be deduced from the experimental procedures. In the literature, several regularization techniques (localization limiters) based on spatial nonlocal continuum concepts [205], higher-order gradient theories [206], micro-polar or Cosserat continuum descriptions [204], viscoplastic regularization methodologies [207], and the regularized discontinuous displacement approximations [208] have been presented for capturing the localization phenomena. These approaches ensure that the numerical solutions remain meaningful in the sense that a finite width of the localization zone and finite energy dissipation are obtained even when the localization zone is fully developed. The above localization limiters (regularization techniques) can be classified as integral, differential and rate limiters. Integral or non-local limiters are based on integral strain measures over a finite domain. Differential limiters include strain or stress measures with derivatives of order higher than one. In rate limiters, the time dependence of the strain softening is built into the constitutive equations. Although, each of the above methodologies has its own advantages and disadvantages, from an implementation point of view, differential and rate limiters are the realistic candidates for implementation into existing codes. Non-local limiters are more complex both theoretically and implementation-wise.

In order to eliminate the effects of mesh size and alignment dependencies in the numerical simulation of fracture, finite element methods based on so-called embedded discontinuities [208, 209] within the finite elements are also used. These finite element formulations are based on enhanced assumed strain (EAS) formulations [210], and the displacement jump across a crack is incorporated into a finite element as an incompatible mode in the strain field. Recently, extended finite element methods (XFEM) [211] based on the partition of unity approach [212] are also employed for simulating the fracture of quasi-brittle materials. Although the XFEM has similarities in the modeling of cracks using discontinuous displacement interpolations within the elements, the XFEM is far superior to the discrete discontinuous displacements based finite element approach. To start with, XFEM is capable of representing arbitrary propagation of cracks within the elements with or without bisecting the elements completely [211]. For example, in the mesoscopic fracture simulations, this feature allows for the simulation of transgranular crack propagation

in addition to the usual intergranular crack propagation [213]. Furthermore, XFEM allows for the presence of multiple cracks with secondary branches including their mutual interaction thereby determining the change in the crack orientation. It is possible to enhance these discontinuous interpolations with a suitably chosen near crack-tip fields to achieve a superior coarse mesh accuracy in the simulations. Representing the cracks using a signed distance function based on level set methodology facilitates the evolution of cracks and hence alleviates the necessity to use automatic remeshing techniques and explicit representation of cracks [211].

Even with these vastly improved finite element methodologies and the recent trend in explicitly modeling the material disorder [191–194], fracture simulation of disordered quasi-brittle materials with many interacting microcracks, and long-range spatial crack correlations and stress fluctuations poses a daunting task for current finite element methodologies. In particular, when the macroscopic fracture is preceded by many competing and interacting microcracks, both mathematical and numerical issues arise in assessing which crack should propagate and by how much should it propagate [214]. In this sense, the rigor and accuracy of these homogenized finite element models based on effective medium (or mean-field) continuum theories is limited to moderate damage levels, whereas those based on continuum fracture mechanics is limited to the regime where the behavior is dominated by a single (or few) dominating crack. Currently, the most fundamental challenge is to bridge the gap between the discrete and continuum descriptions of brittle fracture. Recent finite element studies [191–194] that explicitly include the material disorder effects are very promising in this direction.

### 4.4 *Dynamic effects*

**4.4.1** ***Annealed disorder and other thermal effects.*** In reality, on scales that are supposed to be described by the quasi-static models introduced above, fracture processes may also be influenced by time-dependent details. A possibility that has been widely explored in the past is to move from a deterministic dynamics in a disordered system to a stochastic dynamics in an homogeneous system [215, 216].

Time dependent randomness has been implemented in two different ways in the RFM: the failure probability can be chosen to be a function of the instantaneous fuse current, or a functional (such as an integral) that depends on the current history. The first case corresponds to *annealed* disorder, where probability of failure of fuses is given by [21]

$$P_{ij} \sim (i_{t,ij})^{\eta}, \tag{42}$$

properly normalized over all $ij$, such that $\eta$ measures the relative role of current enhancements. In the limit $\eta = 0$, the model is equivalent to screened percolation. In the opposite case of $\eta \to \infty$, the current enhancements always dominate over any randomness (or disorder). It is commonly believed that quenched and annealed disorder lead to similar behavior in such a scenario. The simplest explanation is that one can always find a set of quenched thresholds such that it will exactly reproduce the same sequence of failures as any stochastically induced history [166]. The behavior of the RFM and RSM for various $\eta$ values has been explored both using simulations and mean-field theory [217–225]. A critical value seems to be $\eta_c = 2$ that arises due to a competition of damage accumulation and crack growth. Many issues still remain open, of those to be discussed in Sec. 6, the crack roughness is an example.

In the second case (history dependent failure probability scenario), one may consider the case where the local current $i_{t,ij}$ is followed as a function of time. For example, consider the integrated current, or some power thereof to a fixed threshold, and then use a rule similar to Eq. (42). Under these circumstances, the scenario mimics a creep-like failure due to the external timescale that is now introduced by the integrated history. Consequently, it is most natural to study such models at constant current or voltage since a ramp-up in loading will only complicate the behavior further.

Alternatively, the dynamics may be studied by considering the evolution of an extra state variable, $T$, defined in a manner similar to temperature [226]. The dynamics of $T$ is supposed to obey a state equation given by

$$C\partial_t T = Ri^b - aT. \tag{43}$$

Now, if we suppose that a fuse fails whenever $T > T_c$, where the critical value $T_c$ may be distrbuted uniformly, one again observes two regimes: percolation when $b \to 0$ and strict brittle fuse networks when $b \to \infty$ [226]. For $b \to \infty$, the studied examples involve quenched disorder via local conductance variations. In the intermediate range of $b$'s, the networks develop interesting damage dynamics.

**4.4.2** ***Sound waves and viscoelasticity.*** The dynamics just discussed do not explicitly involve the two relevant time scales of *loading* and *relaxation*. The relaxation time scale in general encompasses two aspects; namely, the time scales that arise due to transient dynamics, i.e, as the microscopic damage takes place ("bonds break") the stress field deviates from its static or asymptotic stationary value, and the relaxation time scales inherently associated with the local dissipative mechanisms such as viscoelasticity. In the lattice models, these local dissipation mechanisms may be introduced locally

on an individual element level.

The transient dynamic effects consider coarse-grained sound waves together with inertial effects. The *perturbations* induced by the dynamics into a quasi-static model can be considered in a time-dependent model through a dissipation mechanism. As an example, let us consider a simple scalar $2D$ model

$$M\ddot{u}_{i,j} = -K \sum_{(l,m)} (u_{i,j} - u_{l,m}) - \Gamma \dot{u}_{i,j}, \tag{44}$$

This could be considered as a dynamical version of a RFM with the masses $M$ and the damping $\Gamma$ included, or a bare-bones simplification of a central-force one. Here the sum of site $(i, j)$ runs over the nearest neighbors $(l, m)$. A constant loading rate (velocities) of $V$ and $-V$ is applied at the two opposite boundaries so that the boundaries move in opposite directions.

The transient dynamics of the system are followed by numerically integrating the Eq. (44), which is a damped wave equation. Each time a bond is stretched beyond its threshold $u_{c,ij}$, the bond is removed from the lattice system. In this scalar model one has only transverse waves, with the sound speed $c = \sqrt{K/\rho}$. With such dynamics, one may monitor the local signal (Fig. 4.4.2) from an "event" which does have some qualitative resemblance with real acoustic events from experiments (Sec. 3). One of the complications associated with transient dynamics simulations is that wave interference and reflections significantly disrupt the accuracy of numerical solution. Consequently, the damping coefficient $\Gamma$ must be chosen such that the waves are damped strongly enough to avoid interference and reflections. This becomes particularly important in problems involving dynamic fragmentation. Another problem commonly associated with transient dynamics is also that close to surface boundaries incoming and outgoing reflections may interfere disrupting the solution.

In the context of elastic waves excited by energy release, there is a multitude of possible mechanisms that are of interest:

- local, transient stresses - due to a wave passing over a point $\vec{x}$ - may induce local failures, similar to a "beam" failure in a lattice beam model.
- interference from several waves and from the descendant fronts of the same wave as it gets reflected by already existing microcracks [228]. The main point is that how these wave interferences amplify the dynamical, fluctuating stress $\sigma(\vec{x}, t) > \sigma_{static}$ beyond its static value.

The consequences of dynamics in controlled (if not completely quasi-static) fracture would most likely be felt in the advancement of crack lines in $3d$ systems; analysis of the related effects indicates that this may induce crack front roughening beyond the otherwise at most logarithmic scaling [229, 230]. In models with distributed damage, the consequences thereof would be rather

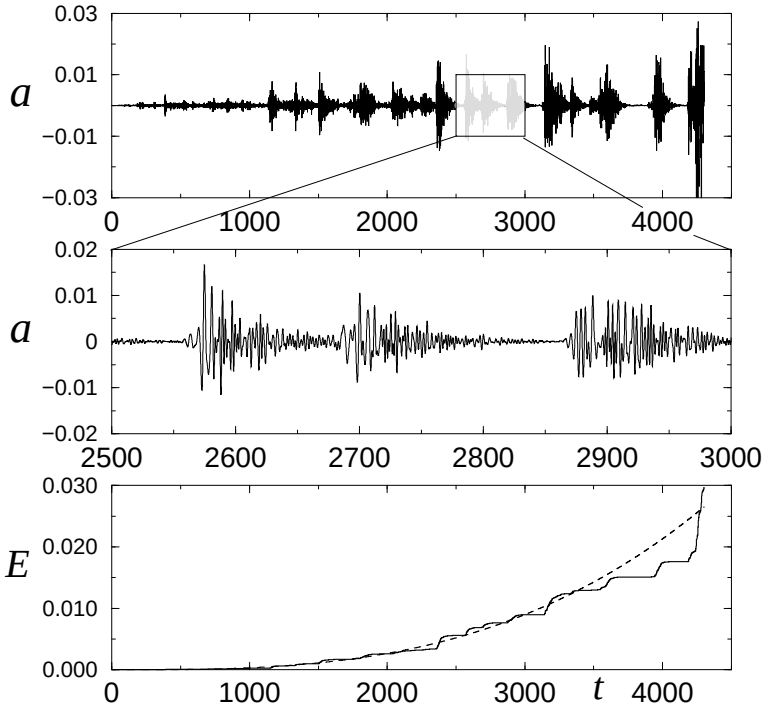


Figure 28. An example of a local amplitude at a site $i$. Clearly, individual events can be distinguished with an envelope that decays as a function of time. The lowest panel presents the integrated wave energy as a function of time. With linearly increasing applied strain, the increase in local amplitude as the failure point is approached is also visible in the time-series of "events" presented in the topmost panels. (see Ref. [227])

.

unclear. One must also recall the attenuation of waves from single source event with distance. It seems to us that it would be of interest to investigate systematically the role of deviations from the quasi-static limit, in particular as the failure point is approached.

The lattice model discussed above is one of many examples used to study dynamical processes. Some of these we have encountered above in the context of DEM, the Discrete Element Method. There is a rather large literature on applying the DEM (also under the pseudonym Particle Method) to various materials problems, in particular to that of fracture behavior of concrete.

A more physics-related application is the study of fast, dynamic crack propagation in $2d$ (for an overview, see [231]). Originally, the question arose how such simple models [232] would relate to the crack velocity vs. time, its asymptotic value in relation to the Rayleigh velocity, and the possible pattern formation. The models are studied either by taking the continuum limit, by simulations,

or by considering in detail the effects induced by the discreteness. The phenomenon of lattice trapping is an important consequence of such studies.

Various authors have elaborated on the crack branching, in particular on the role of crack velocity oscillations, damping, and the exact microscopic force relation and so forth. There is however little overlap with statistical mechanics aspects such as the disorder in the samples, thermal effects and the thermodynamic aspects (where does the released energy go?). The same holds for various phase-field models of fracture [233–236]. In these models, one combines two fields: one for the elastic deformations such that a minimal choice for elasticity (e.g. in $2d$) holds, and another one that allows for a order parameter $\rho(\vec{x})$ that continuously interpolates between undamaged ($\rho = 1$) and failed ($\rho = 0$) states. The models are designed in order to simulate fast fracture propagation and the concomitant pattern formation. In the simplest form, phase-field models do have the problem that a crack is formed due to the presence of "sharp interfaces", with an intrinsic thickness or length-scale. These interfaces separate regions of the phase field $\rho = 1$ where the material is intact from completely broken ones ($\rho = 0$). The interface width is a fixed parameter which gives a minimum FPZ scale.

There are no attempts to apply such models to situations with randomness, and perhaps one may imagine that there are difficulties in justifying physically the choices applied for the noise that one would add. For example, it is conceivable that one might start from a fourth-order Ginsburg-Landau -style free energy describing the intact and failed phases, and couple that to a field term that establishes a local preference ("toughness" or local strength). However, it is not clear how to adjust the noise strength in relation to the intrinsic FPZ size.

One further possibility is to induce dissipation in lattice models such that the time relaxation effects are directly incorporated into the equations of motion. This can be done simply on the model level by applying rules from dashpot-style models of viscoelasticity [237–239]. One possibility is the Maxwell model in which the force $f_{ij}$ acting through bond $ij$ is given by

$$\frac{\partial f_{ij}}{\partial t} = \frac{\partial f_H}{\partial t} - \frac{1}{\tau} f_{ij} \tag{45}$$

Here $\tau$ is a phenomenological damping constant, and has the effect of relaxing the local forces. $f_H$ is the contribution of a Hamiltonian, induced by the displacements of nodes. One could use any particular choice for it, scalar or vector. The system behavior is controlled by the ratio of two timescales: $\tau$ and the strain-rate (or rate of loading). In a model that includes inertia effects, there exists another time scale related to the dynamics of the system, and hence many kinds of behavior could be foreseen. Other possible examples

instead of Eq. (45) would be Kelvin and Voigt -types, which include damping in parallel to a spring. The corresponding response functions are of the form

$$\dot{\epsilon} = \dot{\sigma}/E + \sigma/\tau, \text{Maxwell} \tag{46}$$

$$\sigma = E\epsilon + \tau\dot{\epsilon}, \text{Kelvin} - \text{Voigt} \tag{47}$$

$$\sigma + \tau_1\dot{\sigma} = E(\epsilon + \tau_2\dot{\epsilon}), 3 - \text{parametermodel} \tag{48}$$

with appropriate boundary conditions. All these models result in so-called creep and relaxation functions after the application of a unit stress or strain, as can be seen by the presence of the appropriate relaxation times $\tau$, $\tau_1$ and $\tau_2$ in the equations. Qualitative simulations of Maxwellian models have witnessed as one could expect increased tolerance to damage and crack meandering. This scenario arises due to the blunting of microcracks, and the fact that the local stresses are dissipated in the course of time. However, these models face certain challenges in dealing with boundary conditions, and stress-waves that originate from microfailures.

### 4.5 *Atomistic simulations*

In all materials the ultimate process leading to fracture is of course the breaking of bonds at the level of individual atoms. This is true regardless of whether one considers metals with a crystal lattice, amorphous materials or fiber-matrix composites. In the fiber-matrix composites, it may be that the important phenomena take place on a mesoscopic scale, however for crystalline solids (with dislocations present) it is clear that the fracture energy and the favored mechanisms of crack advancement depend in a fundamental way on atomistic effects. Since fracture is also crucially dependent on long-range elastic fields, one needs to consider processes on large, coarse-grained scales. The main question is thus how to bridge the length-scales from atomistic to continuum elasticity. A current trend is to consider *multi-scale modeling* in which one uses microscopic, even quantum-mechanical input to set up final simulations using the finite element method (see for example, Ref. [240]).

A more fundamental problem is the following: since damage and deformation on the atomistic level typically involve thermally activated or Arrhenius-processes, it is technically difficult to simulate a sample long enough to reach realistic conditions. Numerically accessible timescales are in fact in the range of picoseconds, much smaller than the normal laboratory scales on which fracture operates. One may of course try to circumvent this problem by using idealized systems like Lennard-Jones crystals [241–243]. This has been somewhat popular for the last 20 years, and the crux of such simulations is that a prepared LJ crystal is subjected to shear or tension, leading finally to failure

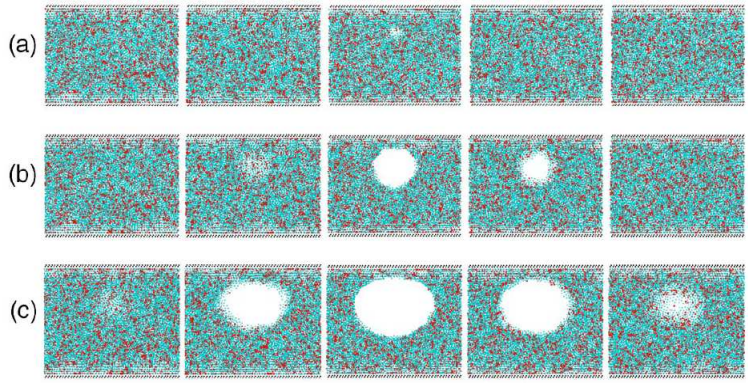


Figure 29. Void initiation and subsequent growth in a binary LJ mixture. Each of the three rows represents five cross-cuts across a 3D system, while the rows themselves correspond to snapshots taken beyond the maximum stress (from Ref. [245]).

exactly as in ordinary lattice models. In this case, however, one may incorporate a finite temperature and rudimentary dislocations and their dynamics. Very large scale simulations by Abraham et al. [244] have demonstrated many fundamental phenomena in single crystal failure, namely, dislocation emission, sound waves and crack acceleration. As an example of recent application of this approach to phenomenological studies [245, 246], we show in Fig. 29 the formation of voids in a three-dimensional study of a binary amorphous LJ system.

More elaborate potentials are then needed to make prediction on any real material, but the scenario gets even more complicated. For the elastic modulus, in many cases the available semi-empirical (to say nothing about full quantum mechanical ab-initio calculations) potentials allow relatively good quantitative accuracy. It is not clear, however, to determine the best possible way to define the condition for the failure of an atomic "bond" when a particular N-body potential is used. On a quantum mechanical level this concept makes no sense, and on a classical level one has to resort to ad hoc techniques. In addition, anharmonicity plays a significant role in such calculations.

In spite of these difficulties, in recent times, there have been significant developments in using such atomistic simulations to study void growth in dynamic fracture of ductile metals, void growth ahead of the crack tip in silicon oxide and carbide, and crack propagation in single-crystal silicon [240, 247–250]. Another theme where progress is being made is in the context of failure of nanotubes [251]. However, such atomistic calculations are not yet at the level where they can be connected with mesoscale disorder, not even in the case of carbon nanotubes where fundamental issues still remain. The exception might be simulations of dynamic fracture, where in spite of the simplifications of

the potentials used one can nevertheless demonstrate fundamental phenomena [250]. We would however like to underline that even in such cases there have not been many studies of fracture as a stochastic phenomenon, with all the phenomenology that it involves.

## 5 Statistical theories for fracture models

The lattice models for fracture introduced in the previous section are reminiscent of other models studied in non-equilibrium statistical mechanics. It is thus tempting to apply standard theoretical tools to understand their behavior and explore the analogies with other systems. This program turns out to be extremely complicated, due to a complex interplay between long range interactions, irreversibility and disorder. We discuss here the solution of simplified models (fiber bundles) and draw analogies between fracture and phase transitions. The fracture process is conveniently analyzed in the framework of interface depinning when disorder is weak, while the case of strong disorder is better viewed in the context of percolation. While these theoretical approaches provide a useful guidance, a complete understanding of the problem has not yet been reached.

### 5.1 *Fiber bundle models*

One of the simplest approaches to analyze fracture in disordered media is represented by the study of fiber bundle models [13, 14]. These models were originally introduced to describe fibrous materials, schematizing the sample as a set of brittle fibers loaded in parallel. As in other lattice models, the failure threshold of each fiber is randomly chosen from a distribution. Next, one has to impose a rule for load redistribution after each failure. The simplest possibility is the case of an equal load sharing (ELS), in which each intact fiber carries the same fraction of the load. This case represents a sort of mean-field approximation and allows for a complete analytic treatment [14, 252–255]. At the other extreme lies the local load sharing model (LLS) where the load of a failed fiber is redistributed to the intact neighboring fibers [217, 220, 256–264]

These simplified models serve as a basis for more realistic damage models such as the micromechanical models of fiber reinforced composites which take into account stress localization [256, 258, 259], the effect of matrix material between fibers [217, 220, 256, 258, 260–262], and possible non-linear behavior of fibers [265]. Other generalizations of the fiber bundle model include viscoelastic couplings [266–268], continuous damage [269], plasticity [270] and thermally activated fracture [271–273]. Fiber bundle models have been used in the past to address the macroscopic constitutive behavior, the reliability and size scaling

of material strength, and the avalanches of fiber breaks preceding ultimate failure [252–255].

**5.1.1** ***Equal load sharing fiber bundle models.*** We consider first the case of ELS fiber bundles, in which $N$ fibers of unitary Young modulus $E = 1$ are subject to an uniaxial load $F$. Each fiber $i$ obeys linear elastic equation up to a critical load $x_i$, which is randomly distributed according to a distribution $p(x)$. When the load on a fiber exceeds $x_i$, the fiber is removed. Due to the ELS rule, when $n$ fibers are present each of them carries a load $F_i = F/n$ and consequently a strain $\epsilon = F/n$. The constitutive law for ELS fiber bundles can be easily be obtained from a self-consistent argument. At a given load $F$, the number of intact fibers is given by

$$n = N\left(1 - \int_0^{F/n} p(x)dx\right). \tag{49}$$

Rewriting Eq. (49) as a function of the strain, we obtain the constitutive law

$$\frac{F}{N} = \epsilon(1 - P(\epsilon)), \tag{50}$$

where $P(x)$ is the distribution obtained from $p(x)$. As a simple illustration, we consider a uniform distribution in $[0, 1]$, so that Eq. (50) becomes

$$f = \epsilon(1 - \epsilon), \tag{51}$$

where $f \equiv F/N$. Similarly we can obtain the fraction of intact fibers $\rho \equiv n/N$ from Eq. (49) $\rho = 1 - f/\rho$ which can be solved to yield

$$\rho = (1 + \sqrt{1 - 4f})/2. \tag{52}$$

This equation shows that as the load is increased $\rho$ decreases up to $f_c = 1/4$ at which $\rho = \rho_c = 1/2$. For larger loads Eq. (52) displays no real solution, indicating the onset of catastrophic failure. It is interesting to rewrite Eq. (52) as

$$\rho = \rho_c + A(f_c - f)^{1/2}, \tag{53}$$

with $\rho_c = 1/2$, $f_c = 1/4$ and $A = 1$. In fact, this form is generically valid for most distributions $p(x)$. To see this we rewrite Eq. (49) as $f = x(1 - P(x))$ where $x \equiv f/\rho$ is the load per fiber. Failure corresponds to the maximum $x_c$

of the left-hand side, after that there is no solution for $x(f)$. Expanding close to the maximum we obtain $f \simeq f_c + B(x - x_c)^2$, which then leads to Eq. (53) as long as the distribution is sufficiently regular (for a discussion of the limits of validity see Ref. [274]). This law also implies that the average rate of bond failures increases very rapidly before fracture:

$$\frac{d\rho}{df} \sim (f_c - f)^{-1/2}. \tag{54}$$

The preceding discussion focused only on average quantities, but the presence of a random distribution of failure thresholds necessarily leads to fluctuations. Due to the ELS rule, however, strength fluctuations are not particularly interesting and vanish in the limit of large bundles. In particular, for any threshold distribution such that $1 - p(x)$ goes to zero faster than $1/x$ for $x \to \infty$, the strength distribution is Gaussian with average $f_c = x_c(1 - p(x_c))$ and standard deviation $\sigma = x_c p(x_c)(1 - p(x_c))/\sqrt{N}$ [14]. More interesting fluctuations are found in the precursors: the load redistribution after a failure event can lead to avalanches of subsequent failures. This process can be treated analytically considering the sequence of external loads $\{F_k\}$ at which some fiber fails [252–254]. After $k - 1$ failure event, the next fiber will break at a load $F_k = (N - k + 1)x_k$, where the thresholds $\{x_k\}$ have been ordered. On average we have

$$\langle F_{k+1} - F_k \rangle = (1 - P(x_k))p(x_k), \tag{55}$$

and close to global failure it vanishes as $\langle F_{k+1} - F_k \rangle \sim x_c - x_k$. In addition, one can see that $\langle (F_{k+1} - F_k)^2 \rangle$ goes to a constant as $x \to x_c$. Hence, the external load $\{F_k\}$ performs a biased random walk, and the bias vanishes as $x \to x_c$. When the load is fixed, an avalanche is defined by the return of the variable $F_k$ to its initial value. For instance, given that the first fiber fails at load $F_1$, the avalanche proceeds until $F_k > F_1$. The process is then repeated from $F_k$, obtaining a series of avalanches whose size $s$ is given by the first return time of the $\{F_k\}$ stochastic process. Thus the avalanche size distribution is equivalent to the first return time distribution of a biased random walk [254]. For a unbiased random walk, this distribution is given by $D(s) = s^{-3/2}$ so that the avalanches just before global failure decay as a power law. When the load is smaller than the critical load, the power law is exponentially cut off and the distribution becomes

$$D(s, f) \sim s^{-3/2} \exp(-s/s_0), \tag{56}$$

where $s_0 \sim (x_c - x)^2 \sim (f_c - f)^{-1}$, diverging as $f \to f_c$ is the limit $N \to \infty$.

Eq. (56) refers to the avalanches at a fixed value of the load $f$. If instead we consider the integrated avalanche distribution obtained when the load is increased from zero to complete failure, we obtain

$$D_{int}(s) \sim s^{-5/2}, \tag{57}$$

as can be seen integrating Eq. (56) over $f$. Recently the difference between the integrated distribution, decaying as $s^{-5/2}$, and the distribution sampled in a small bin, decaying as $s^{-3/2}$, has been rediscovered and reinterpreted as a crossover indicating imminent failure [275]. In fact there is no crossover: the distribution *at each load* $f < f_c$ has an exponent 3/2 as stated Eq. (56), but the cutoff prevents to see in practice the power law unless $f \simeq f_c$.

**5.1.2** ***Local load sharing fiber bundle models.*** The case of LLS represents another extreme case in which the effect of long-range stress field is completely neglected but stress enhancement around the crack is treated in the simplest way. Consider for instance a one dimensional series of fibers loaded in parallel with random breaking threshold from a distribution $p(x)$. When the load on a fiber exceeds the threshold its load is redistributed to the neighboring intact fibers. Thus the load on a fiber is given by $f_i = f(1 + k/2)$, where $k$ is the number of failed fibers that are nearest neighbors of the fiber $i$ and $f = F/N$ is the external load [256]. Even for this apparently simple one dimensional model a closed form solution is not available, but several results are known from numerical simulations, exact enumeration methods or approximate analytical calculations. The analysis of the LLS model is extremely complicated and we thus list here the main results obtained, referring the reader to the relevant literature for the details [217, 220, 256–264].

Contrary to the ELS model, LLS fiber bundles normally exhibit non-trivial size effects as could be anticipated from general consideration of extreme value statistics. In particular, the average bundle strength decreases as the bundle size grows as

$$f_c \sim 1/\log(N), \tag{58}$$

so that an infinitely large bundle has zero strength. The difference in the size effects between LLS and ELS is apparent in Fig. 30 where the constitutive law of ELS fiber bundles is compared with that of an equivalent LLS model for different fiber bundle system sizes. The LLS follows the ELS law at small strains but fails before the ELS critical load. In addition, the failure point in the LLS model decreases as the lattice size is increased. In the limit of large

$N$, it has been shown that the strength distribution should follow the form

$$W(f) = 1 - [1 - C(f)]^N, \tag{59}$$

where $C(f)$ is a characteristic function, close to the Weibull form, but difficult to determine exactly [256]. The existence of a limit distribution has been recently proved under very generic conditions for the disorder distribution in Ref. [276]. This result implies that in LLS bundles there is no disorder induced transition from brittle failure, ruled by extreme value statistics, to a more gradual tough regime where fibers break gradually. The physics and mathematics of this problem is ruled by the determination of critical defects, and it is often so that one needs very large samples to meet some of these important critical defects (see Ref. [276] for a discussion about various LLS models).

The avalanche behavior has also been studied both numerically [253] and by analytical methods [255]. While initially it was believed that LLS would also exhibit a power law avalanche distribution similar to ELS, it was later shown that the power law is only apparent and restricted to a small region. In fact, the integrated avalanche distribution is well approximated by

$$D_{int}(s) \sim s^{-4.5} \exp(-s/s_0) \tag{60}$$

where $s_0$ is independent on $N$.

**5.1.3** ***Generalizations of fiber bundle models.*** Fiber bundle models with ELS and LLS represent two extreme idealizations of fibrous materials that provide some insight on the general failure properties of disordered systems. These models have been improved in various ways, to obtain a more realistic representation of fibrous composites through a more detailed description of their mechanics and by including the effects of disorder on more complicated constitutive laws. There is a vast literature on the effect of the fiber arrangement, for instance two dimensional arrays rather than a one dimensional chains have been considered. Furthermore, it is possible to interpolate between LLS and ELS behavior through a long-range load transfer rule [269, 277], or by a mixed mode in which a fraction of the load is transfered locally and the rest globally [278]. In both cases one observes a crossover between local and global behavior as a function of the parameters of the model. In particular, in Ref. [277] the authors use a load transfer law decaying $1/r^\gamma$, where $r$ is the distance from the broken fiber, and study the failure process as a function of $\gamma$. For $\gamma$ close to zero, they recover the ELS result, while the LLS results is found for large $\gamma$. The two regimes are separated by the point $\gamma_c \simeq 2$. This model is interesting because it makes contact with lattice models for fracture where

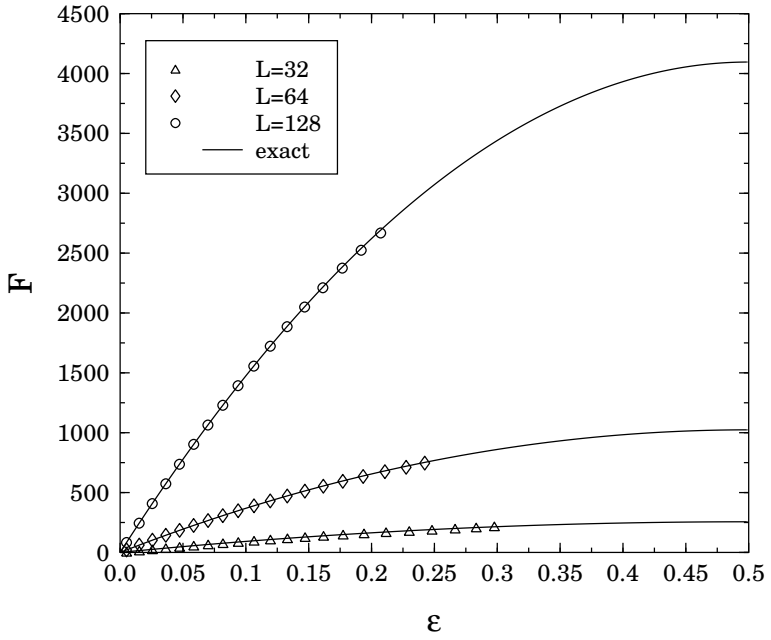


Figure 30. The constitutive law for the ELS model Eq. (51) (solid line) is compared with the local stress transfer model. Increasing the system size $L$, the failure stress decreases in the LLS model (from Ref. [269]).

stress is generally transfered in a non-local, but geometrically dependent, fashion. Interestingly, for the two dimensional random fuse model the current is redistributed with a law decaying as $1/r^2$, exactly the crossover point between local and global behavior. We will elaborate further on this relation in the next section.

The variable load transfer rule also allows to study the patterns of damage using $\gamma$ as a control parameter, as does the version where perfect plasticity is included [270]. In the latter case, with LLS one can have a growing crack which turns out to be compact, with a rough perimeter. The connected cluster of broken fibers can also percolate forming a particular case of a percolation transition. This is slightly different from the damage patterns observed in more realistic - even RFM - models, which are isotropic. Last, in the partly plastic FBM the avalanche size distributions of bursts deviate from their LLS/ELS behaviors [270]: the scale-free nature vanishes with ELS, while there is a special value of remnant load in a yielded fiber, that seems to induce a power-law even with LLS.

Next, we discuss in more detail some time dependent generalizations of fiber bundle models. In viscoelastic fiber bundles [266–268] each fiber obeys a time

dependent constitutive equation of the type

$$f = \beta\dot{\epsilon} + \epsilon, \tag{61}$$

where $f$ is the external load, $\beta$ is a damping coefficient and the Young's modulus is unitary. In a creep test (i.e. constant load test), one thus finds that the strain evolves according to

$$\epsilon(t) = f(1 - \exp(-t/\beta)) + \epsilon_0 \exp(-t/\beta) \tag{62}$$

where $\epsilon_0$ is the initial strain. Fibers fail when the local strain $\epsilon$ exceeds a random threshold $x_i$, taken from a distribution $p(x)$, and its load is redistributed. Here we discuss the ELS case, the generalization to LLS being straightforward. The asymptotic behavior of the model is the same as in the time independent model since the Hooke's law is eventually valid when $t \gg \beta$, but the order of individual failures is different. The time dependent constitutive behavior of the model is obtained by solving the self-consistent equation

$$f = (\beta\dot{\epsilon} + \epsilon)(1 - P(\epsilon)), \tag{63}$$

reducing to Eq. (50) in the steady state regime. A typical example of the time evolution for different values of the loads is reported in Fig. 31. From this we can expect that the bundle will eventually fail for $f > f_c$ and resist otherwise. The time to failure can be evaluated from Eq. (63) and is found to diverge as $t_f \sim (f - f_c)^{-1/2}$ as $f \to f_c$. Notice that in the LLS version of the model one still observes a transition but $t_f$ does not diverge as $f \to f_c^+$ [267].

Another interesting time dependent generalization of the fiber bundle model considers thermally activated fracture [271–273]. The additional ingredient that is added to the model, typically in the ELS approximation, is the presence of an uncorrelated Gaussian noise term $\eta(t)$ acting independently on each fiber. In particular the noise distribution is given by

$$p(\eta) = \frac{1}{\sqrt{2T}} \exp\left(-\frac{\eta^2}{2T}\right), \tag{64}$$

where $T$ is the temperature in appropriate units. Contrary to the viscoelastic case, the noise has the effect to induce fracture even in subcritical conditions, when $f < f_c$. It is instructive to consider first a bundle without disorder, in which $p(x) = \delta(x - 1)$. Even in this simple case, it is not possible to obtain a general closed form for the failure time, but in the low temperature limit

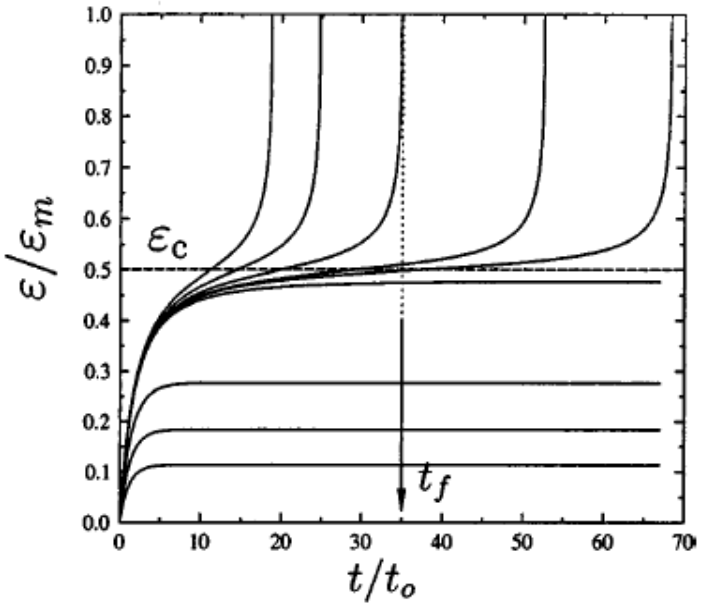


Figure 31. The time evolution of the strain of a viscoelastic fiber bundle for different values of the load $f$. For $f < F_c$ the strain accelerates up to a time to failure $t_f$ (from Ref. [268]).

$T << 1 - f$ case, one can obtain an approximate expression

$$\langle t_f \rangle \approx \sqrt{\frac{2\pi T}{f}} \exp\left(\frac{(1-f)^2}{2T}\right). \tag{65}$$

In the presence of disorder the problem becomes clearly more complicated, but there is an indication that in the low temperature case, the failure time follows a law similar to Eq. (65) with an important difference: the temperature $T$ is replaced by an effective temperature $T_{eff} = T + \Theta$, where $\Theta$ depends on disorder. Hence the net effect of disorder is to enhance thermal activation. It is remarkable that an analogous result was found in Ref. [23] for crack nucleation in a disordered medium.

### 5.2 *Statistical mechanics of cracks: fracture as a phase transition*

The idea that there is a relation between fracture and phase transitions has a long history. For instance, the Griffith theory of fracture is very similar in spirit to the classical theory of nucleation in first order phase transitions. In bubble nucleation, a critical droplet will form when the loss in free energy due

to the bulk forces exceeds the increase in the interfacial energy. Similarly fracture occurs if the external stress prevails over the resistance at surface of the crack. Further analogies come from the scaling behavior observed in fracture experiments, such as for the crack roughness and the acoustic emission distributions. In the following we provide a basic introduction to phase transitions and discuss its relation to fracture using lattice models as an illustration.

**5.2.1** ***Generalities on phase transitions.*** Phase transitions are characterized by changes in the internal symmetries of a material as external control parameters are varied. Familiar examples are the melting of a crystal, or the ferromagnetic transition in a magnet. In the first example, we have an abrupt first-order phase transition, with latent heat, coexistence and no precursors, while the latter is a continuous second-order transition. Notice that one can also observe a first or a second order transition in the very same system, depending on the external conditions, the typical example being the gas-liquid transition that is first order at low temperatures and pressures and becomes second order in a particular point of the PT diagram.

To be more quantitative, one typically distinguishes a phase by an order parameter whose value is related to the internal symmetries of the system. For instance, a ferromagnet acquires a non-zero magnetization when the spin rotational symmetry of the paramagnetic phase is broken. Since the transition is continuous, the magnetization vanishes as the transition is approached. This is unlike first order transitions, where the order parameter is discontinuous across the transition. This case is typically associated also with metastability: when the transition point is reached, the system needs some time to cross into the new equilibrium state. It does so by nucleation: small regions of the new phase are formed, until they become large enough to transform the system completely in a rapid event. In second order transitions, the buildup of the new phase instead occurs before the transition point is reached through the formation of larger and larger correlations that span the entire system exactly at the critical point. This process is encoded in scale invariance: thermodynamic quantities around the critical point are described by homogeneous scaling functions.

To be more concrete and set up the notation, we consider the example of a uniaxial ferromagnetic system. The control parameters, in this case, are the temperature $T$, the magnetic field $H$ and the average magnetization $M$, which is the order parameter of the system. At high temperatures, fluctuations dominate and the magnetization is zero on an average. As the temperature is lowered, the local magnetization becomes more and more correlated until the

critical point $T = T_c$ is reached. The correlation length $\xi$ then diverges as

$$\xi \sim (T - T_c)^{-\nu}, \tag{66}$$

where $\nu$ is a critical exponent. The average susceptibility $\chi \equiv dM/dH$ also diverges, indicating that the system is extremely prone to changes, and it does so as

$$\chi \sim (T - T_c)^{-\gamma}. \tag{67}$$

The order parameter $M$ becomes non-zero in the ferromagnetic phase and close to the critical point follows

$$M \sim (T - T_c)^{\beta}, \tag{68}$$

defining another critical exponent. The presence of a magnetic field destroys the transition, forcing a particular direction for the magnetization, and thus defines another scaling law at $T = T_c$

$$\phi \sim H^{1/\delta}. \tag{69}$$

We have defined a certain number of critical exponents, which are however not all independent, as can be shown by a more detailed analysis. Here, we do not want to go further into these details but just highlight the fact that second-order phase transitions are associated with scaling and a diverging correlation length $\xi$.

A ferromagnet can also be used to illustrate the idea of nucleation, which is at the core of first order transitions. Imagine that the temperature is fixed below the critical point and we instead vary the field $H$. When the field is suddenly increased from a negative to a positive value the magnetization should also change sign, but if the value of the positive field is not so strong then the state with negative magnetization is still metastable. Thus small local changes of the magnetization will be reabsorbed, while large sudden changes will be less favorable for entropic reasons. The system will spend a considerable time in this metastable state before a large enough change occurs. To be more precise, the free energy cost of a spherical droplet of size $l$ is the sum of two contributions: a bulk decrease due to the magnetic field and a surface energy increase: i.e.

$$\Delta F = -4\pi^2 H l^3 + \pi J l^2, \tag{70}$$

where $J$ is the surface energy. If $l > l_c$ the droplet is unstable and a further

increase in droplet size would result in a decrease in its free energy. Thus the nucleation time can be estimated as the time needed to form the first unstable droplet. The analogy with Griffith theory is evident and one could thus associate crack growth with a first order transition from an elastic body to a fractured solid driven by stress.

The difference between first and second order behavior becomes more nuanced when nucleation takes place close to a spinodal point, corresponding to the field at which the metastable state becomes unstable and thus the system is forced to reverse. Strictly speaking, the spinodal point only exists in mean-field theory, but its signatures can be observed even when interaction is long-ranged. The theoretical description of homogeneous spinodal nucleation is based on the Landau-Ginzburg free energy of a spin system in the presence of an external magnetic field. When the temperature is below the critical value, the free energy has the typical two-well structure as depicted in Fig. 32. In the presence of an external magnetic field, one of the wells is depressed with respect to the other, which represents therefore the metastable state. The system must cross a free energy barrier to relax into the stable phase. When the external field is increased, this nucleation barrier decreases, eventually vanishing at the spinodal. The approach to the spinodal is characterized by scaling laws, analogous to critical phenomena, but the reversal is discontinuous and the transition is first-order. The magnetization or the order parameter $M$ scales with the external field $H$ as

$$M - M_s \sim (H_s - H)^{1/2} \tag{71}$$

where $M_s$ and $H_s$ are the values of the order parameter and the field at the spinodal. This law implies a divergence of the quasi-static susceptibility

$$\chi \equiv \frac{dM}{dH} \sim (H_s - H)^{-\gamma}; \qquad \gamma = 1/2 \tag{72}$$

The fluctuations in the order parameter can be related to suitably defined droplets, whose sizes turn out to be power law distributed with an exponent $\tau = 3/2$. For finite-dimensional short-range models, this mean-field picture is expected to fail, since the system will nucleate before reaching the spinodal point. Thus no scaling would be observed in this case, as expected for first-order transitions.

**5.2.2** ***Disorder induced non-equilibrium phase transitions.*** We have discussed above the properties of nucleation and phase-transitions in thermally activated homogeneous systems. In the case of fracture, however, we often deal with a mechanically driven disordered system. An interesting analogy can be

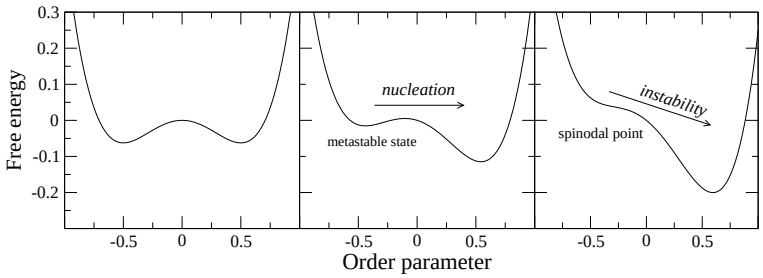


Figure 32. A free energy representation of nucleation. In the absence of a field the system has two equivalent stable states (left). In the presence of a weak positive field one of the two minima becomes metastable and thermally activated nucleation will eventually occur (middle). When the field reaches the spinodal value, the negative minimum becomes unstable (right).

made with the zero-temperature random-field Ising model (RFIM) proposed by Sethna et al. [279–281] in the context of magnetic hysteresis. In this model, a set spins $s_i = \pm 1$ are assigned to the sites $i$ of a lattice. The spins interact with their nearest-neighbors by a ferromagnetic coupling $J$ and are subject to an external field $H$. In addition, to each site of the lattice is associated a random field $h_i$ taken from a Gaussian probability distribution with variance $R$, such that $p(h) = \exp(-h^2/2R^2)/\sqrt{2\pi}R$. The Hamiltonian reads

$$E = -\sum_{\langle i,j \rangle} J s_i s_j - \sum_i (H + h_i) s_i, \tag{73}$$

where the first sum is restricted to nearest-neighbors pairs.

The system is started from a saturated negative state and the external field is increased from a large negative value. At each time the spins $s_i$ take the sign of the local field

$$h_i^{(eff)} \equiv -\frac{\delta E}{\delta s_i} = J \sum_j s_j + h_i + H, \tag{74}$$

where the sum is over the nearest neighbor sites $j$. When a spin $i$ flips, the effective field of the neighbors $j$ is increased by $2J$. This can lead the effective field to change sign inducing an avalanche. For small values of the order parameter $\Delta \equiv R/J$, flipping a few spins generates a big avalanche whose size is comparable to the system size, leading to a discontinuous magnetization reversal. On the other hand, a large disorder prevents the formation of large avalanches and the magnetization reversal is a smooth process. The two regimes are separated by a critical point $\Delta_c$, where the avalanches are distributed as a power law. The behavior of the model in the ($\Delta$, $H$) parameter space is very similar to that of standard equilibrium phase transitions as it is

shown in Fig. 33. In particular, all the usual exponents discussed in Sec. 5.2.1 can be defined replacing $T$ with $\Delta$.

In the mean-field theory, the approach to the instability $H_c$, is characterized by the same scaling laws and exponents of spinodal nucleation, as reported in Eqs. (71)–(72) [280]. In addition, the avalanche size distribution is described by a scaling form

$$P(s) \sim s^{-\tau} f[s(H_c - H)^{\kappa}], \tag{75}$$

with $\tau = 3/2$ and $\kappa = 1$. It is worth noting that these scaling exponents coincide with the mean-field exponents for the distribution of droplets in homogeneous spinodal nucleation. From these studies it appears that the behavior of thermally activated homogeneous spinodal nucleation is similar to the approach to the instability in disordered systems driven at zero temperature. However, one should bear in mind that for a given realization of the disorder the dynamics is completely deterministic in the second case. Concepts such as metastability and nucleating droplets are formally not defined in this context. This picture is only valid in mean-field theory or when interactions are long-ranged. As in conventional equilibrium phase transitions, when interactions are short-ranged nucleation takes place before the spinodal line and scaling laws can be observed only at the critical point.

**5.2.3** ***Phase transitions in fracture models.*** The interpretation of fracture as a phase transition is a highly controversial question. While at first glance the analogies are striking, a precise relation is hampered by several difficulties and no consensus has been reached in the literature on this subject. A series of studies consider the case of crack nucleation in homogeneous media, elaborating on the analogy between the classical theory of nucleation and Griffith theory. Selinger et al. [241–243] have used mean-field theory and numerical simulations to show that a solid under stress is in a metastable state, becoming unstable when the external stress reaches a spinodal point. This is best illustrated with a simple linear chain of particles. It breaks down once one of the pairs gets separated due to a thermal fluctuation that makes the inter-bond to fail. Rundle and Klein [282] have proposed an equation for the growth of a single crack, deriving scaling laws for spinodal nucleation. The nature of the nucleation process in a stressed solid was further analyzed in Refs. [283, 284] using Monte Carlo simulations. More recently, it was shown more rigorously in the framework of elastic theory, that the point of zero external stress corresponds to the condensation point in gas-liquid first order transitions [285]. It is important to remark that these studies deal with the thermally activated fracture where quenched disorder is not considered. The presence of disor-

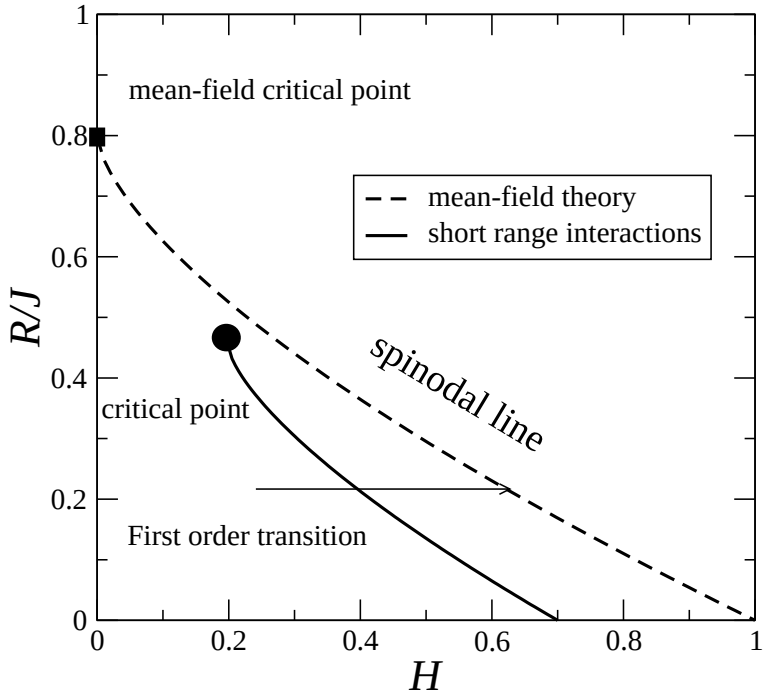


Figure 33. The phase diagram of the non-equilibrium RFIM. The dashed line represents the location of the spinodal, which is obtained from the mean-field theory. When the interactions are short-ranged the reversal occurs on the solid line through a first-order transition. The first-order line ends at a critical point, above which the reversal is continuous.

der, in the form of vacancies or microcracks, strongly affects the nucleation process [242, 283, 284], providing in some cases an effective disorder-induced correction to the temperature [23] as pointed out above in Sec. 5.1.3.

Several authors have tried to relate the scaling laws observed in fracture morphologies and acoustic emission distributions to an underlying critical point, basing their analysis on experiments [121, 124] and models [253, 286–290]. A natural starting point is provided by a lattice model, which could be mapped into other models, typically drawn from ferromagnetism, where the presence of a phase transition is well established [286, 287, 289, 290]. It is instructive to consider first the fiber bundle model, since exact results are available and the nature of the hypothetical phase transition can be clearly identified [286, 287]. To make contact with the RFIM, we can assign to each fiber a spin variable $s_i$, whose value depends on whether the fiber is intact ($s = -1$) or broken ($s = 1$). The effective field is formally given by

$$h_i^{(eff)} = F_i(\{s_j\}, F) - x_i \tag{76}$$

where $x_i$ is the fiber threshold, $F_i$ is the load on the fiber $i$, which depends on the external load $F$ and on the state of the other fibers. The dynamics is now similar to the one of the RFIM since each "spin" follows the local field (i.e. it breaks when $F_i > x_i$). Thus changing the disorder strength and the nature of the load sharing we could obtain a phase diagram of the type depicted in Fig. 33.

In the case of ELS fiber bundles, the load on each fiber is given by $F_i = 2F/(N - \sum_j s_j)$, while for LLS $F_i$ is a complicated function of the state of the neighboring fibers: if a fiber is close to a crack of length $k$ it carries a load of $F_i = F(1 + k/2)$. The crucial difference between these load sharing rules and ferromagnetic interactions is that for fibers the increase of the effective field due to other fiber breaking grows as the fracture process progresses, while in the RFIM this quantity is always given by $2J$. For instance in the case of ELS, the breaking of a single fiber increases the effective field of the others by a quantity $\Delta F = F/(n(n-1))$ which increases as the fraction of intact fibers $n$ decreases. Similarly in the case of LLS each time we break a fiber, we increase the effective field of the neighbor by a quantity $\Delta F = kF/2$ which becomes larger as more and more fibers break.

This difference has a profound effect on the phase diagram, because it implies that interactions always prevail over disorder. Thus, as the system size increases, the system will necessarily hit the low disorder first-order transition line. The only exception is provided by the extreme case of a non-normalizable disorder distribution, where we can always find some strong enough bond to resist the load amplification [274, 288]. In more general cases, however, it is not possible to fine tune the ratio between disorder width and interactions as for the RFIM in order to find a critical point where the two effects are perfectly balanced. Thus the "phase transition" observed in fiber bundle models is always first-order, with a catastrophic nucleation event preceded by some small precursors. The scaling observed in the ELS models is the one associated with a spinodal instability, similar to what is found in the low disorder phase of the RFIM in mean-field theory. When interactions are local, such as for the LLS model, the spinodal line can not be reached and the transition is simply first order. With this idea in mind we can reinterpret the results presented in Fig. 30: as the range of interaction is increased nucleation occurs closer and closer to the spinodal point, as in conventional first-order phase transitions.

Having settled the question of fiber bundle models, we can now turn our attention to more complicated lattice models, such as the random fuse model. The attempts made in the past to map fracture models into spin models are typically based on the lattice Green function formalism: removing a bond $i$ in the lattice implies that the load in the other bonds has to be changed by a quantity $G_{ij}$ (the Green function). Thus we can rewrite the effective field in Eq. (76) in terms of $G_{ij}$ and obtain a suitable spin model. For instance, in the

random-fuse model $G_{ij}$ can be approximated as the dipolar kernel, but only in the limit where only a few bonds are broken. It is interesting to remark that in these conditions the Green function decays as $r^{-2}$ in two dimensions, which is exactly the crossover point between local and global behavior in the FBM. This could imply that the spinodal point, inaccessible under LLS, could be reached in the RFM, as is also suggested by the simulations discussed in Sec. 6.5.

One should take these considerations with due care, since for a generic damage configuration, finding $G_{ij}$ amounts to solving the full problem (i.e. the Kirchhoff equations for the random fuse model) and is thus practically impossible. Thus we can rigorously map fracture models into spin models only in the dilute limit, which is not, however, the limit of interest in fracture. Extrapolating the results of spin models outside their regime of validity leads to inconsistent results, because the stress amplification at the crack tips is not properly captured by the dilute Green function. For instance, the authors of Ref. [289] treat in mean-field theory the spin model obtained from Green function formalism. Neglecting the load amplification in their analysis (i.e. the load transfer is chosen to be independent of the state), they obtain a spurious phase diagram similar to that obtained for the RFIM. Similar problems affect the analysis presented in Ref. [290].

### 5.3 *Crack depinning*

We have discussed in Section 3 that experiments in several materials under different loading conditions, lead to a rough crack surface described by self-affine scaling. The simplest theoretical approach to the problem identifies the crack front with a deformable line pushed by the external stress through a random toughness landscape and the trail of the line yields the fracture surface [91, 97]. The roughness of the line comes from the competition between the deformations induced on the line by the materials inhomogeneities and the elastic self-stress field that tries to keep the front straight. This problem has been studied in full generality and the basic phenomenology applies to a variety of systems including domain walls in ferromagnetic and ferroelectric materials, dislocations gliding through solute atoms, flux lines in superconductors and others.

For simplicity, it is instructive to consider first the case of a planar crack front, corresponding to the experiments reported in Refs. [83–85]. In this case we can schematize the crack as a line moving on the $xy$ plane with coordinates $(x, h(x,t))$ (see Fig. 34) [291–293]. An equation of motion for the deformed line position is obtained by computing, from the theory of elasticity, the variations to the stress intensity factor induced by the deformation of the front. In the

quasistatic scalar approximation, this is given by [294]

$$K(\{h(x,t)\}) = K_0 \int dx' \frac{h(x',t) - h(x,t)}{(x-x')^2}, \tag{77}$$

where $K_0$ is the stress intensity factor for a straight crack. The crack deforms because of the inhomogeneities present in the materials, and these inhomogeneities give rise to fluctuations in the local toughness $K_c(x, h(x,t))$. These ingredients can be joined together into an equation of motion of the type

$$\Gamma \frac{\partial h}{\partial t} = K_{ext} + K(\{h(x,t)\}) + K_c(x, h(x,t)), \tag{78}$$

where $\Gamma$ is a damping term and $K_{ext}$ is the stress intensity factor corresponding to the externally applied stress [291–293]. Eq. (78) belongs to a general class of interface models which have been extensively studied numerically and analytically. For low stress the crack is pinned, and there is a critical threshold $K_c$ above which the crack advances at constant velocity

$$v \sim (K_{ext} - K_c)^{\beta}, \tag{79}$$

where $\beta$ is a scaling exponent, whose value is estimated numerically to be $\beta \simeq 0.68$, while a renormalization group analysis yields $\beta = 2/3$ [295]. Close to the depinning transition crack motion becomes correlated, with avalanches of activity. The distribution of avalanche lengths $l$ follows a power law distribution with a cutoff

$$P(l) \sim l^{-\kappa} f(l/\xi), \tag{80}$$

where $\kappa \simeq 1$ and the correlation length diverges at the transition as

$$\xi \sim (K_{ext} - K_c)^{-\nu}, \tag{81}$$

with an exponent estimated as $\nu \simeq 1.52$ [293]. In addition, the crack front is self-affine, with a roughness exponent given by

$$\zeta = 1 - 1/\nu. \tag{82}$$

Numerical estimates of the roughness exponents range between $\zeta = 0.34$ [291, 292] to $\zeta = 0.39$ [296].

The results of the planar crack propagation model can be compared with the experiments reported in Refs. [83–85]. It is apparent that there is significant

discrepancy between theory and experiments, since the roughness exponent is considerably larger in the latter case. Several mechanisms have been proposed in the literature to account for this discrepancy, but none of them so far is entirely convincing or commonly accepted. The arguments involve correlated disorder [297], elastodynamic effects [293], crack front waves [229] and microcrack nucleation ahead of the main crack [298–301].

The more general problem of three dimensional crack surface roughening can also be recast as a depinning problem, with similar difficulties [230]. It is possible to derive an equation of motion, based on linear elasticity, for the evolution of the crack surface. With respect to the planar crack case, we have an additional equation for the out of plane component $h_\perp(x,y)$ of the crack, while the in-plane component $h_\parallel(x)$ follows Eq. (78). The equation for $h(x,y)$ and the resulting roughness exponent depend on the particular fracture mode imposed in the experiment. Without entering into the details of the derivation, which can be found in Ref. [230], we report here the result. In mode I the out of plane roughness is only logarithmic, while an exponent $\zeta_\perp = 1/2$ is found in mode III. Both results are quite far from the experimental measurement $\zeta \simeq 0.78$, although the mode III result could be in line with the value $\zeta = 0.5$, sometimes measured at small scale (consider also Ref. [92]). Unfortunately, experimental results are normally obtained under mode I loading conditions, at least effectively, while mode III cracks tend to be unstable.

Given the results discussed above, we would conclude that crack roughening is probably more complicated than a simple depinning problem of a linear elastic line moving in a disordered landscape. Nonetheless the depinning picture is quite appealing, since it relates the observed scaling behavior to a non-equilibrium critical point. To obtain a quantitative explanation of the experiments, it is necessary to analyze in detail further modifications of the basic depinning problem, including for instance the combined effects of the anelastic fracture process zone, the formation of microcrack, plastic flow, or elastodynamics. Among these proposals the most promising pathway for future investigation is probably represented by the effect of non-linear elasticity.

The depinning of a non-linear long-range elastic line has been recently studied by renormalization group for contact line depinning, a problem that is formally equivalent to a planar crack [302]. It was shown that adding a non-local KPZ-type non-linearity [1] to Eq. 78 raises the roughness exponent to $\zeta \simeq 0.45$. This value is a little closer to the experimental result, but needs further confirmation, since it is based on a one-loop $\epsilon$ expansion. A more striking similarity is obtained if we consider a non-linear, but local, elastic kernel in Eq. 78. In this case, numerical simulations indicate that the exponent is $\zeta = 0.63$ [303]

[1] The standard KPZ term is $\lambda(\nabla h)^2$, a non-local KPZ term is written in Fourier space as $\lambda q^\alpha |h(q)|^2$

which is in perfect agreement with the experiments. This universality class corresponds to the pinning of the front by a directed percolation path [304, 305]. In order to accept this explanation, we have to understand the mechanism responsible for the screening of long-range forces, resulting in a short-range, but non-linear, kernel. In this respect, recent experiments on amorphous Silica show that the roughness correlation length $\xi$ is of order of the size of the FPZ $\xi_{FPZ}$ [95, 96, 306]. By definition, linear elasticity is not applicable inside the FPZ, where the crack roughening process would takes place. Hence, this observation could be used to justify why the effective kernel is local and non-linear, accounting for the observed value of $\zeta$. While this appears to be a plausible explanation, further work is needed to substantiate this claim.

### 5.4 *Percolation and fracture*

**5.4.1** ***Percolation scaling.*** Adding randomness to brittle lattice models of fracture can be done in many ways, the simplest being the random removal of a fraction of the elements. This process is best understood using the concept of percolation, a particular second-order phase transition that exhibits the full spectrum of usual characteristics, such as scaling and critical exponents as discussed in Sect. 5.2.1 [307]. A percolation transition signifies that a structure becomes *connected* for certain values of the control parameter (i.e. the fraction of intact bonds). The usual example, demonstrated in Fig. 35, is that of bond percolation in a two-dimensional square lattice, where a fraction $p$ of the bonds have been removed. The question is now whether the remaining ones form a connected (or spanning) cluster that extends through the lattice, connecting for instance the two horizontal edges. In this particular example, the spanning cluster is found, in the limit of large lattices, for $p < p_c = 1/2$. As in other second-order phase-transitions, the location of the critical point (i.e. the value of $p_c$) depends on the type of lattice, but the critical exponents are universal.

An important quantity for fracture in the percolation context is the order parameter, usually defined as the probability $\Pi$ that a bond belongs to the spanning cluster. Below the percolation threshold $p_c$, the order parameter scales as

$$\Pi \sim (p - p_c)^{\beta}, \tag{83}$$

with $\beta = 5/36$ in $d = 2$, while $\Pi = 0$ for $p > p_c$. The essential part of describing percolation as a second-order phase transition is that there is a divergent correlation length $\xi$ scaling as

$$\xi \sim (p - p_c)^{-\nu}, \tag{84}$$

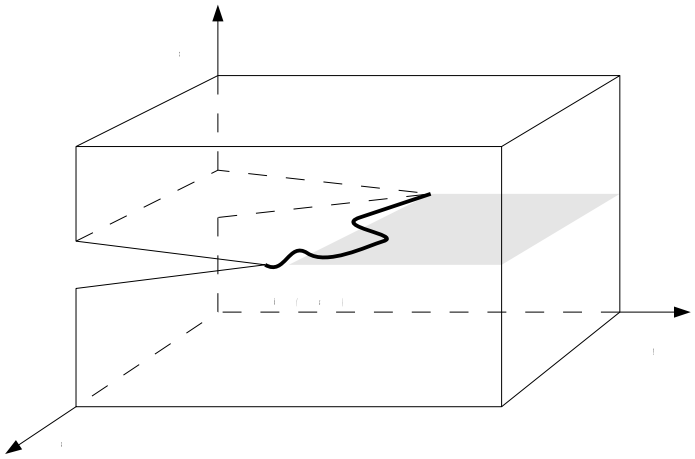

Figure 34. The geometry of a deformed planar crack

with $\nu = 4/3$ in $d = 2$. This correlation length can be measured analyzing the statistics of the clusters of connected bonds for $p < p_c$. The cluster radius distribution is a power law up to a cutoff lengthscale $\xi$. For lengthscales larger than $\xi$ (for the system size $L \gg \xi$ or for distances between two points $r \gg \xi$) the system is out of the critical regime and is either connected or disconnected. For scales such that $r < \xi$, the physics of percolation is governed in general simply by the *singly connected* or "red" bonds. They are - in the bond percolation language - those that make the spanning cluster connected, so that removing any of them also destroys connectedness, or cuts the continuous, spanning path across the sample into two. The sensitivity to the lattice to

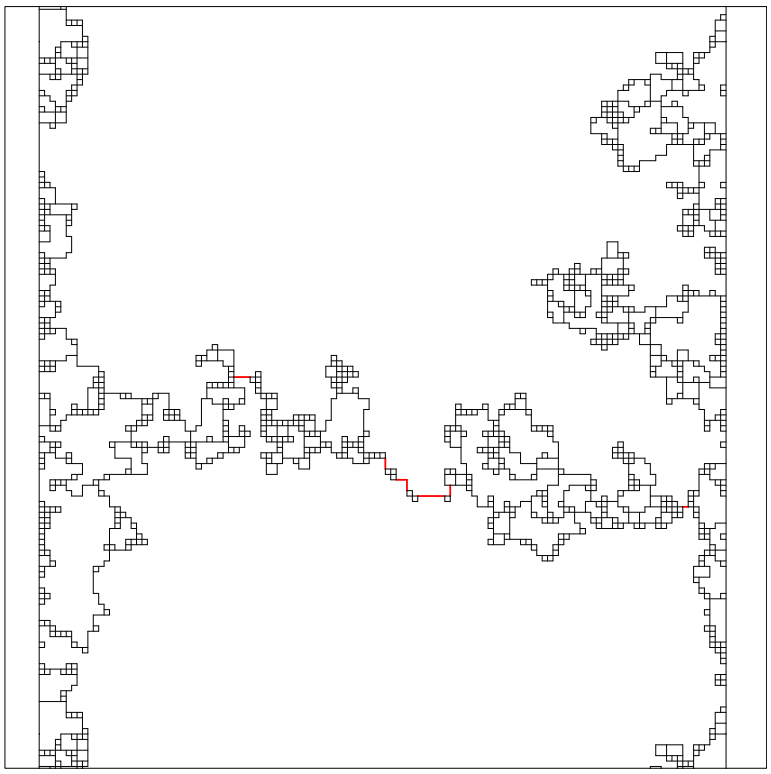

Figure 35. The backbone of a bond percolation problem in $2d$: only the bonds belonging to it are depicted. The "red bonds" are marked, naturally, with red. So-called busbar boundary conditions are used, which makes the backbone more dense close to the boundaries.

small perturbations, like the removal of a red bond, is a signature of criticality.

Red bonds also play a crucial role on various important properties. For instance, if the bonds are taken to be fuses in a RFM, then red bonds will all carry the same current. Thus the conductivity (or equivalently the elastic stiffness in tensorial models) and strength are going to relate to the properties of such bonds. This allows to write down in the critical regions the scaling Ansatz for the conductivity $\Sigma$

$$\Sigma \sim (p - p_c)^{t_\Sigma} f_{perc}(\xi / L^{1/\nu}) \tag{85}$$

such that for $L \gg \xi$ or $p$ large enough but still close to the critical regime, the scaling function $f$ becomes a constant. We have formulated Eq. (85) in terms of a (general) transport exponent $t_\Sigma$, which can also describe any particular physical property from conductivity to maximum current to strength, if the

bonds are taken to be beams with certain elasticity properties. The ratio of the conductivity exponent $t_\Sigma$ to $\nu$ is for instance known to be $t_\Sigma/\nu = 0.9826\ldots$ [308] in $2d$, whereas in $3d$ the ratio is about 2.3 [309]. These questions are often analyzed either numerically via transfer matrix calculations on strips, by renormalization group arguments, or by real-space renormalization, and it appears that the numerical value of most any exponent $t_G$ is non-trivial in the sense that it is not simply related to $\nu$ and the physical dimension.

**5.4.2** ***Variations of the percolation problem.*** Interesting physics is encountered in several separate limits, which concern the nature of the interaction Hamiltonian imposed on the bonds. The difference between elastic and scalar/electric percolation should also be visible in the strength case. At the minimal level, this follows from the scaling of the stiffness and conductivity with $p - p_c$. A fundamental special case arises if the angular or bond-bending part is taken to be zero, exactly, so that only central forces remain. Then the main effect is that single-connectedness is no longer sufficient since simple Maxwell-counting demonstrates that the degrees of freedom are not balanced by the constraints at hand. Several often-used lattices become unstable (e.g. simply cubic ones, like the square one) against deformation. The critical behavior is now called *rigidity percolation*, and its nature is still a not completely resolved question, e.g. with regards to its order in two dimensions - whether it is simply second-order similar to percolation or not [310]. For studies of central-force system fracture in diluted systems the implications are not quite clear either. With increasing damage, at some point, the system will have a vanishing (linear) elastic modulus, while still being geometrically connected.

Another example of percolation-related processes in the fracture context is given by continuum percolation, where one considers the transport properties of a medium with a set of voids or defects. The difference to the lattice case is now due to the fact that the "bottlenecks" of the spanning cluster can have a (naturally) varying distribution of properties. A typical example is the so-called Swiss Cheese -model, where one introduces spherical or circular defects [311,312]. From geometrical considerations, one can now compute the distribution of minimum widths for the narrowest ligaments that one finds on the spanning cluster. The result is that transport properties are changed. In this example, the conductivity is expected to follow $\Sigma \sim (p - p_c)^{T_{sc}}$ with $T_{sc} = (d-2)\nu + \max[\theta, (1-a)^{-1}]$. Here $\theta$ is the resistance exponent of normal percolation, describing what happens between two terminals on the same cluster. The exponent $a$ depends on model and dimension, and describes the power-law distribution of the conductivities of the bottle-necks. One can derive the failure properties easily by noting that all the red bonds carry the same current, but the result depends on what one assumes about the failure

thresholds (see also Ref. [313]).

Finally, an opposite limit to the diluted case is given by the *infinite disorder* case, in which the medium fails following two rules: one picks always the bond with the smallest threshold, and excludes in the process those that do not carry current. Evidently in the beginning this is just dilution, as in geometric percolation, but at some point the *screening* will start to play an increasing role [314]. In this context and in studying fracture close to $p_c$ it might be helpful to use recent algorithmic developments in pruning percolation clusters [315]. These allow to consider only the backbone, and to identify the red, critical bonds, with polynomial time scaling in $L$ and could thus be used to obtain starting configurations for simulations.

**5.4.3** ***Strength of diluted lattices.*** Above the critical region, when the lattice is connected, one can consider the scaling of strength as a function of $L$ and $p$. For simplicity, we restrict our discussion to the scalar case. As noted above, the random removal of bonds naturally leads to a macroscopic reduction of the conductivity from the homogeneous system value. Figure 36 shows an example of the behavior in two dimensions, with fixed $L$ [316]. The crucial argument that relates the strength $\sigma_c(p, L)$ to the extremal statistics arguments underlying the scaling of brittle fracture is due again to Duxbury, Beale, and Leath [316,317]. The most critical defect - this holds also for the elastic case - is a linear one, a row of $n$ missing bonds in two dimensions. In higher dimensions, the corresponding situation is given by a penny-shaped crack and the fuse current will scale as $i_{tip} \sim i_0(1 + k_d n^{1/(2d-1)})$. This results from noticing that the total current increase will scale as $n^{1/2}$, but it is shared by a number of fuses that depends on dimension (e.g. $d = 2$ in $2d$).

Forgetting about rarer configurations where two such cracks are found next to each other, the probability of having a defect of given length is clearly proportional to $P_n \sim p^2(1-p)^n$, times a prefactor which is $L$-dependent from the row length. Thus a connection can be established non-rigorously to the basics of extremal statistics distributions outlined earlier: the critical defect is the biggest found in a sample of transverse size ($L$, usually) and consisting of (again) $L$ independent subvolumes.

From the damage mechanics viewpoint it is useful to take note that in this variant of the RFM the fracture process zone is practically non-existent; thus there is no corresponding lengthscale $\xi_{FPZ} \gg 1$ that might depend on system size. Furthermore, for any $p$ the damage or number of fuses that fails before the maximum current is very small. Thus in these systems there is no "nucleation", the largest defect in the original system dictates the strength.

In particular, the defect population with dilution or percolation disorder is *exponential*, and thus the limiting distribution will be of the double-

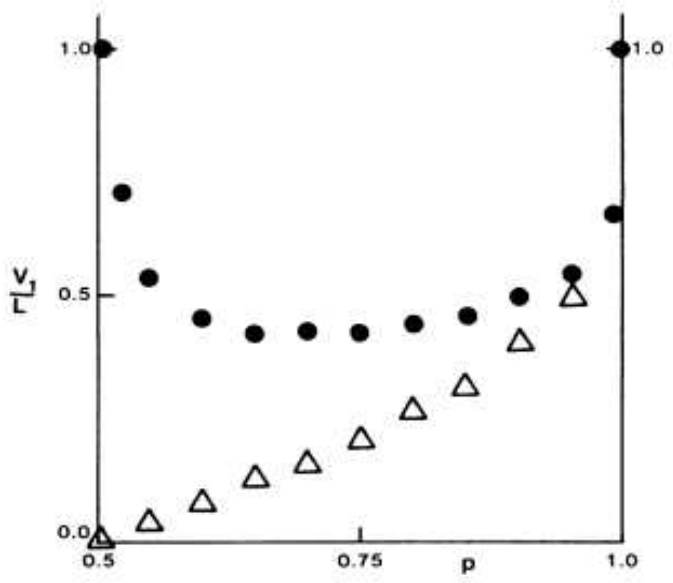


Figure 36. The scaling of both conductivity and strength in $2d$ RFM as a function of the bond probability $p$ (from Ref. [316]).

exponential or Gumbel-form, of extremal statistics [318]. One can write for the integrated distribution

$$P(i) = 1 - \exp\left(-cL^d \exp\left[-ki_b^{-1/\alpha}\right]\right), \tag{86}$$

where $\alpha$ is a constant that depends on $p$ (recall again this is for percolative disorder), as are $c$ and $k$. For the average strength it follows that there is a logarithmic size-effect, $\langle \sigma_c(L) \rangle \sim 1/\log L^a$ where $a \sim \mathcal{O}(1)$ and is difficult to establish rigorously.

**5.4.4** ***Crack fronts and gradient percolation.*** An interesting variation of the percolation problem is *gradient percolation* in which the symmetry is broken by letting the occupation probability of bonds to be a function of the vertical coordinate $y$ so that $p \equiv p(y)$ [319]. In the simplest case, $p(y)$ is a linearly decreasing function interpolating between $p = 1$ and $p = 0$, but other choices do not change the basic physics. This model has applications in several mean-field -like fracture models in which the gradient is imposed into damage by an external displacement or potential field [298–300].

The essential feature of gradient percolation is that an occupied region is

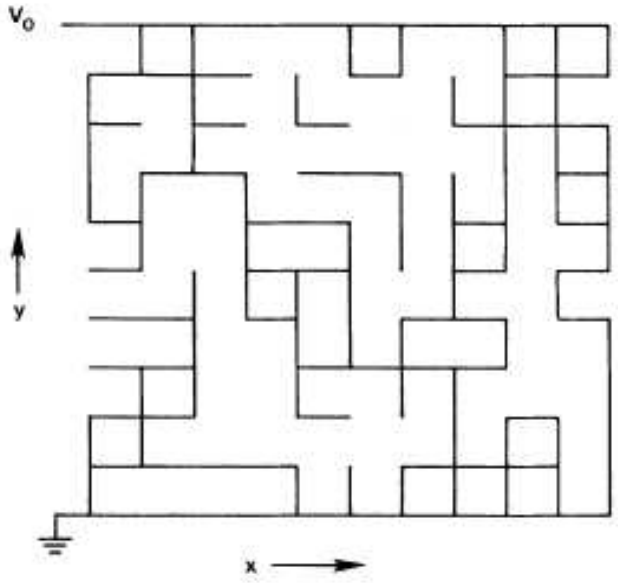


Figure 37. Example of a $2d$ fuse network for $p = 0.75$. What is the largest linear defect in such a system?

separated from an empty region by a corrugated front. The front occurs around the region where $p(x) \sim p_c$ and displays a self-similar geometry at short scales, crossing over to a flat profile at larger scale. The crossover scale $\xi_c$ is set by the value of concentration gradient $\nabla p$ around $p_c$. Using scaling arguments it is possible to show that

$$\xi_c \sim (\nabla p)^{-\alpha} \qquad \alpha = \frac{\nu}{\nu + 1}, \tag{87}$$

where $\nu$ is the correlation-length critical exponent of percolation defined in Eq. (84). The width of the separation front scales linearly with $\xi_c$ and thus increases as the gradient becomes weaker. For lengthscales smaller than $\xi_c$ the front is essentially equivalent to the perimeter of a percolation cluster and has thus a fractal dimension $D = 4/3$ (or $D = 7/4$ depending on the definition of the front) [320]. An example of a gradient percolation cluster is reported in Fig. 38.

The relation between gradient percolation and fracture is based on the study of models of planar cracks. An approach alternative to the crack line depinning scenario discussed in Sec. 5.3 considers damage accumulation in a stress gradient. Thus the crack is not considered as line, but as the separation front between damaged and intact areas, allowing for microcrack formation and co-

alescence even ahead of the main crack. The question is whether this effect can account for the discrepancy between the experiments and the crack depinning predictions.

Different types of lattice models have thus been simulated with boundary conditions inducing a stress gradient. Simulations of a two dimensional RFM in the planar crack geometry (i.e. considering two conducting plates connected by fuses) yield a gradient percolation front [298]. A beam model studied in a similar geometry, recovers instead the crack line depinning exponents, indicating that damage nucleation is irrelevant for crack roughness in that model [299]. On the other hand, a long-range scalar model, simulating planar cracks in a three dimensional geometry, yields a larger exponent $\zeta \simeq 0.6$ which could explain the experiments [300, 321]. The validity of this result is questionable based on the reasoning given below [322].

In the model of Refs. [300, 321], the width of the front $W$ increases with the external load approximately as a power law, and eventually saturates. As in gradient percolation, the saturated width $W^*$ scales with the gradient of the damage profile (see Eq. (87)). Since in Ref. [300] $\xi \sim L$, where $L_x$ is the lattice size parallel to the front, one can combine the initial dynamic scaling with the saturated width into a "Family-Vicsek"-like scaling form $W(L_x, t) = L^\alpha f(t/L^z)$, and conclude that the fronts are self-affine interfaces with $\zeta = \alpha$. In gradient percolation, however, $\alpha$ can *not* be interpreted as a roughness exponent, since as we discussed above the front is *self-similar* [322]. If we remove the overhangs from the front through a solid-on-solid projection, we obtain a single valued interface $h(x)$ that can be analyzed using conventional methods. The result, shown in Fig. 39 is an artificial multiscaling for the correlation functions

$$\langle |h(x + x') - h(x')|^q \rangle^{1/q} \sim x^{\zeta_q}, \tag{88}$$

where $\zeta_q = 1$ for $q \leq 1$ and $\zeta_q = 1/q$ for $q > 1$ The multiscaling behavior is easily understandable: for $q < 1$ the scaling is sensitive to the fractal, hence $\zeta_q = 1$ as expected for isotropic scaling. For $q > 1$ the scaling is dominated by the big jumps, which are also apparent in Fig. 38 [323].

In summary, if the front is due to a gradient percolation mechanism then its geometry is not self-affine, even when the gradient scales with $L$ as in some fracture models [321]. The same reasoning applies to the theoretical arguments put forward in Ref. [324] to explain the roughness of the cracks in the random fuse models. The scaling theory of Ref. [324] rests on a number of assumptions:

(i) in the limit of strong disorder fracture occurs at a percolation (possibly correlated) critical point;
(ii) for weak disorder crack localization occurs, producing a quadratic damage

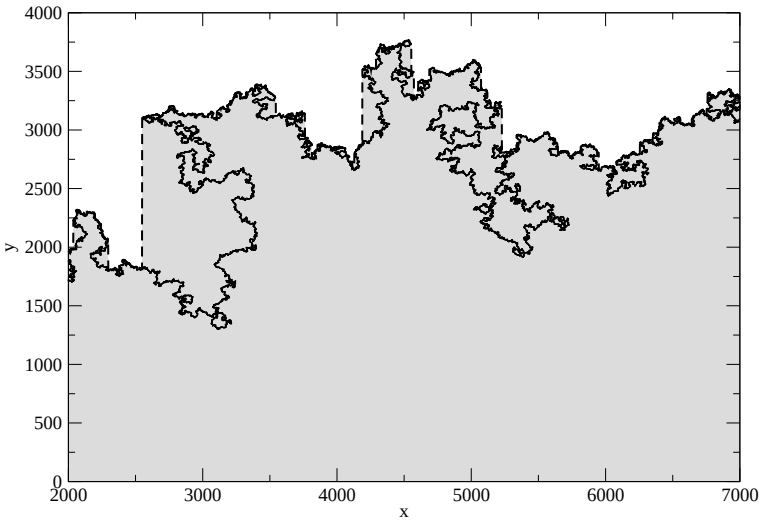


Figure 38. A fractal front in gradient percolation. We also display the solid-on-solid projection of the front which is single valued but not self-affine. Courtesy of A. Baldassarri, see also [323].

profile;

(iii) the width of the damage profile is a linear function of the lattice size; and
(iv) weak and strong disorder are characterized by the same $\nu$ exponent.

Given these assumptions, the authors of Ref. [324] argue that in the localization regime the crack is formed as a front in gradient percolation, leading to a scaling relation $\alpha = 2\nu/(1+2\nu)$, where the factor 2 (not present in Eq. (87)) comes from assumptions 2 and 3. As discussed above, the identification of $\alpha$ with $\zeta$ is incorrect. In addition, the analysis of large scale numerical simulations yields a series of additional problems: (i) the existence of a reliable percolation scaling is dubious; (ii) the damage profile is not quadratic; (iii) the width of the damage profile is not a linear function of $L$ [325].

## 6 Numerical simulations

Here we review the main results, obtained from numerical simulations of statistical models for fracture for the kind of models discussed in Section 4. We present a detailed discussion of the algorithms employed for such simulations in the appendix. The main work horse for these studies has traditionally been the RFM, which therefore will garner the most attention in what follows. The main motif of this section is to summarize the phenomenology of the results, from the RFM and similar models, and to emphasize the relationship

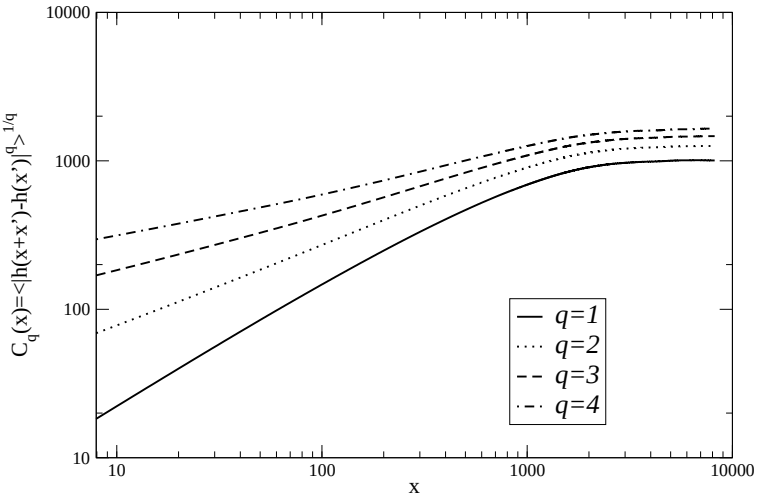


Figure 39. The high order correlation function for the solid-on-solid projection of a gradient percolation front. Since the original front is self-similar, the projection displays an artificial multi-affinity with effective exponents $\zeta_q = 1/q$ for $q > 1$. Courtesy of A. Baldassarri, see also [323].

with the fracture mechanics framework outlined in Sec. 2 and the theoretical approaches reported in Sec. 5. For simplicity we defer a general comparison between simulations and experiments discussed in Sec. 3 to the conclusions.

We first discuss the scaling of the stress-strain characteristics (Sec. 6.1) , and its interpretation in terms of damage mechanics (Sec. 6.2). One issue is whether the numerical data can be interpreted in terms of a scaling picture or framework from statistical physics. Damage as a thermodynamic quantity is then further explored analyzing the spatial distributions of local damage, the development of localization and internal correlations. The two central questions here concern the nature of the approach to peak load, what damage can tell about it, and the role of disorder in the process.

Next, we discuss the topics that are more relevant for statistical experiments: fracture strength, crack morphology and avalanche precursors. In particular

(i) We analyze the properties of the strength distribution and the associated size effects, including a discussion of the effect of disorder in notched specimens. Such results are of importance due to the relation to weakest-link theory and due to the engineering applications (Sec. 6.3).

(ii) The surface properties of cracks are considered from the viewpoint of establishing the true scaling indicated by the data: what is the minimal set of exponents that suffices, and what is the role of disorder and dimensionality (Sec. 6.4).

(iii) The avalanches in fracture models are discussed based on general scaling relations for systems with crackling noise. Again, it is important to understand

how the specific scenario (i.e., type of interactions, disorder, dimensionality) influence the avalanche behavior (Sec. 6.5).

### 6.1 *The I-V characteristics and the damage variable*

The first basic information that can be obtained from numerical simulation is the constitutive response of the model, in the form of a stress-strain curve for tensorial models or, more simply, of a current-voltage ($I-V$) curve for the RFM. This quantity is particularly important in connection with damage mechanics (see Sec. 2.5), since lattice models allow to test possible relations between the microscopic damage state and the macroscopic constitutive behavior. Here for the sake of clarity we focus on the scalar case (i.e. the RFM) where the damage variable $D$ is simply defined. The same discussion can be translated to generic (tensorial) fracture models considering the stress strain characteristics. These models have in general the important feature, that they allow in contrast to mean-field -like approaches the existence of damage correlations, which can thus be explored.

Figure 40 presents a typical $I-V$ response, from a 2D RFM (triangular lattice), with a system size $L = 64$. One can see damage accumulation, and then signatures of crack growth which becomes unstable after the peak current. While initially the stress concentrations are masked by the disorder, in the last stage one of the microcracks wins over the others and dominates.

To obtain a faithful representation of the macroscopic response one needs to perform an ensemble average over many sample configurations. This can naturally be done fixing three different control parameters: current, voltage, or accumulated damage (i.e. number of broken bonds). Appropriate rescaling of the curves is then necessary to obtain intensive quantities (i.e. independent of the system size). For this reason the voltage $V$ is the most natural parameter, since the current excludes the post-peak load part of the $I-V$ response, and the damage is - as is discussed below - not an intensive variable, at least in the post peak regime.

An old idea, inspired from self-affine interface growth, was to attempt a Family-Vicsek (FV) [326] scaling for the $I-V$ curve (see also Ref. [327]). This entails the scaling form

$$I = L^{\Omega_1}\phi(\frac{V}{L^{\Omega_2}}). \tag{89}$$

The scaling function $\phi(x)$ has to fulfill the condition that for small $V$ the response is independent of system size. There is an important detail, not fully appreciated in the literature: usually in the context of surface growth the use of Eq. (89) implies that $\phi \to const > 0$ for $x \gg 1$. In fracture, however,

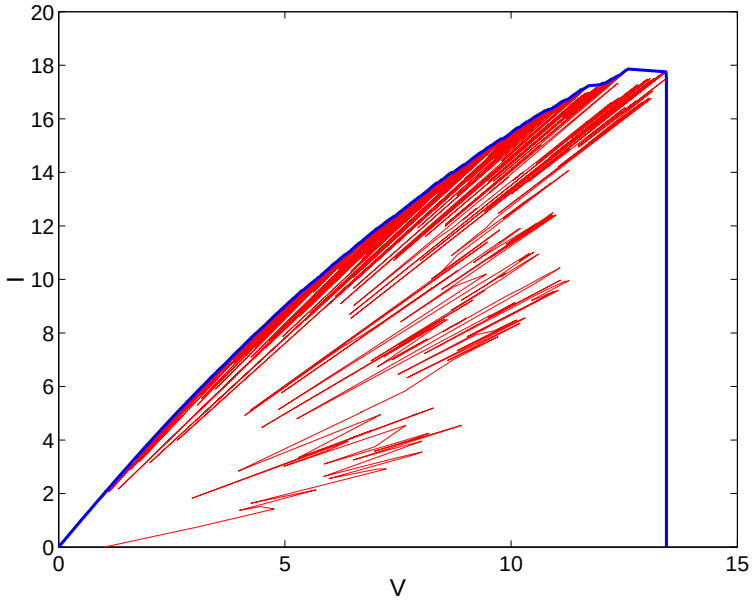


Figure 40. Typical $I-V$ response of a 2D RFM triangular lattice system of size $L=64$. The thin line is the evolution that follows a quasistatic dynamics in which bonds are broken one at a time. The envelope of the $I-V$ response (thick line) represents the voltage controlled response.

the current becomes zero for large enough $V$: in that limit $\phi$ vanishes and is thus not monotonic. For small $x$ the function has to scale as power-law of its argument, which directly implies that the FV collapse *is not applicable* unless the peak load has a power-law scaling form ($I_{max} \sim L^y$, for some $y$), and the same holds also for the corresponding voltage. In addition, the scaling of $\phi$ couples the exponents $\Omega_1$ and $\Omega_2$: since for small $V$, $I \propto V$, it follows that $\phi \sim x$ and $\Omega_1 = \Omega_2$. While this discussion is valid in general, for arbitrary models and experiments, we consider as an example the numerical data for the RFM.

Figure 41(a) presents the scaling of $I-V$ response based on the FV scaling. The plots in Fig. 41(a) correspond to $\Omega_1 = \Omega_2 = 0.75$ as proposed in Ref. [326]. On the other hand, an alternative ad-hoc scaling form

$$I = \frac{L^{\Omega_1}}{(logL)^{\psi}} \phi_2 (\frac{V}{L^{\Omega_1}}) \tag{90}$$

has been proposed by Sahimi and collaborators, in Refs. [328,329]. The values indicated are $\Omega_1 \simeq 1 \pm 0.1$ and $\psi \simeq 0.1$. Figure 41(b) presents the corresponding scaling of $I-V$ curves based on Eq. (90). This suggests that scaling form based on Eq. (90) is de facto more appropriate than the FV one, but of course one notes that the scaling is far from perfect. The logarithmic factor in Eq. (90)

arises from an attempt to correctly take into account the strength size effect. For such a scaling to hold the scaling function $\phi_2$ would also need to contain logarithmic terms so that the small-voltage limit is independent of $L$. Their origin would be unknown. Notice that the analysis presented here is also valid for experiments, and for instance questions the application of FV scaling to the experiment of Otomar et al. [177].

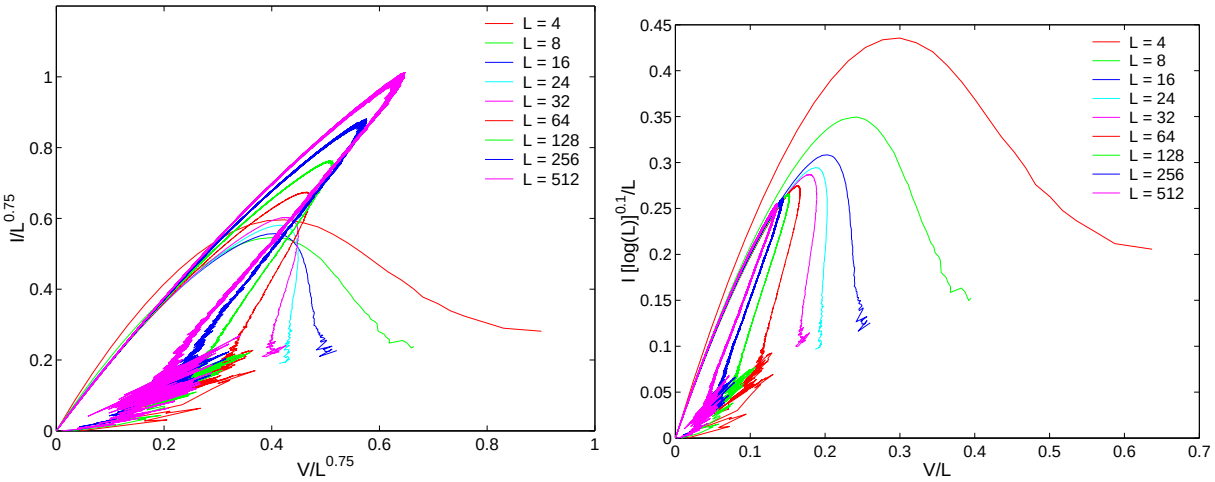


Figure 41. Scaling of $I-V$ response for different triangular lattice system sizes of 2D RFM. (a) Family-Vicsek scaling as proposed in Ref. [326] (see Eq. (89)) with $\Omega_1 = \Omega_2 = 0.75$. (b) Scaling form proposed in Refs. [328, 329] (see Eq. (90) with $\Omega_1 = 1.0$ and $\psi = 0.1$).

Notice that for the data in Figs. 41 ensemble averaging is performed using the accumulated damage as a control parameter as originally done in Refs. [326, 328–330]. This produces an unphysical hysteresis in the curves, which corresponds to unstable crack growth in voltage or current controlled cases. This effect was not apparent for the small lattices sizes at hand in Refs. [326, 328–330], but becomes clear for larger lattices employed here. To avoid this problem, it is more natural to average the envelopes of the $I-V$ curves, using the voltage as a control parameter. The total current $I$ flowing through the lattice in the RFM is given by $I = \Sigma\ V$ where $\Sigma$ is the total conductance of the lattice system expressed as

$$\Sigma = \frac{\left[\sum_{ij} \sigma_{ij}\ V_{ij}^2\right]}{V^2}, \tag{91}$$

and $\sigma_{ij}$ is the local conductivity of the fuse between nodes $i$ and $j$. A simple

normalized form of the $I-V$ curve may then be obtained as

$$\frac{IL}{N_{el}} = \frac{\left[\sum_{ij} \sigma_{ij}\ s_{ij}^2\right]}{N_{el}}\ \frac{V}{L}, \tag{92}$$

where $s_{ij}$ denotes the enhancement of current (stress concentration factor) due to fuse burnouts and $\frac{V}{L}$ is voltage drop per unit length. It should be noted that $s_{ij}=0$ for all the *dangling* or *dead ends* (using percolation theory language) that do not carry any current (stress) even though they are not broken.

Figure 42 presents the ensemble averaged $I-V$ response normalized as in Eq. (92), showing a perfect collapse up to peak load, with strong deviations thereafter. One can easily extract from this curve the behavior of the damage variable $D(V) \equiv 1-\Sigma/\Sigma_0$, where $\Sigma_0$ is the conductivity of the intact lattice. Figure 43 shows that damage variable $D(V)$ grows linearly and remains an intensive variable up to the peak load, beyond which size dependent effects become apparent. Similar damage variable definitions are often used in the engineering literature [25]. It is clear that they are suitable to represent the extent of damage only within the early stages of damage evolution, where the damage levels are moderate and the damage is not localized, but become clearly inadequate around the peak load and especially in the softening regime of the stress-strain curve. In these regimes, $D$ is strongly size-dependent and hence cannot be considered as a thermodynamics based *intensive damage state variable*. Of course, one should keep in mind that due to the "size-effect" asymptotically $I_{max}(L)$ may go to zero anyway, which implies that $D(V)$ would not exist in a well-defined sense for any particular value of $V$.

In order to better understand the behavior of the damage variable, it is instructive to observe the degradation of the conductivity of a single sample as a function of the fraction of broken bonds $p_b$. As is apparent looking at Fig. 44, the conductivity before the peak load follows nicely the prediction of effective-medium theory, considering the contribution to $p_b$ coming both from broken and dangling bonds. This means that there are no strong sample-to-sample variations (nor as we discuss below a strong $L$-dependence). The agreement with the conjecture implies that damage is spread on large scales homogeneously in the sample with no localization or strong correlations. Hence the definition of a RVE is possible and a continuum damage description is appropriate. The lack of a "critical scenario" with a divergent correlation length $\xi$ in any case implies that the scalar damage variable $D$ could be simply written as a power series in the control parameter $V$, $D = d_0 V + d_1 V^2 \ldots$, with $I = (1-D(V))\Sigma_0 V$. Then, the study of damage becomes that of the coefficients $d_i$ and their dependence on model, dimensionality, and disorder.

In the post peak regime, however, the conductivity deviates abruptly from

the effective medium prediction, with strong sample-to-sample and lattice size dependent fluctuations. This brings back the question of ensemble averaging: by averaging together several curves as the one reported in Fig. 44, the abrupt character of the discontinuity is partly lost and one obtains smooth curves as the ones reported in Fig. 45(a). This effect becomes less and less important as the sample size is increased, but has lead to some confusion in the early literature, when only small samples were available. Alternatively, the averaging of the conductivity degradation responses may be performed by first shifting the data by the respective peak load locations $(p_p, \Sigma(p_p))$. In this way, one preserves the main character of the curves as shown in Fig. 45(b).

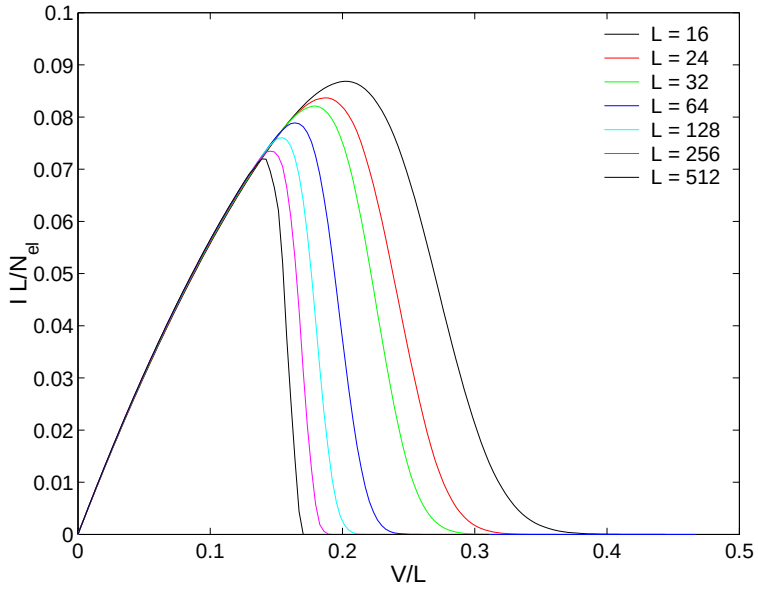


Figure 42. Normalized ensemble averaged $I - V$ response based on Eq. (92) for different 2D RFM triangular lattice systems of sizes $L = \{4, 8, 16, 24, 32, 64, 128, 256, 512\}$.

### 6.2 *Damage Distribution*

Fuse networks can be used to study the microscopic dynamics of damage. In the Sec. 6.1 we discussed the macroscopic characteristics of the RFM in terms of the I-V curves. The increase in the damage variable $D$ (in $I = (1-D(V))\Sigma_0 V)$) is concomitant to the growth of correlations due to microcracking controlled by the distribution of quenched disorder. When the disorder is narrowly distributed (weak disorder), it is known that damage is localized and the network breaks down without significant precursors [165]. For infinitely strong disorder,

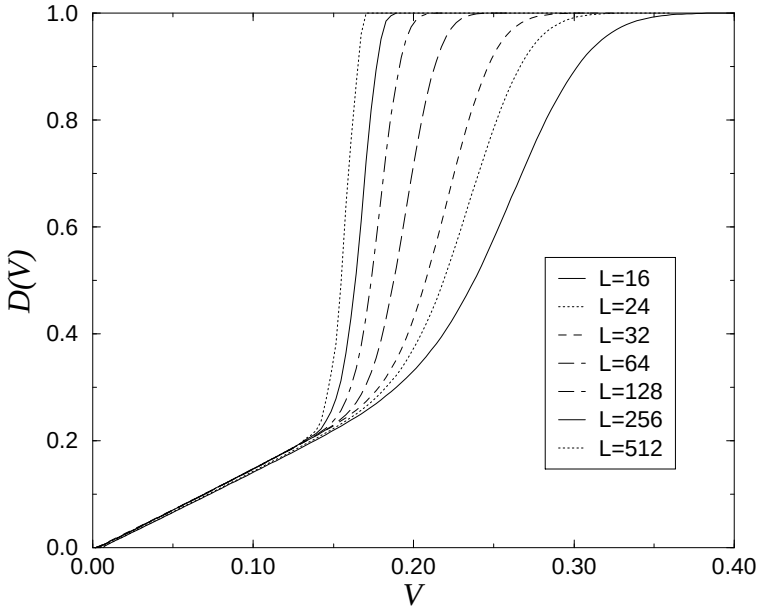


Figure 43. Ensemble averaged damage variable $D(V)$ for different 2D RFM triangular lattice systems of sizes $L = \{4, 8, 16, 24, 32, 64, 128, 256, 512\}$. After peak load the damage variable is not intensive. Also, the nonlinearity in the plots of $D(V)$ close to 1.0 is an artifact of $I - V$ averaging close to fracture.

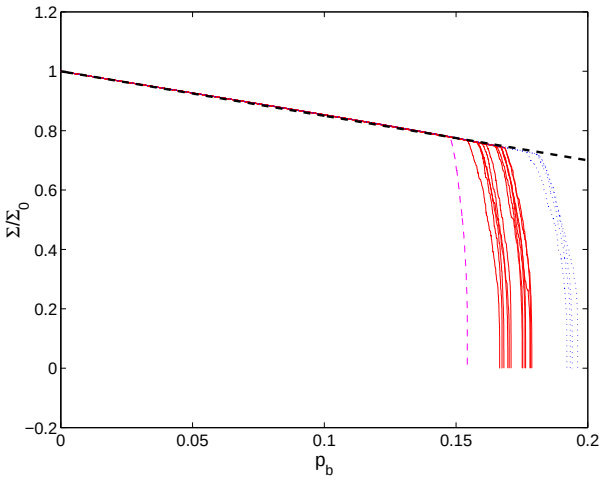


Figure 44. Typical conductivity (stiffness) degradation in various 2D RFM samples: triangular lattices of sizes $L = 256$ (dotted), 512 (solid), 1024 (thin dashed). The thick dashed line corresponds to the degradation of the conductivity predicted by effective medium theory.

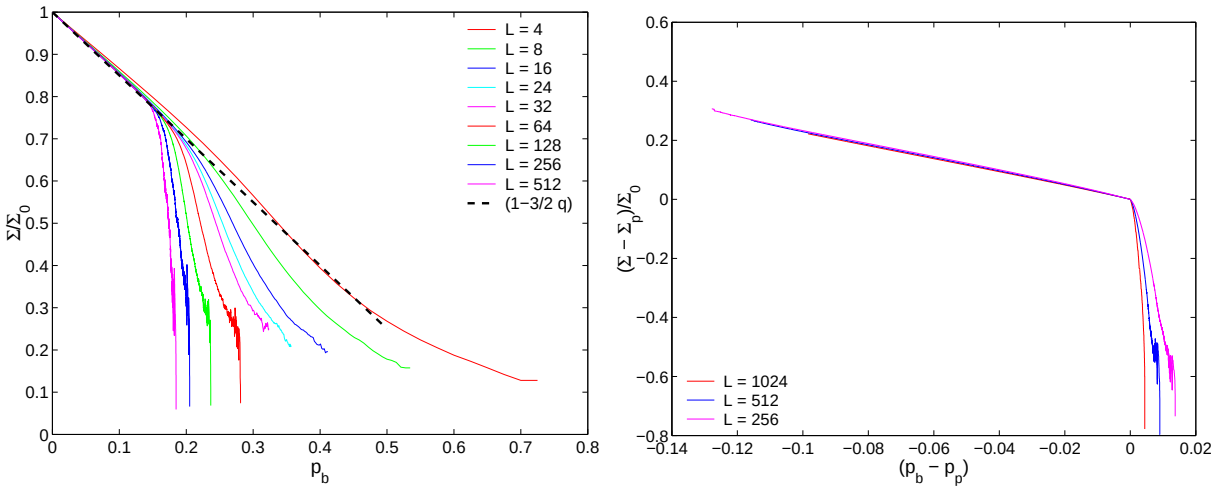


Figure 45. Average conductivity scaling in a 2D RFM triangular lattice system. (a) Averaging performed at constant $n_b$ number of broken bonds. (b) Averaging by first shifting each of the sample responses by their respective peak load positions.

the damage accumulation process can exactly be mapped onto an uncorrelated percolation problem [314]. The interesting situations are to be found for strong but finite disorder, where a substantial amount of damage is accumulated prior to failure. In these conditions, one can try to study several quantities such as the scaling of damage at maximum current, or the geometric characteristics of the ensembles of broken fuses along $I-V$ curves. One interesting question is in addition related to the fluctuations of damage at the $I-V$ curve maximum.

Figure 46 presents the snapshots of damage evolution in a typical 2D RFM simulation of size $L = 512$ and uniform disorder distribution in $[0, 1]$. From this figure, at least visually, it is apparent that damage evolves in a fashion that does not foretell the final crack up to the peak load (see Fig. 46e), beyond which the localization of damage occurs. Next we discuss various results concerning the distributions and fluctuations of damage, both at peak load and at final failure.

**6.2.1** ***Scaling of Damage Density.*** We first consider the evolution of the number of broken bonds at peak load, $n_p$, which excludes the bonds broken in the last catastrophic event, and the number of broken bonds at failure, $n_f$. The quantity $n_p$ is of interest since it tells how the damage is distributed before failure occurs. If the damage were to be localized along a single row, the number of broken bonds at peak load and failure would be $O(1)$ and $O(L)$, respectively, whereas screened percolation would result in $n_f \sim N_{el}$, where $N_{el}$ is the total number of bonds in the intact lattice.

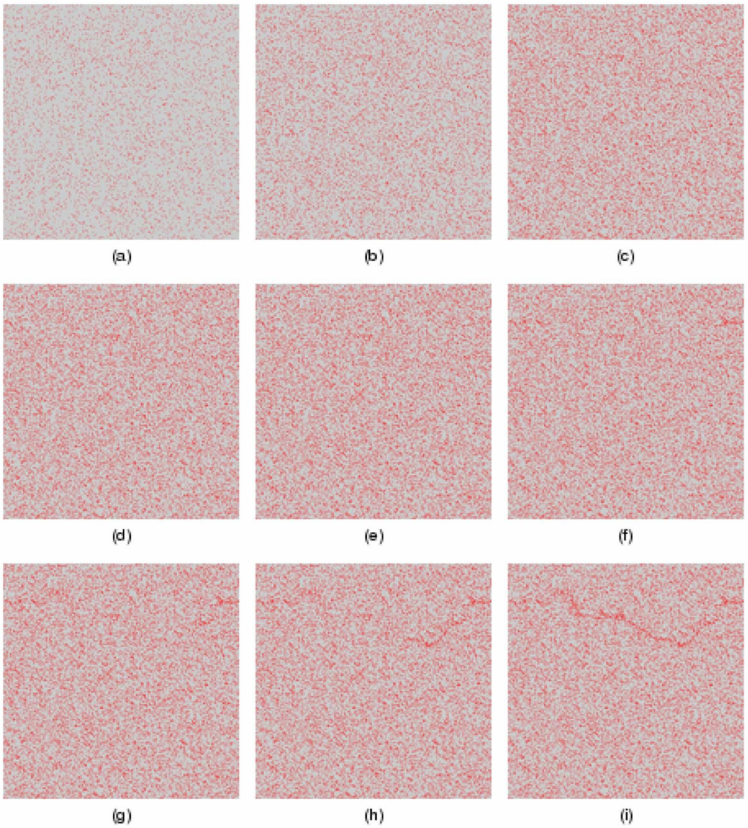


Figure 46. Snapshots of damage in a typical 2D triangular lattice system of size $L = 512$. Number of broken bonds at the peak load and at failure are 83995 and 89100, respectively. (a)-(i) represent the snapshots of damage after breaking $n_b$ number of bonds. (a) $n_b = 25000$ (b) $n_b = 50000$ (c) $n_b = 75000$ (d) $n_b = 80000$ (e) $n_b = 83995$ (peak load) (f) $n_b = 86000$ (g) $n_b = 87000$ (h) $n_b = 88000$ (i) $n_b = 89100$ (failure)

Figure 47 presents $n_p$ as a function of the lattice size $N_{el}$ for 2D RFM and for 2D RSM with uniform threshold disorder. The data displays a reasonable power law behavior $n_p \sim N_{el}^b$, with $b = 0.91 - 0.93$ [182, 325, 326, 331, 332]. In other words, the damage is sub-extensive reflecting a size-effect at the peak load that decreases with $N_{el}$. The difference between the RFM and RSM models is marginal. Some systematic deviations from the scaling form $n_p \sim N_{el}^b$ can perhaps be seen by plotting $n_p/N_{el}^b$ vs $N_{el}$ (see Ref. [325]). Such attempts would indicate that the damage data be equally well fit by a linear law times a logarithmic correction $n_p \simeq N_{el}/\log(N_{el})$ as suggested in Ref. [333]. This also implies that in the thermodynamic limit the peak load damage vanishes. For strong disorder (power law distributed with $\Delta = 20$, see Sec. 4.1) the data depicted in Fig. 47 implies a volume-like $b \simeq 1$, indicating behavior similar to the percolation limit in the range of $L$ used. The three dimensional results for

the RFM are similar [334, 335], with $n_p \sim N_{el}^b$ and $b = 0.72$ for weak disorder (a uniform distribution in $[1/2, 3/2]$ [335]) and $b = 0.99$ for stronger disorder (a uniform distribution in $[0, 1]$ [334]). The weak disorder scaling can also be recast as $n_p \simeq L^2$ corresponding to a localization along a plane.

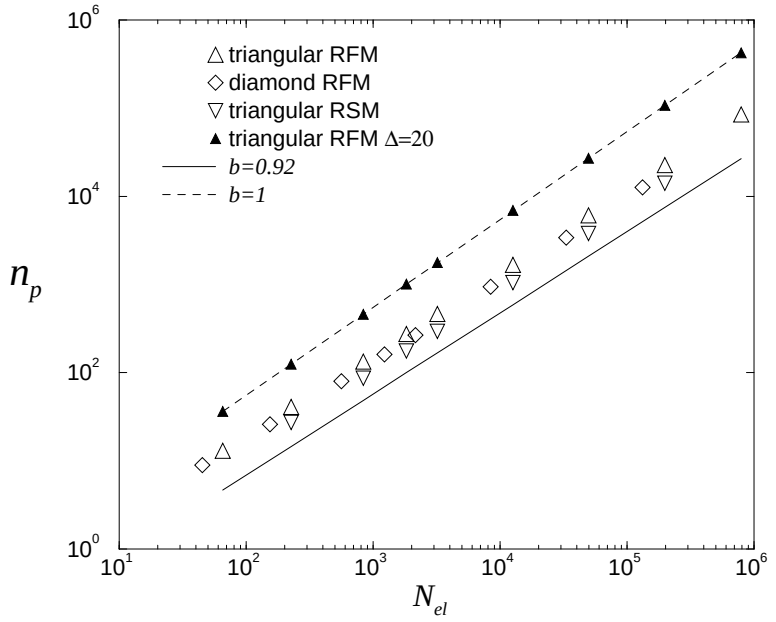


Figure 47. Scaling of number of broken bonds at peak load for two-dimensional triangular and diamond random fuse lattices, and triangular spring lattices. In all these models disorder is uniformly distributed in $[0, 1]$ and the scaling exponents are very close to each other. The last curve represents data obtained using a power low disorder distribution: the exponent changes to $b = 1$.

The other interesting quantity is the average number of broken bonds in the post-peak regime, $(n_f - n_p)$. This corresponds to the size of the last catastrophic avalanche, which is trivially so in particular in the current-driven case. It also exhibits a power law scaling $N_{el}^\theta$ with $\theta = 0.72$ in 2D RFM triangular lattices and $\theta = 0.69$ in 2D RFM diamond lattices [325], while $\theta = 0.68$ in 2D RSM triangular lattices [182], and $\theta = 0.81$ in 3D RFM cubic lattices [334]. If instead one uses again the $\Delta = 20$ case depicted above, the scaling with $N_{el}$ seems to be linear ($\theta = 1$), i.e., extensive similar to $n_p$ [325] whereas for weaker disorder one has $\theta < b$.

If $n_f$ scales extensively, one may then ask what is the finite-size correction to an asymptotic density defined as $p_c = \lim_{L\to\infty} n_f/N_{el}$, in analogy to percolation as argued by Hansen and co-workers [324, 336]. A percolation-like scaling

for the finite-$L$ fraction of broken bonds would be given by

$$p_f - p_c \sim L^{-\frac{1}{\nu}} \sim N_{el}^{-\frac{1}{2\nu}} \tag{93}$$

Here, $p_f = \frac{n_f}{N_{el}}$, and $\nu$ would define an exponent similar to that of the correlation length exponent in percolation. While small system size simulations could be consistent with Eq. (93), Ref. [325] shows that percolation scaling can be excluded and there is no hidden divergent lengthscale defining an exponent $\nu$. This is in agreement with the first-order, nucleation picture of fracture that one gains from mean-field -like models (Sec. 5.1). A similar conclusion is corroborated by considering other measures related to a characteristic lengthscale (which may be called a correlation length or a "RVE size", as discussed in Sec. 2) [331, 333].

To study further the question of damage fluctuations at peak load and failure we next consider the distributions ensemble averaged over samples. The cumulative probability distribution for the damage density at the peak load is defined as the probability $\Pi_p(p_b, L)$ that a system of size $L$ reaches peak load when the fraction of broken bonds equals $p_b = \frac{n_b}{N_{el}}$, where $n_b$ is the number of broken bonds. Scaling such distributions using the average and standard deviation one obtains a good collapse of the distributions (Fig. 48) for both random fuse and random spring models in $d = 2$ and it seems that this behavior is independent of lattice structure and disorder [325]. Similar results are found in three dimensions.

The cumulative probability distribution for the damage density at failure is defined similarly, $\Pi_f(p_b, L)$ [325], and there seems to be no essential difference between the scaled forms of $\Pi_f$ and $\Pi_p$. This is in contrast with some claims in the literature wherein a percolation scaling $\Pi_f(p_b, L) = \Pi((p_b - p_c)L^{1/\nu})$ was suggested for $\Pi_f(p_b, L)$, and the width of the distribution is assumed to originate from a correlation length-like scaling [324]. In the random fuse model, the scaling forms of cumulative distributions of damage density at peak load and failure seem to follow the same scaling function, $\Pi(\bar{p}) = \Pi_f(\bar{p}_f) = \Pi_p(\bar{p}_p)$ [325]. This does not seem to hold for spring lattice systems [182], possibly due to the non-local character of the loss of rigidity in central-force models (Sec. 4.2). We note finally, that the scaling functions display Gaussian forms in the case of the RFM (see the inset of Fig. 48 and Ref. [182] for the peak load of 2D RSM). The Gaussian distribution is consistent with the absence of a divergent correlation length at failure [331, 333], which can be understood by observing that the damage density $p_f$ is the sum of local random variables (the local damage, $s_i$), each originating from the contribution of a single RVE. The central limit theorem yields then a Gaussian distribution, only if correlations in the field $s_i$ are short-ranged as is the case if a RVE can be defined.

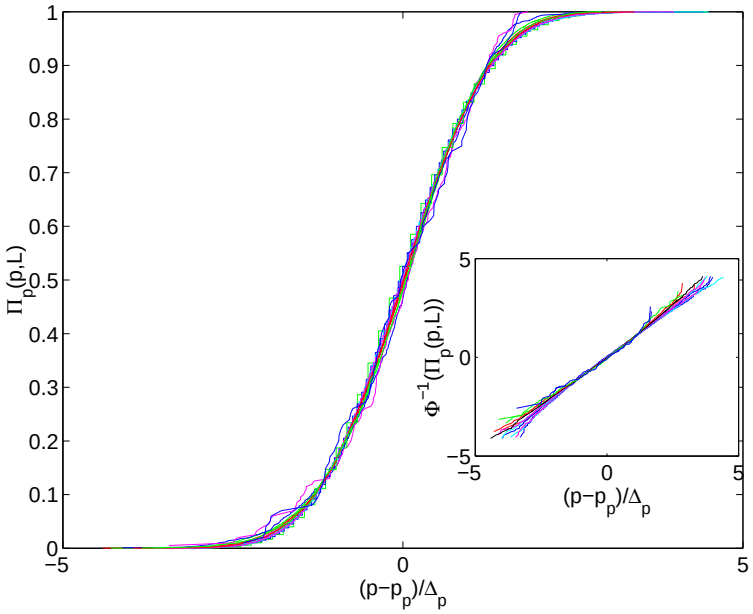


Figure 48. Comparison between the cumulative probability distributions of the fraction of broken bonds at the peak load is presented for the RSM and RFM. For the RSM, triangular lattices of sizes ($L = 8, 16, 24, 32, 64, 128, 256$), and for the RFM, triangular lattices of sizes ($L = 16, 24, 32, 64, 128, 256, 512$) are plotted. The normal distribution fit in the re-parameterized form is presented in the inset. In the RFM case, collapse of cumulative probability distributions at the peak load for different lattice topologies (triangular and diamond) and different disorder distributions (uniform and power law) is presented in Ref. [325].

**6.2.2** ***Damage Localization.*** The question of how damage localizes in lattice models is a problem with many facets. An important question is how the damage variable $D$ is connected to $n_b/N_{el}$ and to the effective RVE size. One has to separate here two issues, the first of which is the development of a macroscopic damage profile in a sample, and the second being how local microfailures become correlated. The first issue can be resolved by evaluating the disorder averaged damage profiles from simulations. However, a posteriori analysis of damage profiles is tricky since the final crack position fluctuates, i.e, it can occur anywhere along the loading direction of the lattice system, and the fact that the final crack position is in general surrounded by a damage "cloud". To overcome this problem, one can use different techniques to determine the location of the "crack" along the macroscopic current flow direction. Some of these techniques are based on shifting individual damage profiles by the center of mass of the damage, or averaging the power spectrum (square of magnitude of the Fourier transforms) of individual damage profiles [325].

Figure 49 presents the average damage profiles for the damage accumulated up to the peak load by first shifting the damage profiles by the center of

mass of the damage and then averaging over different samples. This result, displayed in Fig. 49 for 2D RFM model with uniform disorder distribution, clearly shows that there is no localization at peak load. Similar behavior has been observed in various other cases; namely, the 2D RFM simulations with power law threshold distribution ($\Delta = 20$) [325], the 2D RSM simulations with uniform thresholds distribution [182], and 3D RFM simulations with uniform thresholds distribution. For small system sizes, $L$, there are residual effects due to the non-periodicity of the lattice system in the loading direction. All in all, such profiles suffice to show that the localization profiles measured at failure in the literature [324, 333, 336, 337] are due to the damage accumulated between the peak load and failure. Thus, in the following, we consider the damage profiles $\Delta p(y)$ for the damage accumulated between the peak load and failure. Figure 50 presents a data collapse of the average profiles, using the form

$$\langle \Delta p(y, L) \rangle / \langle \Delta p(0) \rangle = f(|y - L/2|/\xi), \tag{94}$$

where the damage peak scales as $\langle \Delta p(0) \rangle = L^{-\chi}$, with $\chi = 0.3$ and the profile width scales as $\xi \sim L^{\alpha}$, with $\alpha = 0.8$ (see Fig. 50). Similar results are obtained for the 2D RSM [182] and 3D RFM [338] models: the profiles display exponential tails in both cases, with the exponents for the peak being $\chi = 0.37$ and $\chi = 0.15$ and for the profile width $\alpha = 0.65$ and $\alpha = 0.5$, respectively. The $\alpha$-exponents clearly have to do with the final crack roughness, which is discussed in Sec. 6.4. It is an open question as to how the dynamics in this catastrophic phase should be characterized, in order to explain the value of $\alpha$ (or possibly that of $\zeta$, conversely), and more work is needed in this respect. This would also call for studies with simplified models (Sec. 5.1).

One may also consider as a measure the "width of the damage cloud", which is defined as $W \equiv (\langle (y_b - \bar{y_b})^2 \rangle)^{1/2}$. Here $y_b$ is the $y$ coordinate of a broken bond and a disorder average is performed. At peak load, $W \sim L/\sqrt{(12)}$ for both 2D RFM and RSM lattice systems [182, 325, 338], consistent with uniformly distributed damage profiles at the peak load. In the post-peak regime, if the average is restricted only to the bonds broken in the last catastrophic failure, one has $W \sim L^{0.81}$ for 2D RFM [325], and $W \sim L^{0.7}$ for the 3D RFM. These non-trivial scaling exponents in the post-peak regime indicate that the damage profiles exhibit a localized behavior in the post-peak regime in agreement with the results presented above.

The presence of an abrupt localization can also be seen by considering the difference in the accumulated damage between the window containing the final crack (and damage) and any other arbitrary window. Let $n_l$ and $n_a$ denote the associated numbers of broken bonds. Figure 51 presents the evolution of $(n_l - n_a)$ with damage accumulation for 2D RFM lattice system of size

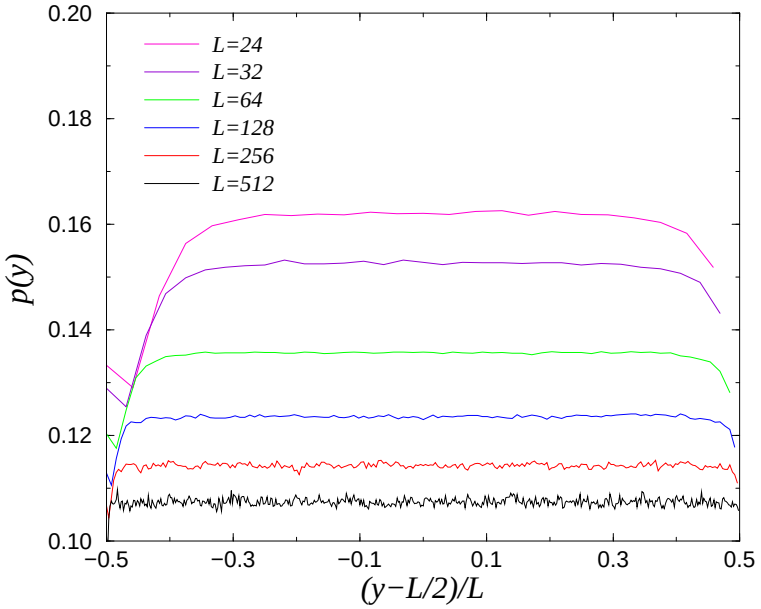


Figure 49. Average damage profiles at peak load obtained by first centering the data around the center of mass of the damage and then averaging over different samples. Data are for RFM simulations with uniform thresholds disorder.

$L = 512$, averaged over 200 samples. This result shows that $(n_l - n_a) \approx 0$ up to the peak load, and a steep increase in $(n_l - n_a)$ in the post-peak regime indicating abrupt localization.

**6.2.3** ***Crack clusters and damage correlations.*** An analysis of the clusters of connected broken bonds is the easiest way to consider the correlation properties of damage. This topic is also of interest due to the relation between the largest defect cluster and the fracture strength distributions discussed in Sec. 2.4 [9, 329, 339, 340]. In the RFM with strong disorder damage accumulation is non-trivial. One could postulate that the size-scaling and strength distribution correspond to the statistics of the largest crack present in the system at peak load, while crack represents the result of damage accumulation prior to the peak load.

The relevant questions are: (i) what kind of distribution is followed by the crack clusters in the strong disorder case just before the appearance of an unstable crack, and (ii) whether there exists a relationship between the distribution of maximum cluster size at peak load and the fracture strength distribution?

Figure 52 presents the connected cluster size distribution at the peak load in a 3D RFM for various $L$. The plots indicate that simple power-law and

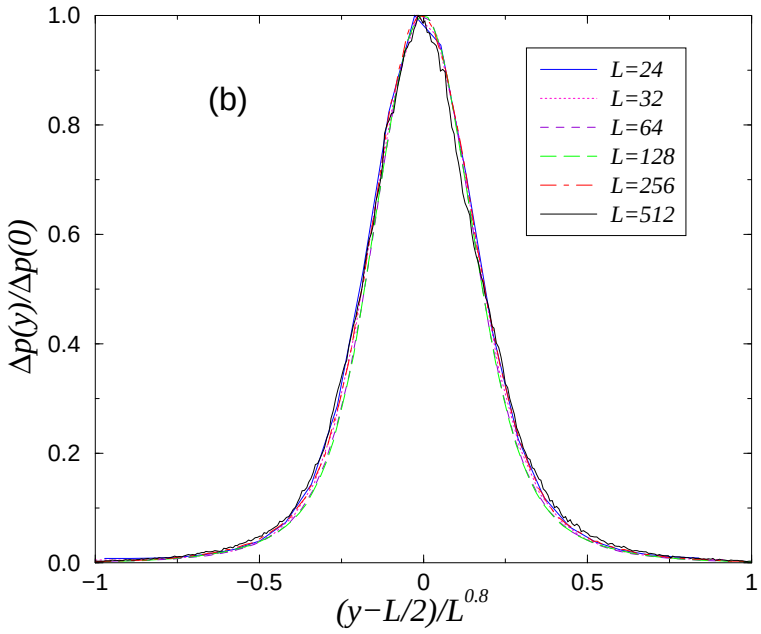


Figure 50. Data collapse of the localization profiles for the damage accumulated between peak load and failure. The profiles show exponential tails. Data are for RFM simulations with uniform thresholds disorder.

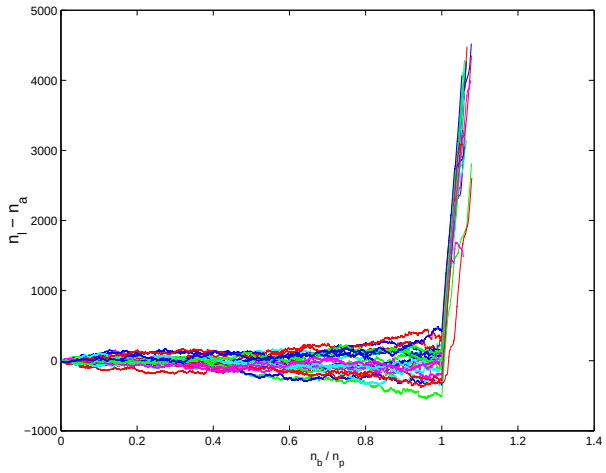


Figure 51. Localization of damage ($n_l - n_a$) in a 2D RFM simulation of lattice system size $L = 512$ averaged over 200 samples. Localization of damage occurs abruptly at the peak load ($n_b/n_p = 1$).

exponential representations are not adequate, and a similar result is obtained in 2D as well [341]. For completeness, one should note that the distribution of the *largest* crack cluster at the peak load seems to follow a Lognormal distribution as demonstrated in Fig. 53 for various system sizes. It is interesting to note that the fracture strength data presented in the following subsection indicate that a Lognormal distribution represents an adequate fit for the fracture strength distribution in broadly disordered materials. At first glance, this result appears to be trivial: assuming that the stress concentration around the largest crack cluster is given by a power law, the fracture strength follows a Lognormal distribution since the power of a Lognormal distribution is also a Lognormal distribution. However, as noted in Ref. [341], a close examination of the largest crack cluster size data at peak load and the fracture strength data reveals that the largest crack cluster size and the fracture strength are uncorrelated [341]. Indeed, quite often, the final spanning crack is formed not due to the propagation of the largest crack at the peak load, but instead due to coalescence of smaller cracks (see Figs. 6 and 7 of Ref. [341]).

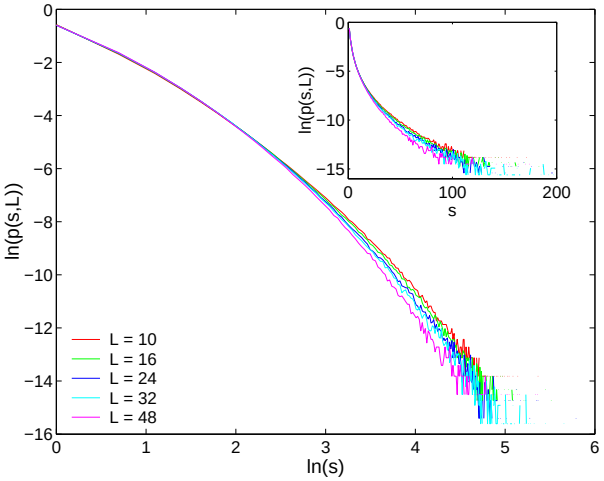


Figure 52. Damage cluster distribution at the peak load in cubic lattices of system sizes $L = \{10, 16, 24, 32, 48\}$ in log-log and log-linear scales (inset). The cluster distribution data for different lattice system sizes is neither a power-law or an exponential distribution.

As a further method to assess the presence of correlations, we consider the ensemble averaged response of entropy, which has also been used in experiments (see Fig. 24 in Sec. 3). The entropy is defined as

$$S = -\langle \sum_i q_i \; log(q_i) \rangle, \tag{95}$$

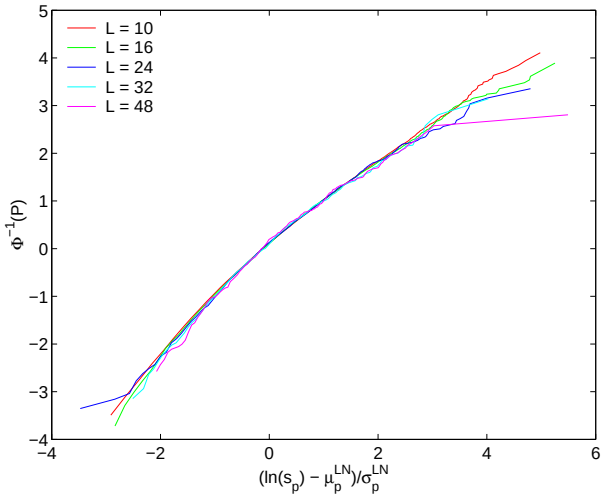


Figure 53. Re-parameterized form of Lognormal fit for the cumulative probability distribution of largest crack cluster size at the peak load in cubic lattices of system sizes $L = \{10, 16, 24, 32, 48\}$. $\mu_p^{LN}$ and $\sigma_p^{LN}$ refer to the mean and the standard deviation of the logarithm of largest cluster sizes, $s_p$, at peak load.

where $q_i$ is the fraction of broken bonds within the $i^{th}$ window (or section). The lattice system is divided into $i = 1, \ldots, m_{box}$ independent measurement windows.

A useful choice is to take the windows to be of width $\Delta y$, along the current flow direction [333]. We now present data for the load-displacement response of a typical RFM simulation, divided into 12 segments, with six equal segments each before and after the peak load. Let $D_I = 1, 2, \ldots, 12$ refer to each of these segments. The entropy $S$ of the damage cloud is calculated at the end of each of these $D_I$ stages using different section widths. For each system size $L$, we considered $N_{box}$ number of different section widths, where $N_{box} = \frac{log(L/8)}{log(2)} + 1$. Each of the different window sizes is denoted by a box size index $B_I = (0, 1, \cdots, N_{box} - 1)$, with the corresponding section widths $B_{size} = 2^{B_I}$. Thus, there are $m_{box} = \frac{L}{\Delta y}$ number of sections (boxes) over which $\sum_i$ is performed (i.e., $i = 1, \ldots, m_{box}$).

Fig. 54 presents the entropy $S$ versus $D_I$, calculated using different section widths for a uniform threshold distribution ($\Delta = 1$). For damage accumulation up to the peak load, the entropy increases and attains a maximum ($S_{max} \approx log(m_{box})$) corresponding to a completely random spatial damage distribution, followed at the peak load by a localization phase in which the entropy decreases. In the inset of Fig. 54 the entropy at the peak load versus the box size index $B_I$ is plotted for uniform and power law threshold distributions, for system sizes $L = (64, 128, 256, 512, 1024)$. The slope of the graph in

the inset equals $-log(2) = -0.693$, which matches exactly with the slope of the maximum entropy $S_{max}$ versus $B_I$ since $S_{max} = log(m_{box}) = log(L/B_{size}) = log(L/2^{B_I}) = log(L) - B_I log(2)$.

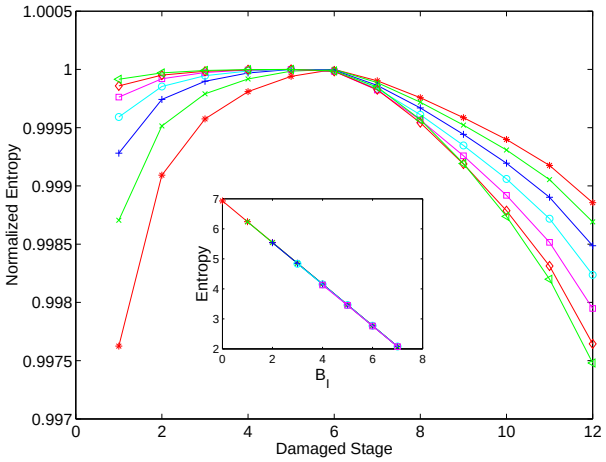


Figure 54. Entropy $S$ versus the damaged stage index $D_I$ for a triangular lattice of size $L = 512$ with uniform threshold distribution ($\Delta = 1$) threshold distribution. Symbols are $B_I = (0, 1, \cdots, N_{box} - 1) = (*, x, +, \circ, \square, \diamond, \triangleleft)$. The inset presents the entropy at the peak load versus the box size index for uniform and power law threshold distributions for $L = (64, 128, 256, 512, 1024)$. The data for smaller systems is shifted such that the points correspond to the same relative box size. The slope of the graph in the inset is equal to $-log(2) = -0.693$ corresponding to randomly distributed damage.

## 6.3 *Fracture strength*

**6.3.1** ***The fracture strength distribution.*** Before discussing the results of numerical simulations let us recall the main theoretical points of the strength of disordered materials. As discussed in Sec. 2.4, the widely used Weibull and modified Gumbel distributions naturally arise from the extreme-value statistics if one assumes a particular form of the defect cluster size distribution in a randomly diluted network: (1) defect clusters are independent of each other, i.e., they do not interact with one another; (2) system failure is governed by the "weakest-link" hypothesis, and (3) there exists a critical defect cluster size below which the system does not fail, and it is possible to relate the critical size of a defect cluster to the material strength. In particular, if the defect cluster size distribution is described by a power-law, then the fracture strength obeys Weibull distribution, whereas an exponential defect cluster size distribution leads to the Gumbel distribution for fracture strengths [9, 329, 339, 340]. Theoretical arguments along these lines have been put forward in the context of lattice models, as discussed in Sec. 5.4. A different theoretical

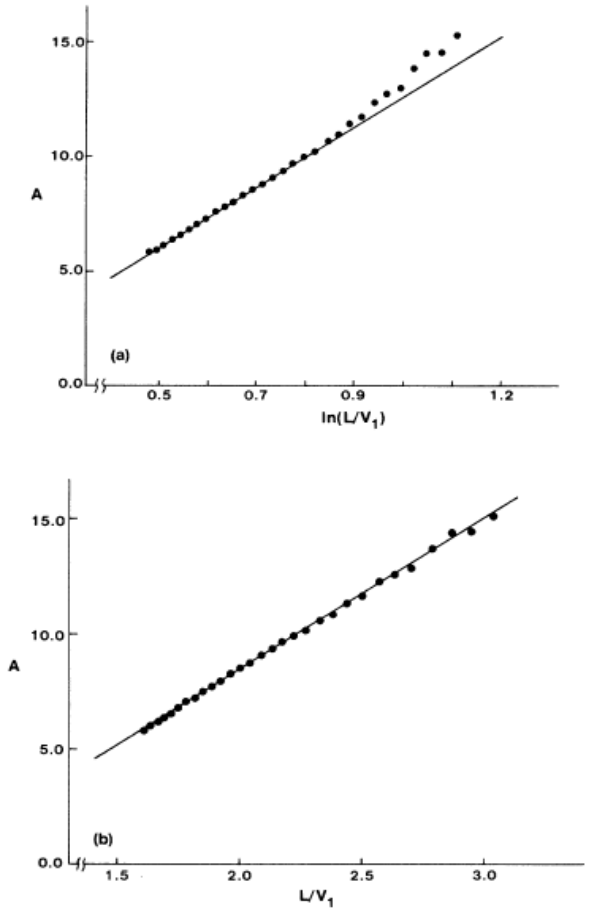


Figure 55. Examples of how the Gumbel and Weibull forms fit into the percolation disorder RFM data (from Ref. [316]).

approach is based fiber bundle models which yields in the case of ELS [14], a Gaussian strength distribution with variance proportional to $1/N$, where $N$ is the number of fibers [14]. The more interesting case of LLS [256], yields a mean fracture strength $\mu_f \equiv \langle \sigma_f \rangle$ decreasing as $1/\log(N)$, such that the strength of an infinite bundle system is zero. The fracture strength distribution follows Eq. (59), and is close to a Weibull form although it is difficult to determine its exact form [256]. Using renormalization techniques, an asymptotic size effect of the form $\mu_f^{-\delta} \sim \log(\log(L))$ was proposed in Refs. [339, 342–344] for LLS models.

Duxbury et al. [22, 316, 317] studied the distribution of fracture thresholds in the randomly diluted fuse networks with bond percolation disorder (see

Sec. 5.4). Fig. 55 shows simulation results [316] compared with the Gumbel-Ansatz. Subsequently, the fracture strength distribution was studied in a variety of lattice models with different local behavior including central-force spring models [328, 345], Born models [184], and bond-bending models [328]. These studies along with the analytical investigations based on largest stable defect size [165] concluded that the fracture threshold decreased with the system size $L$ as a power of $\log(L)$ and the fracture threshold distribution is best described by a double exponential (modified Gumbel) distribution. In these randomly diluted disorder problems, the defect cluster size distribution is exponential far away from the percolation threshold and follows a power law close to the percolation threshold. Consequently, in general, a Gumbel distribution better fits the fracture strengths distribution far away from the percolation threshold and a Weibull distribution provides a better fit close to the percolation threshold [9, 329, 339, 340].

In the case of RFM models with weak disorder, failure is dominated by the stress concentration effects around the crack tip, and hence the "weakest-link" hypothesis should be valid. Thus the fracture strength follows extreme-value theory and is distributed according to the Weibull or modified Gumbel distributions. The interesting scenario corresponds to the case of strong disorder, where neither Weibull nor Gumbel distribution applies well (see Ref. [346] for 2D RFM, Ref. [182] for 2D RSM, and Ref. [334] for 3D RFM). There are two main reasons behind this behavior:

(i) in the "weakest-link" hypothesis, the fracture strength is determined by the presence of few critical defect clusters, and is defined as the stress required for breaking the very first bond in the system. In materials with broad disorder, the breaking of the very first bond ("weakest-link") does not usually lead to the entire system failure (as is manifested with the scaling $n_p \sim N_{el}^b$ with $b = 0.93$ for 2D RFM with strong disorder), and hence a fracture strength distribution based on the importance of very first bond failure may not be applicable.

(ii) As discussed above in Sec. 6.2.3, the actual geometric crack cluster size distribution in the RFM at the peak load develops its own form, quite different from the initial defect cluster size distribution in randomly diluted networks. In general at the peak load of RFM simulations, the crack cluster distribution is represented neither by a power law nor by an exponential distribution (see Fig. 52 and Ref. [338]). Hence, neither the Weibull nor the Gumbel distributions fit the fracture strength distribution accurately.

Figure 56 shows the fracture strength density distributions for random thresholds fuse and spring models using the standard Lognormal variable, $\bar{\xi}$, defined as $\bar{\xi} = \frac{Ln(\sigma_f)-\eta}{\zeta}$, where $\sigma_f$ refers to the fracture strength defined as the peak load divided by the system size $L$, and $\eta$ and $\zeta$ refer to the mean

and the standard deviation of the logarithm of $\sigma_f$. The excellent collapse of the data for various fuse and spring lattices clearly indicates the universality of the fracture strength density distribution.

In addition, the collapse of the data in Fig. 56 suggests that $P(\sigma \leq \sigma_f) = \Psi(\bar{\xi})$, where $P(\sigma \leq \sigma_f)$ refers to the cumulative probability of fracture strength $\sigma \leq \sigma_f$, $\Psi$ is a universal function such that $0 \leq \Psi \leq 1$, and $\bar{\xi} = \frac{Ln(\sigma_f)-\eta}{\zeta}$ is the standard Lognormal variable. The inset of Fig. 56 presents a Lognormal fit for fracture strengths, tested by plotting the inverse of the cumulative probability, $\Phi^{-1}(P(\sigma_f))$, against the standard Lognormal variable, $\bar{\xi}$. In the above description, $\Phi(\cdot)$ denotes the standard normal probability function. As discussed in Ref. [334], a Lognormal distribution is an adequate fit for 3D random fuse models as well. This further confirms the notion of universality of fracture strength distribution in broadly disordered materials.

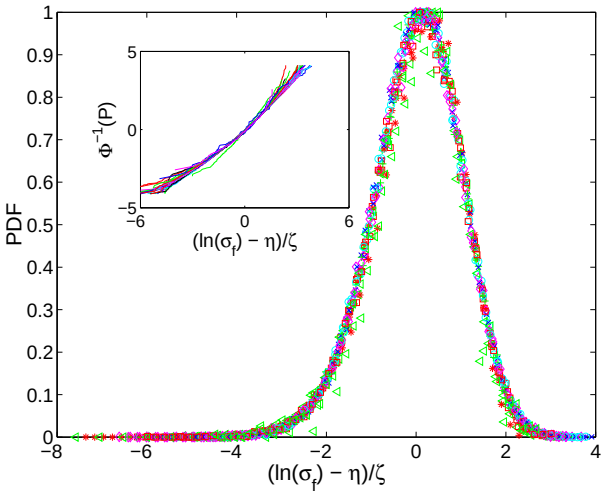


Figure 56. Universality of fracture strength distribution in the random thresholds fuse and spring models. Data are for different lattice system sizes, $L$, corresponding to triangular fuse lattice with uniform disorder ($L = \{4, 8, 16, 24, 32, 64, 128\}$), diamond fuse lattice with uniform disorder ($L = \{4, 8, 16, 24, 32, 64, 128\}$), triangular fuse lattice with power law disorder ($L = \{4, 8, 16, 24, 32, 64, 128\}$), and triangular spring lattice with uniform disorder ($L = \{8, 16, 24, 32, 64, 128\}$). The inset reports a Lognormal fit for the corresponding cumulative distributions.

The origin of a Lognormal strength distribution is not entirely clear from the theoretical point of view (for a heuristic argument see Ref. [346]). It is worth remembering that what determines the survival of a system is a quantity with strong sample to sample variations: the microcrack with the largest stress enhancement. In contrast to percolation disorder, this critical crack grows from the no-damage state in these simulations. In Sec. 6.2.3, we have discussed also the scaling of the connected crack clusters. It is worth remembering that the

stability of a given configuration results from two contradictory effects: stress enhancements and configurations (of fuses in the RFM) that are able to arrest the crack and make it stable (as is the case in LLS fiber bundles [276]). In experiments on paper, there are results that point out in a similar vein the combined role of local strength and local stresses, which can vary not only because of microcracking but also because of structural inhomogeneity [168].

**6.3.2** ***Size effects.*** Two forms have been proposed in the literature to express the size effects on mean fracture strength in randomly diluted lattice systems (percolation disorder): a simple power law scaling [9], consistent with the Weibull statistics,

$$\mu_f \sim L^{-\frac{2}{\bar{m}}}, \tag{96}$$

or a more complicated form [22,316,317,328,329,339,345,347], consistent with a modified Gumbel description,

$$\mu_f = (\frac{1}{A_1 \ + \ B_1 \ ln \ L})^{1/\delta} = (\frac{1}{ln(A_2 L^{B_1})})^{1/\delta}, \tag{97}$$

where $\bar{m}$ is the Weibull exponent, and $\delta$, $A_1 = \log A_2$ and $B_1$ are constants.

The inset of Fig. 57 presents the scaling of mean fracture strength, $\mu_f$, based on power law scaling $\mu_f \sim L^{-\frac{2}{\bar{m}}}$. From the nonlinearity of the plot, it is clear that the mean fracture strength does not follow a simple power law scaling. On the other hand, the scaling form $\mu_f^{\delta} = \frac{1}{A_1 \ + \ B_1 \ ln \ L}$ may represent the mean fracture strengths reasonably well even though the Gumbel distribution is inadequate to represent the cumulative fracture strength distribution. However, the fit results in coefficients that are extremely sensitive; namely, $\delta = -2.45$, $A_1 \approx -18.3$ ($A_2 \approx 10^{-9}$) and $B_1 \approx 20$ (see for instance, Fig. 5b of Ref. [346] for 2D RFM data) consistent with the divergent behavior reported in Refs. [22, 345] for randomly diluted systems.

Alternatively, Ref. [346] suggests a scaling form for the peak load (peak current), $\bar{I}_{peak}$, given by $\bar{I}_{peak} = C_0 L^{\alpha} + C_1$, where $C_0$ and $C_1$ are constants. Correspondingly, the mean fracture strength defined as $\mu_f = \frac{\bar{I}_{peak}}{L^{d-1}}$, is given by $\mu_f = C_0 \ L^{\alpha - d + 1} + \frac{C_1}{L^{d-1}}$, where $d = 2$ in 2D and $d = 3$ in 3D. Using this scaling law, the two-dimensional RFM and RSM fracture strength data are plotted as shown in Fig. 57. The results presented in Fig. 57 indicate that the exponent $\alpha = 0.97$ for RSM and $\alpha = 0.96$ for RFM using both triangular and diamond lattice topologies.

The results for three-dimensional random fuse models are similar. A power law scaling form $\mu_f \sim L^{-\frac{2}{\bar{m}}}$ consistent with a Weibull distribution does not

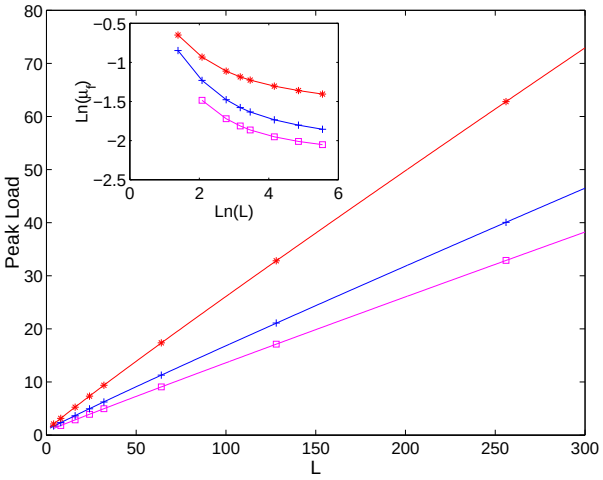


Figure 57. Proposed scaling law for the mean fracture strength ($F_{peak} = C_0 L^{\alpha} + C_1$). (1) Triangular spring network (symbol: -□-): $\alpha = 0.97$. (2) Triangular fuse network (symbol: -*-): $\alpha = 0.956$; (3) Diamond fuse network: (symbol: -+-): $\alpha = 0.959$; The corresponding Weibull fit for the mean fracture strength is shown in the inset.

represent an adequate fit (see Ref. [334]). On the other hand, a scaling of the form $\mu_f^{\delta} = \frac{1}{A_1 + B_1\ ln\ L}$ results in a very high value of $\delta = -7.5$ for the exponent and the high values for the coefficients $A_1 = -156380$ and $B_1 = 85050$ indicating the divergence behavior similar to that observed in 2D RFM and in randomly diluted systems [22,345]. Alternatively, using the scaling form $\bar{I}_{peak} = C_0 L^{\alpha} + C_1$, the mean fracture strength data for 3D RFM results in a value of $\alpha = 1.95$ [334].

Since a very small negative exponent $(\alpha - d + 1)$ is equivalent to a logarithmic correction, i.e., for $(d - 1 - \alpha) << 1$, $L^{\alpha - d + 1} \sim (ln\ L)^{-\psi}$, an alternative expression for the mean fracture strength may be obtained as $\mu_f = \frac{\mu^{\star}}{(ln\ L)^{\psi}} + \frac{c}{L}$, where $\mu^{\star}$ and $c$ are constants that are related to the constants $C_0$ and $C_1$. This suggests that the mean fracture strength of the lattice system decreases very slowly with increasing lattice system size, and scales as $\mu_f \approx \frac{1}{(ln\ L)^{\psi}}$, with $\psi \approx 0.15$, for very large lattice systems. The same asymptotic scaling relation (i.e., $\mu_f \approx \frac{1}{(ln\ L)^{\psi}}$) was also conjectured in Ref. [328,329] for broadly disordered materials.

**6.3.3** ***Strength of notched specimens.*** Above, we have investigated the fracture of unnotched specimens, but from an engineering point of view, scaling of fracture strength in pre-notched specimens is of significant interest [52, 73, 74, 161, 348]. The size effect in this case is often given by a scaling of the form $\mu_f \propto a^{-1/2}$, where $a = a_0 + c_f$ is the effective crack size, $a_0$ is

the initial crack (notch) size, and $c_f$ is the FPZ size surrounding the crack tips [52, 73, 74, 161, 348]. As we have noted in the previous section, a logarithmic size effect is observed in 2D and 3D simulations using the random thresholds models (RFM and RSM) with both uniform ($\Delta = 1$) and power law ($\Delta = 20$) thresholds disorder. The difference between $a^{-1/2}$ size effect in the engineering literature [52, 73, 74, 161, 348] and the typical logarithmic size effect in the statistical physics literature is due to two aspects: i) initial relative crack size $a_0/L$, and ii) disorder.

A simulation of an initially cracked (or notched) lattice system is reported in Fig. 58 for a 2D RFM. It illustrates the possible role of disorder in determining the ultimate sample strength and its scaling with $L$ and/or $a_0/L$. The scenario corresponds to some initial distributed damage followed by the crack roughening, which at the trivial level indicates the effect of crack arrest due to strong bonds, followed finally by the point of catastrophic failure.

The size effects obtained in such notched specimens using the 2D RFM with uniform thresholds disorder are presented in Fig. 59 showing the scaling of fracture strength with system size for a fixed initial crack size, $a_0/L$. The results can be fitted by a power law of the type

$$\mu_f \propto L^{-m}, \tag{98}$$

where the scaling exponent $m$ is significantly influenced by $a_0/L$: for small $a_0/L$ values, $m$ is very small, and is equivalent to a logarithmic correction as in Sec. 6.3.2 while for large $a_0/L$ values, $m$ approaches 1/2 as predicted by LEFM [52]. The reason for this behavior is that in the small $a_0/L$ regime, fracture is dominated by disorder, whereas in the large $a_0/L$ regime, fracture is controlled by the initial crack.

A weak disorder leads to the standard $m = 1/2$ scaling, while for strong disorder we have a logarithmic size effect. One way to understand the data - qualitatively - is to take note of the fact that for sure a typical sample can accumulate damage upto a number of broken bonds $n_p$ for which the notch-induced crack is still stable. E.g. for a crack of size "$a_0 = 1$" this implies, that $n_p$ can be interpreted roughly as a density of broken fuses, for which the integral of the failure threshold distribution corresponds to the typical strength of the system if the bulk damage is excluded. This, in turn, is given by $\pi/4$ times the mean of the threshold distributions times a numerical $O(1)$ factor, coming from the number of fuses most affected by the current enhancement (at most two). The damage will then produce a number of microcracks competing with the flaw, which is of size $a_0$. Increasing the control parameter $a_0/L$ implies, that the damage $n_p$ will decrease since the current enhancement increases. Eventually, the notch will win over the other flaws, but this is a slow process.

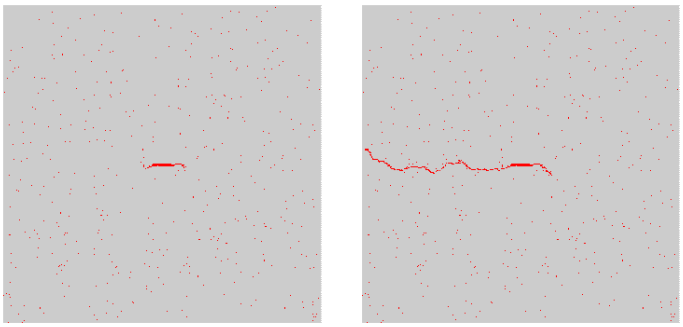

Figure 58. Evolution of damage in a notched sample. Although diffuse damage is present, a wandering fracture line starts from the notch breaking the entire lattice.

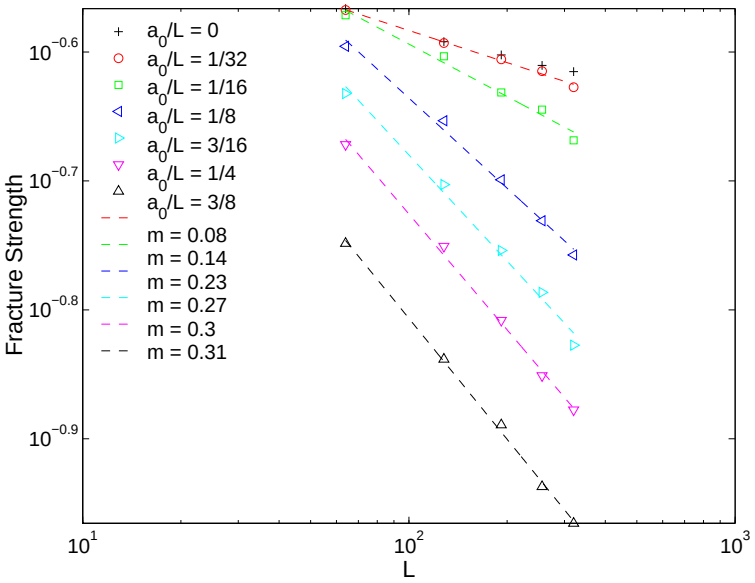


Figure 59. Size effects in notched specimens with uniform thresholds disorder. The effective scaling exponent of mean fracture strength depends on the ratio $a_0/L$.

### 6.4 *Crack roughness*

Lattice models for fracture have been used in the past to analyze the roughness of the crack surfaces in various geometries. The RFM has been numerically simulated in two [335, 347, 349, 350] and three dimensions [351, 352] using various types of disorder. Other lattice models have also been simulated for this purpose, including the beam model [353], the RSM and the Born model [216, 354]. Interfacial (planar) cracks have been studied with the

RFM [298], the beam model [299], and a long-range scalar model [321]. Due to numerical limitations, earlier numerical simulations mostly considered global measurements for the crack roughness, while more recent results explored other quantities and the possibility of anomalous scaling.

Let us first discuss the widely studied RFM [335,347,349–352]. As discussed in Sec. 4.1 the plastic version of the RFM yields on minimum energy surfaces, which in two dimensions corresponds to the directed polymer, characterized by $\zeta = 2/3$. The results of numerical simulations of the brittle RFM yield values close to $\zeta \simeq 0.7$ for a variety of disorder distributions [349] suggesting that indeed the fracture surface would result from minimum energy considerations [335]. High quality data for the surface roughness in $d = 2$ have been recently published in Ref. [350] ruling out this interpretation. The only caveat would be if the effective disorder would become correlated due the microcracking, which can change the $\zeta$ [347].

Several methods have been devised to characterize the roughness of an interface and their reliability has been tested against synthetic data [291]. If the interface is self-affine all the methods should yield the same result in the limit of large samples. In Fig. 60a we report the local width for triangular random fuse lattices for different sizes $L$. The curves for different system sizes do not overlap even for $l \ll L$ which would be the scenario when anomalous scaling is present (Sec. 2.6.1). The global width scales with an exponent $\zeta = 0.83 \pm 0.02$ ($\zeta = 0.80 \pm 0.02$, obtained for diamond lattices [350]). On the other hand the local width increases with a smaller exponent, that can be estimated for the larger system sizes as $\zeta_{loc} \simeq 0.7$. A more precise value of the exponents is obtained from the power spectrum, which is expected to yield more reliable estimates. The data reported in Fig. 60b are collapsed using $\zeta - \zeta_{loc} = 0.13$ ($\zeta - \zeta_{loc} = 0.1$ for diamond lattices). A fit of the power law decay of the spectrum yields instead $\zeta_{loc} = 0.74$ ($\zeta = 0.7$ for diamond lattice), implying $\zeta = 0.87$ ($\zeta = 0.8$ for diamond lattice). The results are close to the real space estimates and we can attribute the differences to the bias associated to the methods employed [291]. Although the value of $\zeta - \zeta_{loc}$ is small, it is significantly larger than zero so that we would conclude that anomalous scaling is present. This implies in analogy to other theoretical scenarios that there is an external transverse lengthscale, increasing as a function of $L$. The question now becomes, what about the origins of such a scale?

While the local exponent is close to the directed polymer value $\zeta = 2/3$, the global value is much higher. It is also interesting to remark that for directed polymers anomalous scaling is not expected to be present, even with noise which has a more complex character [32]. The result obtained in other lattice models are partly similar, posing the question whether there is a broad universality class for fracture surfaces of disordered lattices. In particular, some measurements reported in the literature are $\zeta = 0.7$ for a RFM with dilution

disorder [347], $\zeta = 0.87$ for the beam model in the limit of strong disorder [353], $\zeta_{loc} = 0.66$ in the Born model for a variety of parameters [216].

An additional tool to characterize the roughness is provided by the distribution $p(W)$ of the crack global width. This distribution has been measured for various interfaces in models and experiments and typically rescales as [347, 355, 356]

$$p(W) = p(W/\langle W \rangle)/\langle W \rangle, \tag{99}$$

where $\langle W \rangle \sim L^{\zeta}$ is the average global width. As shown in Fig. 61 the distributions can be collapsed well using Eq. (99) for diamond and triangular lattices [350], providing additional evidence for universality. Moreover, the scaling function follows a Lognormal distribution.

The results of simulations in $d = 3$ are more difficult to interpret coherently since the numerical data is limited to small system sizes and fewer statistical samples. The higher computational cost of 3D simulations compared to 2D simulations restricts the consideration of 3D simulations to relatively small system sizes and smaller statistical sampling. It was debated whether the fracture roughness of the RFM could be described by a minimum energy surface, corresponding to $\zeta \simeq 0.41$. Simulations of the model with weak disorder lead to a similar value, but the exponent increases for stronger disorder [335, 352]. Ref. [351] proposes an extrapolation leading to $\zeta = 0.62$, but the numerical estimates fluctuate considerably, depending on the method employed and on the considered disorder distribution. Recently performed extensive simulations of 3D RFM have obtained similar results. In particular, an analysis of the width and the power spectrum data results in a value of $\zeta \simeq 0.52$, with possible anomalous scaling corresponding to a local value of $\zeta_{loc} \simeq 0.42$ (see Fig. 62). Finally, results of three dimensional simulations have also been reported for the Born model (on FCC lattices), yielding $\zeta_{loc} \simeq 0.5$ from power spectrum and local width calculations.

An interesting point to note is the consistency between the scaling of final crack width and the scaling of localization length $\xi$ discussed in Sec. 6.2.2. For the 2D RFM triangular lattice system, we have $\zeta = 0.83 \pm 0.02$, which is consistent with the scaling of the localization length $\xi \sim L^{0.8}$ used in the data collapse of damage profiles in the post-peak regime. The center of mass shifting of the damage profiles for the purpose of averaging the damage profiles makes this consistency between the final crack width and the localization length $\xi$ of the damage profiles self-evident. In addition, this agreement supports the idea that the post-peak damage profile is predominantly due to the localization produced by the catastrophic failure, which at the same time results in the formation of the final crack. Similar behavior is observed in three-dimensional RFM; namely, the scaling of final crack width $\zeta \simeq 0.52$ consistent with the

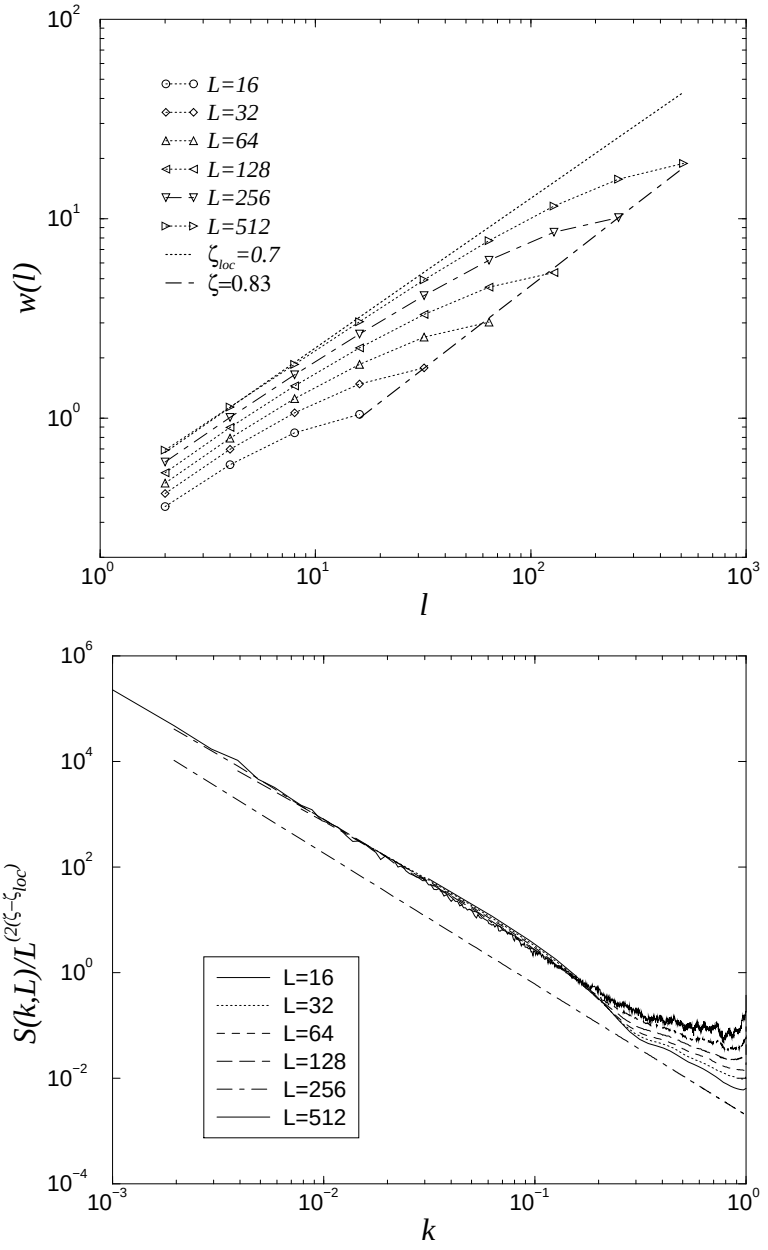


Figure 60. (a) The local width $w(l)$ of the crack surface for different lattice sizes of 2D RFM triangular lattice systems plotted in log-log scale. A line with the local exponent $\zeta_{loc} = 0.7$ is plotted for reference. The global width displays an exponent $\zeta > \zeta_{loc}$.(b) The corresponding power spectrum in log-log scale. The spectra for all of the different lattice sizes can be collapsed indicating anomalous scaling.

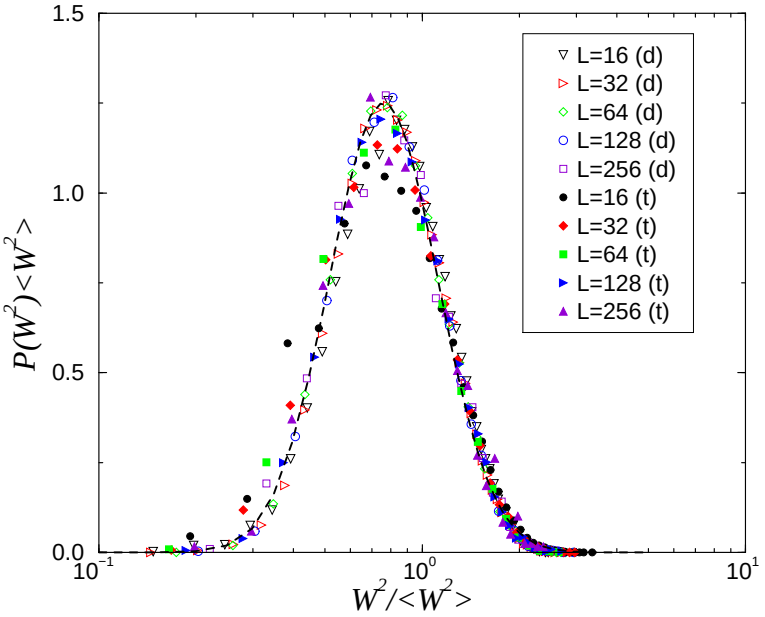


Figure 61. The distribution of the crack width is universal for diamond and triangular random fuse lattices. A fit with a log normal distribution is shown by a dashed line.

scaling of localization length $\xi \sim L^{0.5}$ [338] of the post-peak damage profiles. Interestingly, the same consistency in scaling between the final crack width and the localization length of the post-peak damage profiles is observed in the 2D random spring models as well. The final crack width scales as $W \sim L^{0.64}$ (see Ref. [216]), and the localization length $\xi$ of the post-peak damage profiles scales as $\xi \sim L^{0.65}$ (see Fig. 6 of Ref. [182]).

### 6.5 *Avalanches*

The loading curve of fracture models, such as the RFM, is characterized by avalanches of failure events. As discussed in Sec. 5.1, fiber bundle models represent a useful idealization providing a qualitative description of the avalanche phenomenology and their statistics. On this basis one would expect to find a power law distribution with a cutoff changing with the applied load. An important theoretical question is whether the scaling exponents measured in lattice models are universal, i.e. they are the same in different models. On the experimental side, the main challenge is to relate the avalanche exponents to the acoustic emission statistics recorded in experiments. In both cases, one can ask what is the relation of the avalanches, and the underlying dynamics, to crack formation and damage mechanics. In lattice model simulations

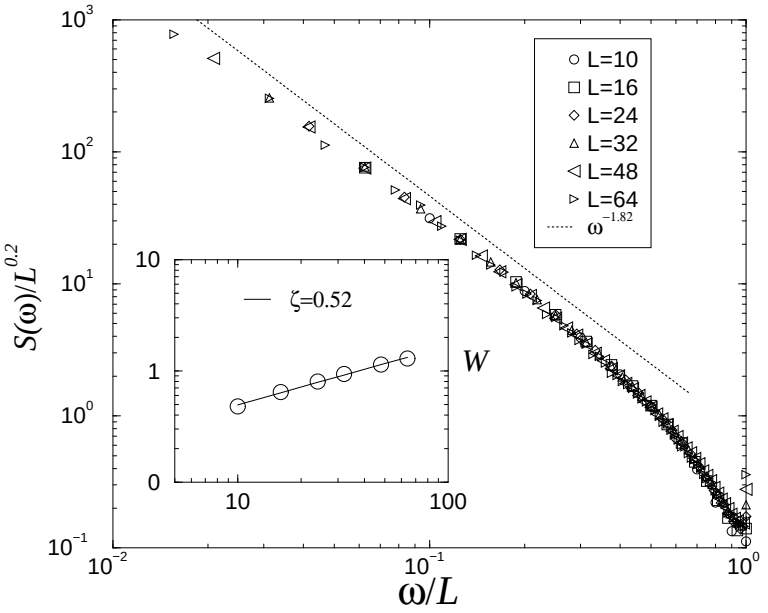


Figure 62. The power spectrum of the crack surface of the three dimensional RFM. The spectrum exponent $2\zeta + 1 = 1.82$, corresponds to $\zeta_{loc} = 0.41$. The global width scales with $\zeta = 0.52$ (see inset), so that the power spectrum should be normalized by $2(\zeta - \zeta_{loc}) \simeq 0.2$

one typically defines the avalanche size $s$ as in the FBM (see Sec- 5.1.1) by counting the number of broken bonds that fail without any further increase in the applied load. Although this avalanche size is not directly equivalent to the acoustic emission energy, under some assumption, it is possible to relate the two distributions as discussed in the following.

The avalanche statistics of the RFM has been reported for two dimensional [253,286,287,350] and three dimensional simulations [352,357]. While initially it was believed that FBM and RFM were in the same universality class [253, 286, 287] with exponent $\tau = 5/2$, recent larger scale simulations displayed deviations from the expected behavior. The puzzling fact is, however, that the estimated value of the exponent $\tau$ was found to be dependent on the lattice topology. This is contrary to any expectation, since in critical phenomena the exponents depend only on symmetries and conservation law, but not on the type of lattice or similar small scale details. An opposite situation is found in $d = 3$ where early simulations reported a strong deviation from mean-field, $\tau \sim 2 < \tau_{FBM} = 5/2$ [352] while more recent results seem in agreement with this value [357]. Let us discuss all these results in detail.

First, one can define avalanches increasing the voltage (deformation) or the current (force), but we do not expect strong differences for these two cases, so in the following we always refer to the latter. If one simply records the

distribution considering all the avalanches, one observes a power law decay culminating with a peak at large avalanche sizes. As in the FBM, the peak is due to the last catastrophic event which can thus be considered as an outlier and analyzed separately, avoiding possible bias in the exponent estimate (this problem is present in Ref. [358] reporting simulations of a central force model). When the last avalanche is removed from the distribution the peak disappears and one is left in these models with a power law (see Ref. [350]). On the other hand, the size distribution of the last avalanche is Gaussian [182, 350, 359].

Next, as discussed in Sec. 5.1.1, one should distinguish between distributions sampled over the entire load history, and those recorded at a given load. In the first case, the integrated distribution has been described by a scaling form [350]

$$P(s, L) = s^{-\tau} g(s/L^D), \tag{100}$$

where $D$ represents the fractal dimension of the avalanches. To take into account the different lattice geometries, it is convenient to express 2D scaling plots in terms of $N_{el}$ rather than $L$

$$P(s, N_{el}) = s^{-\tau} g(s/N_{el}^{D/2}). \tag{101}$$

A summary of the results for two-dimensional lattices are reported in Fig. 63, showing that in the RFM $\tau > 5/2$, with variations depending on the lattice topology, while the result reported for the RSM is instead very close to $\tau = 5/2$. As for the avalanche fractal dimension, $D$ varies between $D = 1.10$ and $D = 1.18$, indicating almost linear crack (which would correspond to $D = 1$). Note that the last avalanche has been studied earlier in the context of damage, and its geometrical properties in the context of crack roughness. The variation of $D$ should be compared to that of $\zeta$ in the same systems. Three dimensional results are plotted in Fig. 64 for the RFM [357]. Again the agreement with FBM results is quite remarkable.

The distribution of avalanche sizes sampled at different values of the current $I$ is obtained by normalizing the current by its peak value $I_c$ and dividing the $I^* = I/I_c$ axis into several bins. The distribution follows then a law of the type

$$p(s, I^*) = s^{-\gamma} \exp(-s/s^*), , \tag{102}$$

where the cutoff $s^*$ depends on $I^*$ and $L$, and can be conjectured to scale as

$$s^* \sim \frac{L^D}{(1 - I^*)^{1/\sigma} L^D + C}, \tag{103}$$

where $C$ is a constant. Integrating Eq. (102) we obtain

$$P(s, L) \sim s^{-(\gamma+\sigma)} \exp[-sC/L^D]. \tag{104}$$

which implies $\tau = \gamma + \sigma$. We recall here that in the FBM $\gamma = 3/2$ and $\sigma = 1$ (see Sec. 5.1.1). Fig. 65 reports a series of distributions obtained for the RFM for different values of the currents [350]. The best fit for the scaling of the distribution moments as a function of $I$ and $L$ (Eq. (103)), and a direct fit on the curves suggest $\gamma \approx 1.9 - 2$, $\sigma \approx 1.3 - 1.4$ in $d = 2$ and $\gamma \approx 1.5$, $\sigma \approx 1$ in $d = 3$.

In summary, the avalanche distribution for RFM is qualitatively close to the prediction of the FBM (i.e. mean-field theory). Apparently non-universal (lattice type dependent) corrections are present in $d = 2$, but the problem disappears in $d = 3$. This could be expected building on the analogy with critical phenomena, where exponents are expected to approach the mean-field values as the dimension is increased. Simulations of other models have been reported in the literature: the distribution obtained in Ref. [182] for the RSM is very close to the FBM result (see Fig. 63). The avalanche distribution has been also reported for the Born model ($\tau \approx 2$ [360]), the bond-bending model ($\tau \approx 2.5$ [287]), the continuous damage model ($\tau \approx 1.3$ [175]).

To conclude, we discuss the issue of the relation between the AE distribution and and the avalanche size distribution. These two are, contrary to usual indications in the literature, not the same. The same holds even more clearly for the acoustic amplitude distribution. Acoustic waves were incorporated in a scalar model in Ref. [227], and the AE energy distribution was measured, with an exponent $\beta \simeq 1.7$. This exponent can be related to $\tau$ if we assume that the typical released AE energy of an avalanche of size $s$ scales as $\epsilon \sim s^\delta$, with $\delta = 2$ (i.e. the scaling relation is $\tau = 1 + \delta(\beta - 1)$). This was verified in the model of Ref. [227], but also in the RFM defining $\epsilon$ as the dissipated electric energy during one event seems to agree [125].

## 7 Discussion and outlook

We would like to conclude the present review by trying to answer two essential questions: (i) what can be learned from statistical models in order to reach a better understanding of fracture in quasi-brittle materials and interpret relevant experiments and (ii) what kind of developments can be foreseen to improve the current theoretical/modeling framework. The first question involves as well an assessment of the possible advantages of the statistical mechanics strategy with respect to traditional damage mechanics approaches. On the other hand, answering the second question will also help to clarify the

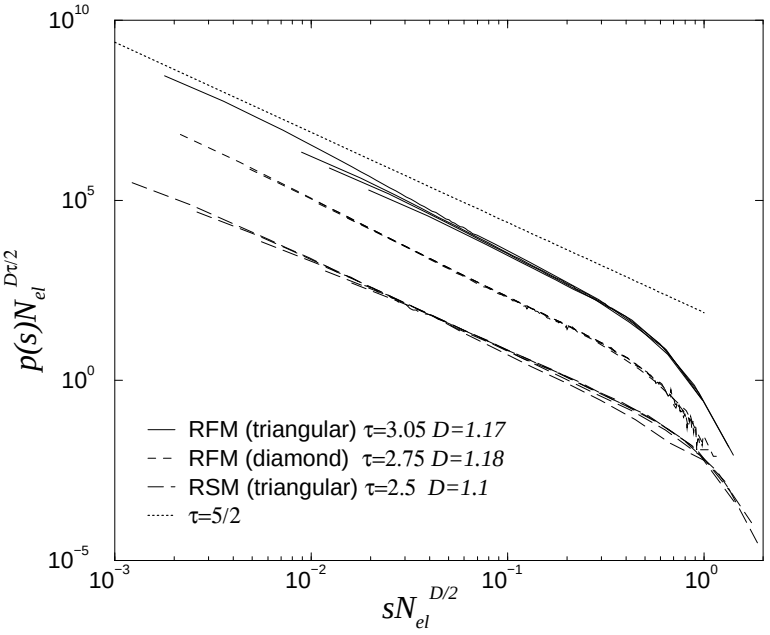


Figure 63. A summary of two-dimensional results for avalanche distributions integrated along the entire loading curve. The results are for the RFM on triangular and diamond lattices [350] and for the RSM [182]. Data for different lattice sizes have been collapsed according to Eq. (101). A line with exponent $\tau = 5/2$ is reported for reference.

limitations of statistical lattice models and their role in the future.

The macroscopic behavior of lattice models is well described using the terminology of phase transitions and the ensuing picture is conceptually rather simple: in the stress-controlled case crossing the peak-load implies a first-order transition to a "broken state". This means that regardless of system size and disorder strength, the correlations in damage are local albeit with a growing characteristic length. This lengthscale does not diverge however as the peak-load is approached in contrast to that of a second-order transition. Such a picture has automatic consequences for the scaling of thermodynamic quantities as the conductivity or stiffness, damage and strength distributions. In particular, scaling laws inspired from critical phenomena typically fail to describe the size dependence of these quantities. The statistical properties are instead well captured by relatively simple laws, such as Gaussian or Lognormal distributions, whose precise origin, however, is not always clear and remains a topic for future research. There are still interesting issues left, such as the most appropriate mathematical framework for measuring the damage anisotropy and correlations, or understanding the dynamics of microcrack populations. It would be important to carry out an extensive analysis for vectorial fracture

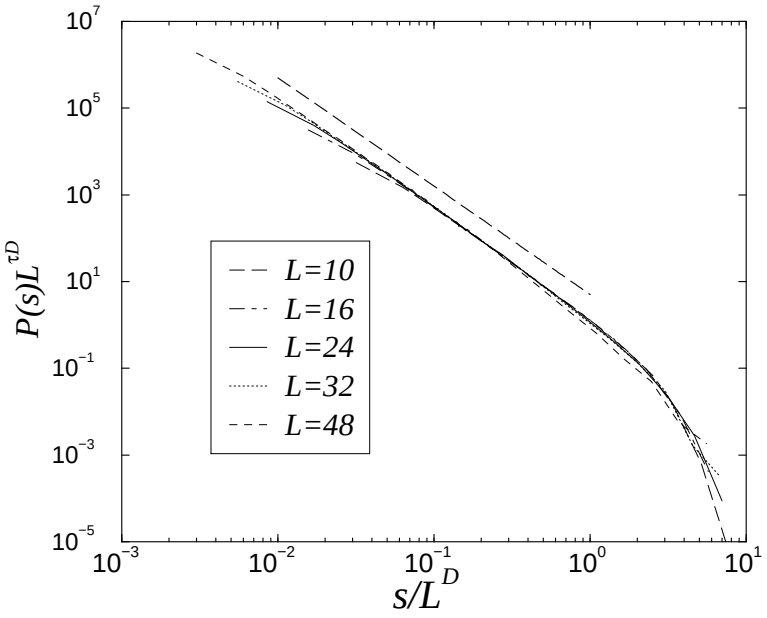


Figure 64. Data collapse of the integrated avalanche size distributions for the three dimensional RFM. The exponents used for the collapse are $\tau = 2.5$ and $D = 1.5$. A line with a slope $\tau = 5/2$ is reported in Ref. [350].

models, even though such quasistatic brittle fracture models are expected to have the same kind of "phase diagram" in the statistical mechanics language. Presumably allowing for several modes of element failure will also influence the right description of damage, summarized by the classical damage mechanics question whether it makes sense to use scalar damage parameter $D(\vec{x})$.

Next we would like to summarize with a few points the picture obtained from the theoretical approaches discussed in Sec. 5 and the numerical simulations reported in Sec. 6 and compare the results with the experimental data analyzed in Sec. 3. An additional question that naturally follows from statistical models is the role of internal disorder for macroscopic damage laws used in engineering applications.

### 7.1 *Strength distribution and size effects*

One of the successes of statistical models of fracture has been to shed light into the scaling of strength with sample size and the associated distributions. There are indications that the asymptotics of extremal statistics are not the only alternative to explain the strength distribution, which results instead from cooperative phenomena or fluctuations in the damage accumulation. While for

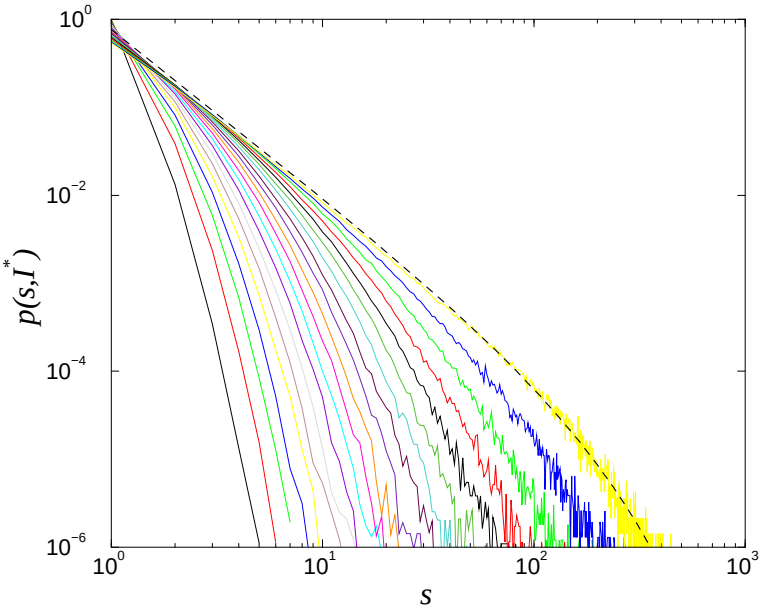


Figure 65. The avalanche size distributions sampled over a small bin of the reduced current $I^*$ for a diamond lattice of size $L = 128$. The dashed line represents a fit according to Eq. (102) with $\gamma = 1.9$ (from Ref. [350]).

weak disorder the Weibull distribution provides an adequate fit to the data, for strong disorder we observe a Lognormal strength distribution. Whether this is a general result valid at all scales or the signature of a crossover behavior to Gumbel or Weibull scalings, still remains to be explored.

A possible pathway to understand these results could stem from fiber bundle models (see Sec. 5.1). Under LLS conditions the model displays an extremal type distribution and a Logarithmic size effect. Conversely under ELS the distribution becomes Gaussian and size effects are absent. A clever way to interpolate between LLS and ELS was suggested by Hidalgo et al. [277] through a long-range rule in which the stress is transfered as $1/r^\gamma$. The crossover between LLS and ELS is identified with $\gamma \simeq d$, which corresponds with the exponent of the Green function obtained from lattice models, such as the RFM. Hence these models lie exactly at the boundary between LLS and ELS and the Lognormal distribution could then arise from the competition between local and global effects in a strongly disordered environment. Here, we would like to call for further basic science -oriented experiments. In the materials science -community it is customary to use the Weibull scaling to describe strength. However, it is clear that it is very rare to have a situation in which one would a priori expect that the conditions underlying the Weibull statistics are valid.

Lattice models are also useful to analyze the effect on strength coming from

the interplay between elastic interactions and disorder in notched samples. For instance, the data displayed in Sec. 6.3.3 show the various mechanisms by which disorder can mask the classical LEFM prediction involving a $1/\sqrt{a_0}$-type scaling. The RFM has typically a rather small fracture process zone which decreases in size, for a fixed notch-to-sample size -ratio $a_0/L$. The simple lesson we can draw from the model is that in practice one may, for a limited range of sample sizes, expect to get almost any strength exponent (in the law $\sigma_f \propto L^{-m}$ ) between $m = 0$ (or logarithmic behavior) and the $m = 1/2$ prediction indicated by LEFM.

It is interesting to close the present discussion by analyzing the predictions for strength coming from two other theoretical frameworks commonly used to interpret statistical properties of fracture, namely percolation (Sec. 5.4) and depinning (Sec. 5.3). Percolation describes rigorously the infinite disorder limit of lattice models, where stress enhancement is irrelevant, the bonds fail one by one, and no real size effect is expected besides the small corrections associated with finite size scaling. The infinite disorder limit is useful as a theoretical idealization but is not relevant in practical cases, where the disorder distribution might be broad but remains normalizable. In that case, only the initial stage of damage accumulation resembles percolation, but eventually a catastrophic process is initiated and size effects, both in damage and strength are observed in agreement with experiments.

The depinning approach is applicable instead to the weak disorder limit, single crack limit. Strong inhomogeneities would break up the single valued crack interface that is the starting assumption of the theory. According to the depinning scenario, the crack interface moves, eventually leading to the failure of the sample, when the stress intensity factor on the crack overcomes a critical threshold $K_c$. Since we deal here with a non-equilibrium phase transition, as in percolation, we do not expect to see size effects in $K_c$, besides the usual finite size corrections (i.e. $K_c > 0$ for $L \to \infty$). Other possible size effects are hidden in the definition of the stress intensity factor. In other words, a depinning transition alone can not account for the observed size effects but can at best be used to describe the crack dynamics and morphology once crack growth has been initiated.

### 7.2 *Morphology of the fracture surface: roughness exponents*

We have discussed both the experimental (in Sec. 3.2), theoretical (in Sec. 5.3) and simulation-based (in Sec. 6.4) crack roughness analysis. As we discussed extensively there are several possible definitions of the roughness exponent, depending on the experimental conditions (dimensionality of the sample, loading mode) and on the measured surface properties (in plane or out of plane, parallel or perpendicular, local or global roughness). This variety of exponents

| exponent | exp. | RFM | DT-LR | DT-SR |
|---|---|---|---|---|
| $\zeta$ 2D local (i), | 0.6-0.7 | $0.7 \pm 0.1$ | - | - |
| $\zeta$ 2D global (i) | - | $0.8 \pm 0.1$ | - | - |
| $\zeta$ 3D planar crack (ii) | 0.6 | fractal | 0.39 | 0.63 |
| $\zeta_\perp$ 3D local (iii) | 0.4-0.5 (ss) 0.8 (ls) | 0.4 | log | - |
| $\zeta_\parallel$ 3D local (iii) | 0.6 | 0.4 | - | - |
| $\zeta_\perp$ 3D global (iii) | 1.2-1.3 | 0.5 | - | - |

Table 1. A summary of the values of the roughness exponent measured in experiments, in the RFM and in the depinning transition (DT) scenario, both with long-range (LR) and (SR) interactions. Refer to Sec. 2.6.1 for the definition of the exponents, to Sec. 3.2 for details about experiments, to Sec. 6.4 for the RFM results and to Sec. 5.3 for the depinning transition.

makes a direct comparison between theory and experiments quite involved. In order to simplify this task we report in Table 1 the values of the roughness exponents measured in experiments, as well as the predictions of the models.

A direct comparison of the exponent values leads to two main conclusions: first, the exponents agree "roughly" in two dimensions (i.e. $\zeta \simeq 0.7$) - depending on the case considered - but in three dimensions the numerical value is significantly smaller than the experimental one, $\zeta_{\rm loc} \simeq 0.4$ and $\zeta \simeq 0.5$ in simulations while $\zeta_{\rm loc} \simeq 0.8$ and $\zeta \simeq 1.2$ in experiments. This discrepancy is quite striking given the large range over which $\zeta_{\rm loc}$ can be observed in experiments. Second, The *physical mechanism* to crack roughening is still not understood even in the case of the RFM, not to mention other more realistic models and of course experiments.

From the experimental point of view, presently it is not completely clear if the 3D fracture surface exponents are universal, and what kind of regimes can be found. The crucial lengthscales seem to be that of FPZ [89,92], $\xi_{FPZ}$, and in some cases one related to voids formed ahead of the crack tip [95]: their density, and typical size. From the model point of view, it is crucial to underline here the main implication of the observed catastrophic failure occurring after peak-load and the lack of localization before this point: the roughness of the crack arises in the last abrupt "avalanche". This has important consequences for the modeling strategies, since quasi-static models such as the ones we are discussing here may become inappropriate when the crack grows unstable. It would be necessary to incorporate a more realistic dynamics, possibly including sound waves or other dynamical effects, or some process leading to residual strength.

A further relevant theoretical point is the question of the universality of the roughness exponent, an hypothesis supported by ample experimental evidence. Early RFM simulations suggest that $\zeta$ does not depend on the disorder strength [349], while recent results indicate as well an independence of the lattice type [350]. It would be very interesting to consider in more de-

tail comparisons to/within truly vectorial (beam or bond-bending) models to see their roughness characteristics. This also holds for crack growth experiments from notches, in which the interaction of dominating crack with diffuse damage could be investigated. An important aspect stems from the connection between fracture energy (or toughness) and the crack shape. It should be mentioned that the amplitude $A$ of the roughness (as in $w \propto AL^{\zeta}$) usually increases as the prefactor of strength decreases if the disorder is varied. Thus we may conclude that "rough" does not necessarily imply "tough", to answer the original question posed 20 years ago in Ref. [88].

### 7.3 *Crack dynamics: avalanches and acoustic emission*

The statistical properties of acoustic emission also remain to be explained, completely. Quasistatic lattice models qualitatively predict the correct behavior: a power law distribution of avalanche events, with an activity increasing as the failure point is approached. The scaling behavior is well captured by mean-field theory, as exemplified by fiber bundle models, with some deviations from the analytical predictions in the two-dimensional RFM (where $\tau > 5/2$), but almost perfect agreement in $d = 3$ and for the RSM. The apparent success of mean-field theory is probably related to the occurrence of a first-order transition in presence of long-range elastic interactions. In these conditions, the spinodal instability with the related mean-field scaling is accessible even in low dimensionality. From the point of view of the experimental comparison, however, lattice models typically predict a too large energy exponent $\beta$. It is not known as to whether this problem results from any of the known possible caveats, such the brittle nature of the models, the dispersion of the acoustic waves and data in experiments, or the possibility that in reality one can not separate the time-scales of stress relaxation and loading, as assumed in the quasi-static models. For this reason we would like to call for more experiments in various loading conditions (tensile, creep, fatigue etc.), for varying materials so that the influence of plasticity, time-dependent response, and localization can be studied.

Brittle fracture models are due to the first-order nature of the final failure such that their predictability is inherently weak, though there have been (mainly experimental) attempts to show the opposite [121, 151, 361]. For the practically minded scientist, the main lessons are that brittle materials have a tendency to fail abruptly, exhibit critical-looking noise, and their fracture statistics depend crucially on the presence of large flaws and on the actual disorder.

### 7.4 *From discrete models to damage mechanics*

Lattice models have been used to describe qualitatively the stress-strain curves of materials as noted earlier. Here, we have overviewed, mainly in the context of the RFM, the basic tenants of damage accumulation. The crucial questions are: how to average over samples, what kind of correlations arise in the damage, including localization, and in general what one learns from a representative volume element -idea.

Large-scale simulations provide evidence for strong self-averaging for the $D$, damage variable, in the RFM. This is connected with the notion that while the damage accumulated becomes anisotropic, it still has only a finite correlation length $\xi$ (both parallel and perpendicular to the load) up to the peak load. Meanwhile, as one takes the limit $L \to \infty$ the strength decreases and actually the self-averaging gets stronger since $L/\xi$ remains large even up to the peak load. Again, it would be useful to test these conclusions in vectorial models. One question not addressed here in detail is the probability distribution of $P(D, V)$, which is related to $\xi(V)$ via a simple application of the central limit theorem. Again, we would like to call for experiments, including looking at damage patterning and localization to also stimulate the further development of models.

### 7.5 *Concluding remarks and perspectives*

We think that there are substantial advances to be made within the confines of lattice fracture models with inelastic, or time-dependent effects incorporated. Even simulations of elastic-plastic fracture in this respect are still awaiting, though these have no rate-dependence. As was very briefly mentioned in Sec. 3.4, there are statistical laws in fracture and deformation processes that are not simply "brittle". For many of these cases we expect that models akin to the RFM and its generalizations will prove to be useful.

There are some simple ingredients that "improved" models might contain and some simple developments they might lead to. For one, we would like to see the invention of lattice models that allow for true damage localization before the peak load. This would for instance produce damage dynamics comparable to the experimental "b-value" analysis of AE, to name but one issue. Similarly, one would need models that allow for stable crack growth beyond the peak load ($V$-controlled ensemble for equivalent RFM's).

In all, theoretically it is also an interesting question how the "first-order" picture of fracture changes in the presence of other screening mechanisms for the long-range interactions. The implications of statistical fracture on other lengthscales, as in multi-scale modeling, are then dependent on what is the appropriate coarse-grained description. The resulting picture of the emerging

physics should be connected to what we have presented in this work.

**Acknowledgments:**
MJA would like to thank the Centre of Excellence program of the Academy of Finland and TEKES (The National Technology Agency of Finland) for financial support. A number of students, colleagues, and partners in research (K. Niskanen, V. Räisänen, L. Salminen, E. Seppälä, J. Rosti, J. Lohi) have contributed to the related research. PKVVN is sponsored by the Mathematical, Information and Computational Sciences Division, Office of Advanced Scientific Computing Research, U.S. Department of Energy under contract number DE-AC05-00OR22725 with UT-Battelle, LLC. In addition, PKVVN acknowledges the discussions with and support received from Dr. Srdjan Simunovic. SZ whishes to thank A. Baldassarri, D. Bonamy, A. Hansen, H. J. Herrmann, F. Kun, M. Minozzi, S. Roux, A. Vespignani and M. Zaiser for collaborations, discussions and remarks on the topics discussed in this review.

## Appendix A: Algorithms

As mentioned earlier, fracture of disordered quasi-brittle materials is often studied using discrete lattice networks, wherein the damage is accumulated progressively by breaking one bond at a time until the lattice system falls apart. Each time a bond is broken, it is necessary to redistribute the stresses to determine the subsequent bond failure. Algebraically, this process of simulating fracture by breaking one bond at a time is equivalent to solving a new set of linear equations (Kirchhoff equations in the case of fuse models)

$$\mathbf{A}_n \mathbf{x}_n = \mathbf{b}_n, \qquad n = 0, 1, 2, \ldots, \tag{A1}$$

every time a new lattice bond is broken. In Eq. (A1), each matrix $\mathbf{A}_n$ is an $N \times N$ symmetric and positive definite matrix (the lattice conductance matrix in the case of fuse models and the lattice stiffness matrix in the case of spring and beam models), $\mathbf{b}_n$ is the $N \times 1$ (given) applied nodal current or force vector, $\mathbf{x}_n$ is the $N \times 1$ (unknown) nodal potential or displacement vector, and $N$ is the number of degrees of freedom (unknowns) in the lattice. The subscript $n$ in Eq. (A1) indicates that $\mathbf{A}_n$ and $\mathbf{b}_n$ are evaluated after the $n^{th}$ bond is broken. The solution $\mathbf{x}_n$, obtained after the $n^{th}$ bond is broken, is used in determining the subsequent $((n+1)^{th})$ bond to be broken.

Numerical simulations of fracture using large discrete lattice networks are often hampered due to the high computational cost associated with solving a new large set of linear equations every time a new lattice bond is broken. This becomes especially severe with increasing lattice system size, $L$, as the number of broken bonds at failure, $n_f$, follows a power-law distribution given by

$n_f \sim O(L^{1.8})$ in 2D and $n_f \sim O(L^{2.7})$ in 3D. In addition, since the response of the lattice system corresponds to a specific realization of the random breaking thresholds, an ensemble averaging of numerical results over $N_{config}$ configurations is necessary to obtain a realistic representation of the lattice system response. This further increases the computational time required to perform simulations on large lattice systems.

### A.1 *Fourier Acceleration Method*

Traditionally, iterative techniques based on preconditioned conjugate gradient (PCG) method have been used to simulate fracture using fuse networks (see Ref. [362] for an excellent review of iterative methods; see Ref. [363] for a review of multigrid method). However, large-scale numerical simulations using iterative solvers have often been hindered due to the *critical slowing down* associated with the iterative solvers as the lattice system approaches macroscopic fracture. That is, as the lattice system gets closer to macroscopic fracture, the condition number of the system of linear equations increases, thereby increasing the number of iterations required to attain a fixed accuracy. This becomes particularly significant for large lattices. As a remedy, Fourier accelerated PCG iterative solvers [351,364,365] have been suggested to alleviate the critical slowing down. The Fourier acceleration algorithm proposed in Refs. [364, 365] for solving the system of equations $\mathbf{Ax} = \mathbf{b}$ can be expressed as shown in Algorithm 1. In this subsection, we do not explicitly write the subscript $n$ to refer to the system of equations $\mathbf{A}_n\mathbf{x}_n = \mathbf{b}_n$ obtained after the failure of $n$ bonds. Instead, the subscript $n$ is implicitly understood.

*Algorithm A.1*

1: Compute $\mathbf{r}^{(0)} = \mathbf{b} - \mathbf{Ax}^{(0)}$ for some initial guess $\mathbf{x}^{(0)}$
2: **for** $k = 1, 2, \ldots$ **do**
3: Solve: $\mathbf{Mz}^{(k-1)} = \mathbf{r}^{(k-1)}$
4: $\mathbf{x}^{(k)} = \mathbf{x}^{(k-1)} + \mathbf{z}^{(k-1)}$
5: $\mathbf{r}^{(k)} = \mathbf{r}^{(k-1)} - \mathbf{Az}^{(k-1)}$
6: Check convergence; continue if necessary
7: **end for**

In Algorithm 1, the matrix $\mathbf{M}$ is referred to as the preconditioner, and the superscript in the parenthesis refers to the iteration number. The steps in the Algorithm 1 can be combined into an iterative scheme as shown below

$$\mathbf{x}^{(k+1)} = \mathbf{x}^{(k)} + \mathbf{M}^{-1}\mathbf{r}^{(k)} \tag{A2}$$

where $\mathbf{r}^{(k)} = \mathbf{b} - \mathbf{Ax}^{(k)}$. Denoting the error $\mathbf{e}$ (or *algebraic error*) as $\mathbf{e} = \mathbf{x} - \bar{\mathbf{x}}$, where $\bar{\mathbf{x}}$ is the exact solution such that $\mathbf{A}\bar{\mathbf{x}} = \mathbf{b}$, the errors in the $k^{th}$ and

$(k+1)^{th}$ iterations may be related as

$$\mathbf{e}^{(k+1)} = (\mathbf{I} - \mathbf{M}^{-1}\mathbf{A})\mathbf{e}^{(k)} \tag{A3}$$

Consequently, after $k$ number of relaxation sweeps, the error in the $k^{th}$ approximation is given by $\mathbf{e}^{(k)} = \mathbf{Q}^k\mathbf{e}^{(0)}$, where $\mathbf{Q} = (\mathbf{I} - \mathbf{M}^{-1}\mathbf{A})$. Choosing a particular vector norm and its associated matrix norm, it is possible to bound the error after $k$ iterations by $\|\mathbf{e}^{(k)}\| \leq \|\mathbf{Q}\|^k\|\mathbf{e}^{(0)}\|$. From this relation, it can be shown that the iteration associated with the matrix $\mathbf{Q}$ converges for all initial guesses if and only if $\rho(\mathbf{Q}) < 1$, where $\rho(\mathbf{Q})$ is the spectral radius defined as

$$\rho(\mathbf{Q}) = \max_j|\lambda_j(\mathbf{Q})| \tag{A4}$$

and $\lambda_j(\mathbf{Q})$ denotes the $j^{th}$ eigenvalue of $\mathbf{Q}$ given by $\lambda_j(\mathbf{Q}) = 1 - \lambda_j(\mathbf{M}^{-1}\mathbf{A})$. Hence, convergence of Algorithm 1 is fast whenever the eigenvalues of $\mathbf{M}^{-1}\mathbf{A}$ are clustered around one, i.e., when $\mathbf{M}^{-1}$ is an approximation of the inverse of $\mathbf{A}$.

It should be noted that Eq. (A2) is similar to the iterative algorithm based on the steepest descent (or alternatively, the modified Newton's method or the method of deflected gradients [366]), which is given by

$$\mathbf{x}^{(k+1)} = \mathbf{x}^{(k)} + \alpha^{(k)}\mathbf{M}^{-1}\mathbf{r}^{(k)} \tag{A5}$$

where $\alpha^{(k)}$ is a non-negative scalar chosen to minimize the standard quadratic function $f(\mathbf{x}^{(k+1)})$ defined as

$$f(\mathbf{x}) = \frac{1}{2}\mathbf{x}^T\mathbf{A}\mathbf{x} - \mathbf{b}^T\mathbf{x} \tag{A6}$$

The minimization of $f(\mathbf{x})$ is equivalent to the solution of the system of equations $\mathbf{A}\mathbf{x} = \mathbf{b}$. In this sense, a variety of iterative algorithms such as steepest descent and quasi-Newton methods [366] may be employed to solve $\mathbf{A}\mathbf{x} = \mathbf{b}$ using the iterative scheme based on Eq. (A5). For instance, $\mathbf{M}^{-1} = \mathbf{I}$ results in a steepest descent algorithm, whereas if $\mathbf{M}^{-1}$ is the inverse of the Hessian of $f$ then we obtain the Newton's method. In general, $\mathbf{M}^{-1}$ is chosen to be an approximation to the inverse of the Hessian. In addition, in order to guarantee the iterative process defined by Eq. (A5) to be a descent method for small values of $\alpha^{(k)}$, it is in general required that $\mathbf{M}$ be positive definite [366]. For computational purposes, $\mathbf{M}$ is chosen such that its inverse can be computed cheaply so that the solution of $\mathbf{M}\mathbf{z} = \mathbf{r}$ can be computed with least computational effort.

The Fourier acceleration algorithm proposed in Refs. [364, 365] chooses an ensemble averaged matrix $\bar{\mathbf{A}}$ [367, 368] as the preconditioner in Algorithm 1, where $\bar{\mathbf{A}}(i,j) = r^{(d_w - d_f)}$, $r = |i-j|$, the distance between the nodes $i$ and $j$, and $d_f$ and $d_w$ refer to the fractal dimension of the current-carrying backbone and the random-walk dimension respectively. This ensemble averaged matrix $\bar{\mathbf{A}}$ is a symmetric Toeplitz matrix and hence the preconditioned system $\mathbf{Mz} = \mathbf{r}$ in Algorithm 1 can be solved in $O(N\ log\ N)$ operations by using FFTs of size $N$. Compared with the unconditioned CG methods, the Fourier accelerated technique based on ensemble averaged circulant preconditioner significantly reduced the computational time required to simulate fracture using random fuse networks [364, 365]. Although the Fourier accelerating technique significantly improves the condition number of the unconditioned system of equations, these methods still exhibit *critical slowing down* close to macroscopic fracture. Consequently, the numerical simulations in the past were often limited to systems of sizes $L = 128$.

Mathematically, the ensemble averaged matrix $\bar{\mathbf{A}}$ is not the optimal circulant preconditioner in the sense that it does not minimize the norm $\|\mathbf{I} - \mathbf{C}^{-1}\mathbf{A}\|_F$ over all non-singular circulant matrices $\mathbf{C}$, and hence is expected to take more CG iterations than the *optimal* [369–372] and *superoptimal* [372, 373] circulant preconditioners. In the above description, $\|\cdot\|_F$ denotes the Frobenius norm [374]. It should be noted that $\|\mathbf{I} - \mathbf{C}^{-1}\mathbf{A}\|_F$ determines the convergence rate of Algorithm 1 as evident in Eq. (A3). The discussion of *optimal* [369–372] and *superoptimal* [372, 373] circulant preconditioners is presented in detail in Section A.4. In addition, the Fourier acceleration technique is not effective when fracture simulation is performed using central-force and bond-bending lattice models [365]. In the case of central-force and bond-bending lattice models, each of the lattice sites has more than one degree of freedom. This results in a matrix $\mathbf{A}_0$ that is block-circulant. This explains why a naive circulant preconditioner is not effective in the case of central-force and bond-bending lattice models. A discussion on block-circulant preconditioners is presented in Section A.4.

### A.2 *Naive Application of Sparse Direct Solvers*

Alternatively, since each of the matrices $\mathbf{A}_n$ for $n = 0, 1, 2, \ldots$, is sparse, it is possible to use any of the existing sparse direct solvers [375, 376] to solve each of the system of equations formed by $\mathbf{A}_n$. It should be noted that the Cholesky factorization of $\mathbf{A}_n$ for any particular $n$ can be done efficiently. However, factorization of each of the $\mathbf{A}_n$ matrices for $n_f \sim O(L^{1.8})$ (or $n_f \sim O(L^{2.7})$ in 3D) number of times is still a computationally daunting task. For example, in the case of a 2D triangular lattice system of size $L = 128$, the algorithm based on factorizing each of the $\mathbf{A}_n$ matrices using supernodal sparse direct

solver [377] took on an average 8300 seconds compared to an average of 7473 seconds taken by the *optimal* circulant preconditioner based CG algorithm. It should however be noted that, in general, the *optimal* circulant preconditioner based CG algorithm used in the above comparison is much faster than the Fourier accelerated CG algorithm described in Ref. [365]. However, as the following description elaborates, the computational advantages of sparse direct solvers are not fully realized when the algorithm is based on factorizing each of the $\mathbf{A}_n$ matrices.

### A.3 *Multiple-rank sparse Cholesky downdating algorithm*

An important feature of fracture simulations using discrete lattice models is that, for each $n = 0, 1, 2, \ldots$, the new matrix $\mathbf{A}_{n+1}$ of the lattice system after the $(n+1)^{th}$ broken bond is equivalent to a rank-$p$ downdate of the matrix $\mathbf{A}_n$ [187, 378]. Mathematically, in the case of the fuse and spring models, the breaking of a bond is equivalent to a rank-one downdate of the matrix $\mathbf{A}_n$, whereas in the case of beam models, it is equivalent to multiple-rank (rank-3 for 2D, and rank-6 for 3D) downdate of the matrix $\mathbf{A}_n$. Thus, an updating scheme of some kind is therefore likely to be more efficient than solving the new set of equations formed by Eq. (A1) for each $n$. One possibility is to use the Shermon-Morrison-Woodbury formula [374] to update the solution vector $\mathbf{x}_{n+1}$ directly knowing the sparse Cholesky factor $\mathbf{L}_m$ of $\mathbf{A}_m$, for any $m \leq n$. That is, given the Cholesky factorization $\mathbf{L}_m$ of $\mathbf{A}_m$ for $m = 0, 1, 2, \cdots$, it is possible to obtain a direct updating of the solution $\mathbf{x}_{n+1}$ for $n = m, m+1, m+2, \cdots$ based on $p = (n-m)$ *saxpy* vector updates [187,378]. The resulting algorithm is equivalent to a dense matrix update algorithm proposed in the Appendix C of Ref. [187]. In Ref. [187], it has been shown that for two-dimensional fracture simulations, any of these sparse solver updating algorithms are significantly superior to the traditional Fourier accelerated CG iterative schemes. The best performing sparse solver for two-dimensional fracture simulations using the discrete lattice models (fuse, spring and beam models) is based on the multiple-rank sparse Cholesky downdating algorithm, which is briefly described in the following.

Consider the Cholesky factorizations

$$\mathbf{P}\mathbf{A}_n\mathbf{P}^t = \mathbf{L}_n\mathbf{L}_n^t \tag{A7}$$

for each $n = 0, 1, 2, \cdots$, where $\mathbf{P}$ is a permutation matrix chosen to preserve the sparsity of $\mathbf{L}_n$. Since the breaking of bonds is equivalent to removing the edges in the underlying graph structure of the matrix $\mathbf{A}_n$, for each $n$, the sparsity pattern of the Cholesky factorization $\mathbf{L}_{n+1}$ of the matrix $\mathbf{A}_{n+1}$ must be a subset of the sparsity pattern of the Cholesky factorization $\mathbf{L}_n$ of the

matrix $\mathbf{A}_n$. Hence, for all $n$, the sparsity pattern of $\mathbf{L}_n$ is contained in that of $\mathbf{L}_0$. That is, denoting the sparsity pattern of $\mathbf{L}$ by $\mathcal{L}$, we have

$$\mathcal{L}_m \supseteq \mathcal{L}_n \quad \forall\ m < n \tag{A8}$$

Therefore, we can use the sparse Cholesky factorization downdate algorithm of Davis and Hager [379, 380] to successively downdate the Cholesky factorizations $\mathbf{L}_n$ of $\mathbf{A}_n$ to $\mathbf{L}_{n+1}$ of $\mathbf{A}_{n+1}$, i.e., $\mathbf{L}_n \rightarrow \mathbf{L}_{n+1}$ for $n = 0, 1, 2, \cdots$. Since $\mathcal{L}_n \supseteq \mathcal{L}_{n+1}$, it is necessary to modify only a part of the non-zero entries of $\mathbf{L}_n$ in order to obtain $\mathbf{L}_n \rightarrow \mathbf{L}_{n+1}$. This results in a significant reduction in the computational time. In addition, the rank-$p$ downdating vectors are very sparse with only a few non-zero entries (at most two for fuse models; six for spring models; and twelve for beam models). Consequently, the computational effort involved in downdating the Cholesky factors using the sparse downdating vectors is once again significantly reduced [187, 378].

### A.4 *Optimal* ***and*** *superoptimal* ***circulant preconditioners***

Although the algorithms based on sparse direct solvers with multiple-rank Cholesky downdating schemes achieve superior performance over iterative solvers in 2D lattice simulations (see Section A.7), the memory demands brought about by the amount of fill-in during sparse Cholesky factorization poses a severe constraint over the usage of sparse direct solvers for 3D lattice simulations. Hence, iterative solvers are in common use for large-scale 3D lattice simulations. The performance of iterative solvers depends crucially on the condition number and clustering of the eigenvalues of the preconditioned system. In general, the more clustered the eigenvalues are, the faster the convergence rate is. Hence, the main focus of any iterative solution technique is choosing an optimum preconditioner.

The main observation behind developing preconditioners for the iterative schemes is that the operators on discrete lattice network result in a circulant block structure. For example, the Laplacian operator (Kirchhoff equations in the case of random fuse model) on the initial uniform grid results in a Toeplitz matrix $\mathbf{A}_0$. Hence, a fast Poisson type solver with a circulant preconditioner can be used to obtain the solution in $O(N\ logN)$ operations using FFTs of size $N$, where $N$ denotes the number of degrees of freedom. However, as the lattice bonds are broken successively, the initial uniform lattice grid becomes a diluted network. Consequently, although the matrix $\mathbf{A}_0$ is Toeplitz (also block Toeplitz with Toeplitz blocks) initially, the subsequent matrices $\mathbf{A}_n$, for each $n$, are not Toeplitz matrices. However, depending on the pattern of broken bonds, $\mathbf{A}_n$ may still possess block structure with many of the blocks being Toeplitz blocks.

The *optimal* circulant preconditioner $c(\mathbf{A})$ [369–372] of a matrix $\mathbf{A}$ is defined as the minimizer of $\|\mathbf{C}-\mathbf{A}\|_F$ over all $N \times N$ circulant matrices $\mathbf{C}$. Given a matrix $\mathbf{A}$, the *optimal* circulant preconditioner $c(\mathbf{A})$ is uniquely determined by

$$c(\mathbf{A}) = \mathbf{F}^* \delta\left(\mathbf{F}\mathbf{A}\mathbf{F}^*\right)\mathbf{F} \tag{A9}$$

where $\mathbf{F}$ denotes the discrete Fourier matrix, $\delta\left(\mathbf{A}\right)$ denotes the diagonal matrix whose diagonal is equal to the diagonal of the matrix $\mathbf{A}$, and $*$ denotes the adjoint (i.e. conjugate transpose). It should be noted that the diagonals of $\mathbf{F}\mathbf{A}\mathbf{F}^*$ represent the eigenvalues of the matrix $c(\mathbf{A})$ and can be obtained in $O(N\ log\ N)$ operations by taking the FFT of the first column of $c(\mathbf{A})$. The first column vector of T. Chan's *optimal* circulant preconditioner matrix that minimizes the norm $\|\mathbf{C}-\mathbf{A}\|_F$ is given by

$$c_i = \frac{1}{N}\sum_{j=1}^{N} a_{j,(j-i+1) \bmod N} \tag{A10}$$

If the matrix $\mathbf{A}$ is Hermitian, the eigenvalues of $c(\mathbf{A})$ are bounded below and above by

$$\lambda_{min}(\mathbf{A}) \leq \lambda_{min}(c(\mathbf{A})) \leq \lambda_{max}(c(\mathbf{A})) \leq \lambda_{max}(\mathbf{A}) \tag{A11}$$

where $\lambda_{min}(\cdot)$ and $\lambda_{max}(\cdot)$ denote the minimum and maximum eigenvalues, respectively. Based on the above result, if $\mathbf{A}$ is positive definite, then the circulant preconditioner $c(\mathbf{A})$ is also positive definite. The computational cost associated with the solution of the preconditioned system $c(\mathbf{A})\mathbf{z} = \mathbf{r}$ is the initialization cost of $nnz(\mathbf{A})$ for setting the first column of $c(\mathbf{A})$ using Eq. (A10) during the first iteration, and $O(N\ log\ N)$ during every iteration step.

The *superoptimal* circulant preconditioner $t(\mathbf{A})$ [373] is based on the idea of minimizing the norm $\|\mathbf{I}-\mathbf{C}^{-1}\mathbf{A}\|_F$ over all nonsingular circulant matrices $\mathbf{C}$. In the above description, $t(\mathbf{A})$ is *superoptimal* in the sense that it minimizes $\|\mathbf{I}-\mathbf{C}^{-1}\mathbf{A}\|_F$, and is equal to

$$t(\mathbf{A}) = c(\mathbf{A}\mathbf{A}^*)c(\mathbf{A})^{-1} \tag{A12}$$

The preconditioner obtained by Eq. (A12) is also positive definite if $\mathbf{A}$ itself is positive definite. Although the preconditioner $t(\mathbf{A})$ is obtained by minimizing the norm $\|\mathbf{I}-\mathbf{C}^{-1}\mathbf{A}\|_F$, the asymptotic convergence of the preconditioned system is same as $c(\mathbf{A})$ for large $N$ system.

### A.5 *Block-circulant preconditioner*

Alternatively, block-circulant preconditioners may also be used as preconditioners since many of the block matrices in $\mathbf{A}_n$ for $n > 0$ may still retain the circulant or Toeplitz property. Let the matrix $\mathbf{A}_n$ be partitioned into $r$-by-$r$ blocks such that each block is an $s$-by-$s$ matrix. That is, $N = rs$. Since each of the blocks of $\mathbf{A}_n$ are Toeplitz (or even circulant), the block-circulant preconditioner is obtained by using circulant approximations for each of the blocks of $\mathbf{A}_n$. It is the minimizer of $\|\mathbf{C} - \mathbf{A}_n\|_F$ over all matrices $\mathbf{C}$ that are $r$-by-$r$ block matrices with $s$-by-$s$ circulant blocks. In addition, we have

$$\lambda_{min}(\mathbf{A}_n) \leq \lambda_{min}(c_B(\mathbf{A}_n)) \leq \lambda_{max}(c_B(\mathbf{A}_n)) \leq \lambda_{max}(\mathbf{A}_n) \tag{A13}$$

In particular, if $\mathbf{A}_n$ is positive definite, then the block-preconditioner $c_B(\mathbf{A}_n)$ is also positive definite. In general, the average computational cost of using the block-circulant preconditioner per iteration is $O(rs\ log\ s) + delops$, where *delops* represents the operational cost associated with solving a block-diagonal matrix with $r \times r$ dense blocks. For 2D and 3D discrete lattice network with periodic boundary conditions in the horizontal direction, this operational cost reduces significantly. The reader is referred to [187, 381] for further details on *optimal* and block-circulant preconditioners for discrete lattice networks.

### A.6 *Summary of algorithms*

To summarize, we use the following two algorithms based on sparse direct solvers for modeling fracture using discrete lattice systems.

- *Solver Type A*: Given the factorization $\mathbf{L}_m$ of $\mathbf{A}_m$, the rank-1 sparse Cholesky modification is used to update the factorization $\mathbf{L}_{n+1}$ for all subsequent values of $n = m, m+1, \cdots$. Once the factorization $\mathbf{L}_{n+1}$ of $\mathbf{A}_{n+1}$ is obtained, the solution vector $\mathbf{x}_{n+1}$ is obtained from $\mathbf{L}_{n+1}\mathbf{L}_{n+1}^t\mathbf{x}_{n+1} = \mathbf{b}_{n+1}$ by two triangular solves [187, 378].
- *Solver Type B*: Assuming that the factor $\mathbf{L}_m$ of matrix $\mathbf{A}_m$ is available after the $m^{th}$ fuse is burnt, the solution $\mathbf{x}_{n+1}$ after the $(n+1)^{th}$ fuse is burnt, for $n = m, m+1, \cdots, m+maxupd$, is obtained through $p = (n-m)$ *saxpy* vector updates using an algorithm based on Shermon-Morrison-Woodbury [374] formula. Either a completely new factorization of the matrix $\mathbf{A}$ is performed or a multiple-rank downdate of the factorization $\mathbf{L}_m \rightarrow \mathbf{L}_{m+maxupd+1}$ is performed every *maxupd* steps [187, 378].

In addition to the above two algorithms, the simulations are carried out using the iterative solvers based on *optimal* circulant and block-circulant preconditioners [187, 381].

### A.7 *Performance comparison*

For two-dimensional lattice systems, we choose a triangular lattice topology, whereas a cubic lattice topology is used in three-dimensional cases. The random thresholds fuse model (rank-one downdate with $p = 1$) is used as a basis of performance comparison to evaluate the numerical efficiency of various algorithms. The algorithmic framework for central-force (spring) and beam models is presented in Refs. [187, 378].

In the numerical simulations using solver types A and B based on sparse direct solvers, the maximum number of vector updates, *maxupd*, is chosen to be a constant for a given lattice size $L$. We choose $maxupd = 25$ for $L = \{4, 8, 16, 24, 32\}$, $maxupd = 50$ for $L = 64$, and $maxupd = 100$ for $L = \{128, 256, 512\}$. For $L = 512$, *maxupd* is limited to 100 due to memory constraints. By keeping the *maxupd* value constant, it is possible to compare realistically the computational cost associated with different solver types. Moreover, the relative CPU times taken by these algorithms remain the same even when the simulations are performed on different platforms.

The convergence rate of an iterative solver depends on the quality of starting vector. When PCG iterative solvers are used in updating the solution $\mathbf{x}_n \rightarrow \mathbf{x}_{n+1}$, we use either the solution from the previous converged state, i.e., $\mathbf{x}_n$, or the zero vector, $\mathbf{0}$, as the starting vectors for the CG iteration of $\mathbf{x}_{n+1}$. The choice of using either $\mathbf{x}_n$ or $\mathbf{0}$ as the starting vectors depends on which vector is closer to $\mathbf{b}_{n+1}$ in 2-norm. That is, if $\|\mathbf{b}_{n+1} - \mathbf{A}_n\mathbf{x}_n\|_2 \leq \|\mathbf{b}_{n+1}\|_2$, then $\mathbf{x}_n$ is used, else $\mathbf{0}$ is used as the starting vector for the $\mathbf{x}_{n+1}$ CG iteration. A relative residual tolerance $\epsilon = 10^{-12}$ is used in CG iteration.

The numerical simulations are carried out on a single 1.3 GHz IBM Power4 processor. Tables A1 and A2 present the CPU times taken for one configuration (simulation) using the sparse direct solver algorithms A and B, respectively. These tables also indicate the number of configurations, $N_{config}$, over which ensemble averaging of the numerical results is performed for performance evaluation. The CPU times taken by the iterative solvers are presented in Tables A3-A4. For iterative solvers, the number of iterations presented in Tables A3-A4 denote the average number of total iterations taken to break one intact lattice configuration until it falls apart. In the case of iterative solvers, some of the simulations for larger lattice systems were not performed either because they were expected to take larger CPU times or the numerical results do not influence the conclusions drawn in this study. The results presented in Tables A1-A4 indicate that for 2D lattice systems, the multiple-rank Cholesky downdate based sparse direct solver algorithms are clearly superior to the optimal and block-circulant preconditioned CG iterative solvers. In particular, for the lattice size $L = 128$, the solver type A took 212.2 seconds, which should be compared with the 7473 and 8300 seconds taken respectively by the optimal

Table A1. Solver Type A (2D Triangular Lattice)

| Size | CPU(sec) | Simulations |
|---|---|---|
| 32 | 0.592 | 20000 |
| 64 | 10.72 | 4000 |
| 128 | 212.2 | 800 |
| 256 | 5647 | 96 |
| 512 | 93779 | 16 |

Table A2. Solver Type B (2D Triangular Lattice)

| Size | CPU(sec) | Simulations |
|---|---|---|
| 32 | 0.543 | 20000 |
| 64 | 11.15 | 4000 |
| 128 | 211.5 | 800 |
| 256 | 6413 | 96 |

Table A3. Block Circulant PCG (2D Triangular Lattice)

| Size | CPU(sec) | Iter | Simulations |
|---|---|---|---|
| 32 | 10.00 | 11597 | 20000 |
| 64 | 135.9 | 41207 | 1600 |
| 128 | 2818 | 147510 | 192 |
| 256 | 94717 | | 32 |

Table A4. Optimal Circulant PCG (2D Triangular Lattice)

| Size | CPU(sec) | Iter | Simulations |
|---|---|---|---|
| 32 | 11.66 | 25469 | 20000 |
| 64 | 173.6 | 120570 | 1600 |
| 128 | 7473 | 622140 | 128 |

circulant preconditioner and the naive sparse direct solution technique based on factorizing each of the $\mathbf{A}_n$ matrices.

For large 3D lattice systems, the advantages exhibited by the multiple-rank Cholesky downdating algorithms in 2D simulations vanish due to the amount of *fill-in* during Cholesky factorization. Tables A5-A8 present the CPU times taken for simulating one-configuration using the block circulant, *optimal* circulant, un-preconditioned, and the incomplete Cholesky iterative solvers, respectively. It should be noted that for large 3D lattice systems (e.g., $L = 32$), the performance of incomplete Cholesky preconditioner (see Table A8) is sim-

Table A5. Block Circulant PCG (3D Cubic Lattice)

| Size | CPU(sec) | Iter | Simulations |
|---|---|---|---|
| 10 | 16.54 | 16168 | 40000 |
| 16 | 304.6 | 58756 | 1920 |
| 24 | 2154 | 180204 | 256 |
| 32 | 12716 | 403459 | 128 |
| 48 | 130522 | 1253331 | 32 |
| 64 | 1180230 | | 11 |

Table A6. Optimal Circulant PCG (3D Cubic Lattice)

| Size | CPU(sec) | Iter | Simulations |
|---|---|---|---|
| 10 | 15.71 | 27799 | 40000 |
| 16 | 386.6 | 121431 | 1920 |
| 24 | 2488 | 446831 | 256 |
| 32 | 20127 | 1142861 | 32 |
| 48 | 233887 | 4335720 | 32 |

Table A7. Un-preconditioned CG (3D Cubic Lattice)

| Size | CPU(sec) | Iter | Simulations |
|---|---|---|---|
| 10 | 5.962 | 48417 | 40000 |
| 16 | 119.4 | 246072 | 3840 |
| 24 | 1923 | 1030158 | 256 |
| 32 | 16008 | 2868193 | 64 |

Table A8. Incomplete Cholesky PCG (3D Cubic Lattice)

| Size | CPU(sec) | Iter | Simulations |
|---|---|---|---|
| 10 | 5.027 | 8236 | 40000 |
| 16 | 118.1 | 42517 | 3840 |
| 24 | 1659 | 152800 | 512 |
| 32 | 12091 | 422113 | 64 |

ilar to that of block-circulant preconditioner (see Table A5), even though the performance of incomplete Cholesky preconditioner is far more superior in the case of 2D lattice simulations [187]. Indeed, for 3D lattice systems of sizes $L = 48$ and $L = 64$, the CPU time taken by the sparse direct solver types A and B is much higher than that of block-circulant PCG solver.

To summarize, the numerical simulation results presented in Tables A1-A4

for 2D triangular random fuse networks indicate that sparse direct solvers based on multiple-rank sparse Cholesky downdating are superior to the competing iterative schemes using block-circulant and optimal circulant preconditioners. On the other hand, for 3D lattice systems, the block-circulant preconditioner based CG solver exhibits superior performance (for system sizes $L > 32$) over the sparse direct solvers and the related incomplete Cholesky preconditioned CG solvers. In addition, for both 2D and 3D lattice systems, the block circulant preconditioned CG is superior to the *optimal* circulant preconditioned PCG solver, which in turn is superior to the Fourier accelerated PCG solvers used in Refs. [364, 365].

## References


[1] L. da Vinci, in *I libri di Meccanica*, edited by A. Uccelli ( Hoepli Milano 1940).
[2] G. Galilei, *Discorsi e dimostrazioni matematiche intorno a due nuove scienze* ( Boringhieri, Torino, 1958).
[3] W. B. Parsons, *Engineers and Engineering in the Renaissance* ( MIT Press, Cambridge, 1939).
[4] J. R. Lund and J. P. Byrne, Civil. Eng. and Env. Syst **18**, 243 (2001).
[5] A. A. Griffith, Trans. Roy. Soc. (london) A **221**, 163 (1920).
[6] W. Weibull, in *A statistical theory of the strength of materials*, edited by G. litografiska anstalts förlag ( Stockholm, 1939).
[7] S. P. Timoshenko, in *History of strength of materials*, edited by M. G. Hill ( Mc Graw Hill New York, 1953).
[8] H. J. Herrmann and S. Roux, *Statistical Models for the Fracture of Disordered Media* (North-Holland, Amsterdam, 1990).
[9] B. K. Chakrabarti and L. G. Benguigui, *Statistical Physics of Fracture and Breakdown in Disordered Systems* (Oxford Science Publications, Oxford, 1997).
[10] A. Hansen and S. Roux, in *Statistical toolbox for damage and fracture*, edited by D. Krajcinovic and J. van Mier (Springer-Verlag, New York, 2000), pp. 17–101.
[11] J. L. L. Mishnaevsky, Eng. Fract. Mech. **56**, 47 (1997).
[12] L. de Arcangelis, S. Redner, and H. J. Herrmann, Journal of Physics (Paris) Letters **46**, 585 (1985).
[13] F. T. Pierce, J. Textile Inst. **17**, 355 (1926).
[14] H. E. Daniels, Proc. R. Soc. London A **183**, 405 (1945).
[15] D. Krajcinovic and J. G. M. van Mier, *Damage and fracture of disordered materials* ( Springer-Verlag, New York, 2000).
[16] J. G. M. van Mier, *Fracture Processes of Concrete* (CRC Press, Boca Raton, USA, 1996).
[17] Z. P. Bazant and J. Planas, *Fracture and Size Effect in Concrete and Other Quasibrittle Materials* (CRC Press, Boca Raton, USA, 1997).
[18] J. G. M. van Mier and M. R. A. van Vliet, Eng. Fract. Mech. **70**, 2281 (2003).
[19] G. Lilliu and J. G. M. van Mier, Eng. Fract. Mech. **70**, 927 (2003).
[20] E. Schlangen and E. J. Garboczi, Int. J. Eng. Sci. **34**, 1131 (1996).
[21] L. Niemeyer, L. Pietronero, and H. J. Wiesmann, Phys. Rev. Lett. **52**, 1033 (1984).
[22] P. D. Beale and P. M. Duxbury, Phys. Rev. B **37**, 2785 (1988).
[23] P. F. Arndt and T. Nattermann, Phys. Rev. B **63**, 134204 (2001).
[24] J. Lemaitre and J. L. Chaboche, *Mechanics of Solid Materials* (Cambridge University Press, Cambridge, 1990).
[25] D. Krajcinovic, *Damage Mechanics* (Elsevier, Amsterdam, 1996).
[26] S. Gluzman and D. Sornette, Phys. Rev. E **63**, 066129 (2001).
[27] R. Shcherbakov and D. L. Turcotte, Theoretical and Applied Fracture Mechanics **39**, 245 (2003).
[28] B. K. Atkinson and P. G. Meredith, in *Fracture Mechanics of Rock*, edited by B. Atkinson ( Academic Press, New York, 1987), p. 110.
[29] S. Straumsnes, P. Dommersnes, E. G. Flekkoy, and S. Roux, European Journal of Mechanics A-Solids **16**, 993 (1997).

[30] G. I. Barenblatt, *Scaling, Self-Similarity, and Intermediate Asymptotics* (Cambridge Univ. Press, Cambridge, 1996).
[31] F. Family and T. Viscek, *Dynamics of Fractal Surfaces* ( World Scientific, Singapore, 1991).
[32] A.-L. Barabási and H. E. Stanley, *Fractal concepts in surface growth* (Cambridge University Press, Cambrdige, 1995).
[33] J. M. Lopez, M. A. Rodriguez, and R. Cuerno, Phys. Rev. E **56**, 3993 (1997).
[34] J. M. Lopez, Phys. Rev. Lett. **83**, 4594 (1999).
[35] T. Nattermann, S. Stepanow, L. H. Tang, and H. Leschhorn, J. Phys. (France) II **2**, 1483 (1992).
[36] H. Leschhorn, T. Nattermann, S. Stepanow, and L. H. Tang, Ann. Physik **7**, 1 (1997).
[37] O. Narayan and D. Fisher, Phys. Rev. B **48**, 7030 (1993).
[38] P. Chauve, P. L. Doussal, and K. Wiese, Phys. Rev. Lett. **86**, 1785 (2001).
[39] P. L. Doussal, K. Wiese, and P. Chauve, Phys. Rev. B **66**, 174201 (2002).
[40] F. M. Borodich, J. Mech. Phys. Solids **45**, 239 (1997).
[41] D. Vandembroucq and S. Roux, J. Mech. Phys. Solids **45**, 853 (1997).
[42] D. Vandembroucq and S. Roux, Phys. Rev. E **55**, 6186 (1997).
[43] F. Barra, H. G. E. Hentschel, A. Levermann, and I. Procaccia, Phys. Rev. E **65**, 045101 (2002).
[44] F. Barra, A. Levermann, and I. Procaccia, Phys. Rev. E **66**, 066122 (2002).
[45] A. Levermann and I. Procaccia, Phys. Rev. Lett. **89**, 234501 (2002).
[46] S. Morel, J. Schmittbuhl, E. Bouchaud, and G. Valentin, Phys. Rev. Lett. **85**, 1678 (2000).
[47] S. Morel, E. Bouchaud, and G. Valentin, Phys. Rev. B **65**, 104101 (2002).
[48] E. Bouchaud and J.-P. Bouchaud, Phys. Rev. B **50**, 17752 (1994).
[49] J. Weiss, Int. J. Fracture **109**, 365 (2001).
[50] B. Chiaia, J. G. M. van Mier, and A. Vervuurt, Cem. Concr. Res. **28**, 103 (1998).
[51] I. C. van den Born, A. Santen, H. D. Hoekstra, and J. T. M. D. Hosson, Phys. Rev. B **43**, R3794 (1991).
[52] Z. P. Bazant, Arch. Appl. Mech. **69**, 703 (1999).
[53] L. Sutherland, R. Shenoi, and S. Lewis, Composite Sci. Techn. **209**, 1999 (1999).
[54] M. Korteoja, L. I. Salminen, K. J. Niskanen, and M. J. Alava, J. Pulp Paper Sci. **24**, 1 (1998).
[55] M. Korteoja, L. I. Salminen, K. J. Niskanen, and M. J. Alava, Materials Science and Engineering A **240**, 173 (1999).
[56] M. R. A. van Vliet and J. G. M. van Mier, Eng. Fract. Mech. **65**, 165 (2000).
[57] C. Lu, R. Danzer, and F. D. Fischer, Phys. Rev. E **65**, 067102 (2002).
[58] R. H. Doremus, J. Appl. Phys. **54**, 193 (1983).
[59] J. A. Lavoie, C. Soutis, and J. Morton, Composite Sci. Techn. **60**, 283 (2000).
[60] R. M. L. Foote, Y. W. Mai, and B. Cotterell, J. Mech. Phys. Solids **34**, 593 (1986).
[61] B. Cotterell and Y. W. Mai, J. Mat. Sci. **22**, 2734 (1987).
[62] Y. W. Mai and B. R. Lawn, J. Am. Ceram. Soc. **70**, 289 (1987).
[63] M. R. Wisnom, Composites **22**, 47 (1991).
[64] X. Z. Hu and F. Wittmann, Mat. Struct. **25**, 319 (1992).
[65] V. C. Li, Z. Lin, and T. Matsumoto, Int. J. Solids Structures **1998**, 35 (1998).
[66] A. Tabiei and J. M. Sun, Compos. Struct. **46**, 209 (1999).
[67] M. R. Wisnom, Composite Sci. Techn. **59**, 1937 (1999).
[68] X. Z. Hu and F. Wittmann, Eng. Fract. Mech. **65**, 209 (2000).
[69] Y. W. Mai, Eng. Fract. Mech. **69**, 219 (2002).
[70] X. Z. Hu, Eng. Fract. Mech. **69**, 555 (2002).
[71] M. M. Stevanovic, A. A. Elhisnavi, and D. R. Pesikan, Mat. Sci. Forum **413**, 207 (2003).
[72] K. Duan, X. Z. Hu, and F. H. Wittmann, Mat. Struct. **36**, 74 (2003).
[73] Z. P. Bazant, Probabilistic Engineering Mechanics **19**, 307 (2004).
[74] Z. P. Bazant, PNAS **101**, 13400 (2004).
[75] W. Klock and S. Aicher, Wood Fib. Sci. **37**, 403 (2005).
[76] J. Rosti *et al.*, Eur. Phys. J. B **19**, 259 (2001).
[77] E. Bouchaud, Journal of Physics: Condensed Matter **9**, 4319 (1997).
[78] L. I. Salminen, M. J. Alava, and K. J. Niskanen, Eur. Phys. J. B **32**, 369 (2003).
[79] J. Kertész, V. K. Horvath, and F. Weber, Fractals **1**, 67 (1993).
[80] T. Engoy, K. J. Maloy, A. Hansen, and S. Roux, Phys. Rev. Lett. **73**, 834 (1994).
[81] I. L. Menezes-Sobrinho, M. S. Couto, and I. R. B. Ribeiro, Phys. Rev. E **71**, 066121 (2005).
[82] E. Bouchbinder, I. Procaccia, and S. Sela, cond-mat/0508549 (2005).
[83] J. Schmittbuhl and K. J. Maloy, Phys. Rev. Lett. **78**, 3888 (1997).
[84] A. Delaplace, J. Schmittbuhl, and K. J. Maloy, Phys. Rev. E **60**, 1337 (1999).
[85] K. J. Maloy and J. Schmittbuhl, Phys. Rev. Lett. **87**, 105502 (2001).

[86] K. J. Maloy, J. Schmittbuhl, A. Hansen, and G. G. Batrouni, Int. J. Fracture **121**, 9 (2003).
[87] K. J. Maloy, S. Santucci, J. Schmittbuhl, and R. Toussaint, Phys. Rev. Lett. **96**, 045501 (2006).
[88] B. B. Mandelbrot, D. E. Passoja, and A. J. Paullay, Nature **308**, 721 (1984).
[89] L. Ponson, D. Bonamy, and E. Bouchaud, Phys. Rev. Lett. **96**, 035506 (2006).
[90] J. M. Boffa, C. Allain, and J. Hulin, Eur. Phys. J. AP **2**, 281 (1998).
[91] P. Daguier, B. Nghiem, E. Bouchaud, and F. Creuzet, Phys. Rev. Lett. **78**, 1062 (1997).
[92] D. Bonamy *et al.*, preprint (2006).
[93] S. Morel, T. Lubet, J.-L. Pouchou, and J.-M. Olive, Phys. Rev. Lett. **93**, 065504 (2004).
[94] F. Plouraboue *et al.*, Phys. Rev. E **53**, 277 (1996).
[95] F. Célarié *et al.*, Phys. Rev. Lett. **90**, 075504 (2003).
[96] C. Marliére *et al.*, Journal of Physics: Condensed Matter **15**, S2377 (2003).
[97] J. P. Bouchaud, E. Bouchaud, G. Lapasset, and J. Planès, Phys. Rev. Lett. **71**, 2240 (1993).
[98] J. M. Lopez and J. Schmittubhl, Phys. Rev. E **57**, 6405 (1998).
[99] S. Morel, J. Schmittbuhl, J. M. Lopez, and G. Valentin, Phys. Rev. E **58**, 6999 (1998).
[100] G. Mourot, S. Morel, E. Bouchaud, and G. Valentin, Phys. Rev. E **71**, 016136 (2005).
[101] E. Bouchbinder, I. Procaccia, S. Santucci, and L. Vanel, cond-mat/0508183 (2005).
[102] D. Hull, *Fractography: Observing, Measuring and Interpreting Fracture Surface Topography* (Cambridge University Press, Cambrdige, 1999).
[103] M. Kouzeli, L. Weber, S. C. March, and A. Mortensen, Acta Materialia **49**, 497 (2001).
[104] H. Kawakata *et al.*, Tectonophysics **313**, 293 (1999).
[105] D. A. Lockner, Int. J. Rock Mech. Min. Sci. **30**, 883 (1993).
[106] B. Berkowitz and A. Hadad, Journal of Geophysical Research B: Solid Earth **102**, 12205 (1997).
[107] E. Bonnet *et al.*, Rev. Geophys. **39**, 347 (2001).
[108] J. Rundle, W. Klein, and S. Gross, Pure Appl. Geophys. **155**, 575 (1999).
[109] V. Lyakhovsky, Geophys. J. Int. **144**, 114 (2001).
[110] K. Goto and K. Otsuki, Geophys. Res. Lett. **31**, L05601 (2004).
[111] J. Weiss, Bull. Seism. Soc. Am. **87**, 1362 (1997).
[112] M. V. Lysak, Eng. Fract. Mech. **55**, 443 (1996).
[113] C. S. Ouyang, E. Landis, and S. P. Shah, J. Engng. Mech. - ASCE **117**, 2681 (1991).
[114] B. Harris, F. Habib, and R. Cooke, Proc. R. Soc. London A **437**, 1899 (1992).
[115] P. M. Mummery, B. Derby, and C. B. Scruby, Acta Metall. Mater. **41**, 1431 (1993).
[116] S. Barre and M. L. Benzeggagh, Composite Sci. Techn. **52**, 369 (1994).
[117] P. J. de Groot, P. A. M. Wijnen, and R. B. F. Janssen, Composite Sci. Techn. **55**, 405 (1995).
[118] J. Bohse, Composite Sci. Techn. **60**, 1213 (2000).
[119] Y. A. Dzenis and I. Saunders, Int. J. Fracture **117**, L23 (2002).
[120] A. Petri *et al.*, Phys. Rev. Lett. **73**, 3423 (1994).
[121] A. Garcimartin, A. Guarino, L. Bellon, and S. Ciliberto, Phys. Rev. Lett. **79**, 3202 (1997).
[122] A. Guarino, A. Garcimartin, and S. Ciliberto, Eur. Phys. J. B **6**, 13 (1998).
[123] C. Maes, A. van Moffaert, H. Frederix, and H. Strauven, Phys. Rev. B **57**, 4987 (1998).
[124] A. Guarino *et al.*, Eur. Phys. J. B **26**, 141 (2002).
[125] L. I. Salminen, A. I. Tolvanen, and M. J. Alava, Phys. Rev. Lett. **89**, 185503 (2002).
[126] L. I. Salminen *et al.*, Europhys. Lett. **73**, 55 (2006).
[127] D. Amitrano, Journal of Geophysical Research B: Solid Earth **108**, 2044 (2003).
[128] I. G. Main, Geophys. J. Int. **107**, 353 (1991).
[129] I. G. Main, Geophys. J. Int. **111**, 531 (1992).
[130] C. G. Hatton, I. G. Main, and P. G. Meredith, J. Struct. Geol. **15**, 1485 (1993).
[131] I. G. Main, P. R. Sammonds, and P. G. Meredith, Geophys. J. Int. **115**, 367 (1993).
[132] Z. Reches and D. A. Lockner, Journal of Geophysical Research B: Solid Earth **99**, 18159 (1994).
[133] V. Lyakhovsky, Y. Ben-Zion, and A. Agnon, Journal of Geophysical Research B: Solid Earth **102**, 27635 (1997).
[134] I. G. Main, Geophys. J. Int. **142**, 151 (2000).
[135] X. L. Lei *et al.*, Geophys. Res. Lett. **27**, 1997 (2000).
[136] I. S. Colombo, I. G. Main, and M. C. Forde, J. Mat. Civ. Engrg. **15**, 280 (2003).
[137] J. Aue and J. T. M. D. Hosson, J. Mat. Sci. **33**, 5455 (1998).
[138] J. Weiss and D. Marsan, Science **299**, 89 (2003).
[139] L. C. Krysac and J. D. Maynard, Phys. Rev. Lett. **81**, 4428 (1998).
[140] D. A. Lockner *et al.*, Nature **350**, 39 (1991).
[141] K. R. Shah and J. F. Labuz, Journal of Geophysical Research B: Solid Earth **100**, 15527 (1995).
[142] J. F. Labuz and L. Biolzi, Int. J. Solids Structures **45**, 4191 (1998).
[143] A. R. Zang *et al.*, Geophys. J. Int. **135**, 1113 (1998).

[144] X. T. Feng and M. Seto, Geophys. J. Int. **136**, 275 (1999).
[145] K. Hayakawa, T. Nakamura, H. Yonezawa, and S. Tanaka, Mater. Transac. **45**, 3136 (2004).
[146] W. K. Zietlow and J. F. Labuz, Int. J. Rock Mech. Min. Sci. **35**, 291 (1998).
[147] T. Kanit *et al.*, Int. J. Solids Structures **40**, 3647 (2003).
[148] A. S. Balankin, O. Susarrey, and A. Bravo, Phys. Rev. E **64**, 066131 (2001).
[149] J. Rosti and M. J. Alava, preprint (2006).
[150] J. C. Anifrani, C. L. Floch, D. Sornette, and B. Souillard, J. Phys. I France **5**, 631 (1995).
[151] A. Johansen and D. Sornette, Eur. Phys. J. B **28**, 163 (2000).
[152] S. Suresh, *Fatigue of Materials* (Cambridge Univ. Press, Cambridge, 1998).
[153] S. Santucci, L. Vanel, and S. Ciliberto, Phys. Rev. Lett. **93**, 095505 (2004).
[154] H. Nechad, A. Helmstetter, R. E. Guerouma, and D. Sornette, Phys. Rev. Lett. **94**, 045501 (2005).
[155] M. Zaiser, Adv. Phys. **to appear**, (2006).
[156] P. Hähner, A. Ziegenbein, E. Rizzi, and H. Neuhäuser, Phys. Rev. B **65**, 134109 (2002).
[157] V. S. Deshpande, A. Needleman, and E. van der Giessen, Scripta Mat. **45**, 1047 (2001).
[158] S. Nemat-Nasser, Mech. Materials **31**, 493 (1999).
[159] A. Needleman and V. Tvergaard, Int. J. Fracture **101**, 73 (2000).
[160] R. Mahnken, Int. J. Plasticity **18**, 801 (2002).
[161] Z. P. Bazant *et al.*, Int. J. Fracture **113**, 345 (2002).
[162] J. D. Clayton and D. L. McDowell, Mech. Materials **36**, 799 (2004).
[163] M. Ostoja-Starzewski, Int. J. Plasticity **21**, 1119 (2005).
[164] J. C. Baret, D. Vandembroucq, and S. Roux, Phys. Rev. Lett. **89**, 195506 (2002).
[165] B. Kahng *et al.*, Phys. Rev. B **37**, 7625 (1988).
[166] A. Hansen, E. L. Hinrichsen, and S. Roux, Phys. Rev. B **43**, 665 (1991).
[167] I. Ootani, Y. Ohashi, K. Ohashi, and M. Fukuchi, J. Phys. Soc. Jpn. **61**, 1399 (1992).
[168] D. Hristopulos and T. Uesaka, Phys. Rev. E **70**, 064108 (2004).
[169] S. H. Chen and T. C. Wang, Acta Mech. **157**, 113 (2002).
[170] J. E. Bolander and N. Sukumar, Phys. Rev. B **71**, 094106 (2005).
[171] M. Alava, P. M. Duxbury, C. Moukarzel, and H. Rieger, in *Phase Transitions and Critical Phenomena* ( Academic Press, New York, 2000), Vol. 18.
[172] M. Kardar, G. Parisi, and Y. C. Zhang, Phys.Rev.Lett. **56**, 889 (1986).
[173] M. J. Alava, M. E. J. Karttunen, and K. J. Niskanen, Europhysics Letters **32**, 142 (1995).
[174] Y. S. Li and P. M. Duxbury, Phys. Rev. B **38**, 9257 (1988).
[175] S. Zapperi, A. Vespignani, and H. E. Stanley, Nature **388**, 658 (1997).
[176] P. K. V. V. Nukala and S. Simunovic, Phys. Rev. E **72**, 041919 (2005).
[177] D. R. Otomar, I. L. Menezes-Sobrinho, and M. S. Couto, Phys. Rev. Lett. **96**, 095501 (2006).
[178] L. Lamaignere, F. Carmona, and D. Sornette, Phys. Rev. Lett. **77**, 2738 (1996).
[179] A. Hansen, S. Roux, and H. J. Herrmann, J. Physique **50**, 733 (1989).
[180] S. Arbabi and M. Sahimi, Phys. Rev. B **47**, 695 (1993).
[181] M. Sahimi and S. Arbabi, Phys. Rev. B **47**, 703 (1993).
[182] P. K. V. V. Nukala, S. Zapperi, and S. Simunovic, Phys. Rev. E **71**, 066106 (2005).
[183] S. Feng and P. N. Sen, Phys. Rev. Lett. **52**, 216 (1984).
[184] G. N. Hassold and D. J. Srolovitz, Phys. Rev. B **39**, 9273 (1989).
[185] S. Roux and E. Guyon, J. Physique Lett. **46**, L999 (1985).
[186] H. J. Herrmann, A. Hansen, and S. Roux, Phys. Rev. B **39**, 637 (1989).
[187] P. K. V. V. Nukala, S. Simunovic, and M. N. Guddati, Int. J. Numer. Meth. Engng. **62**, 1982 (2005).
[188] Y. Kantor and I. Webman, Phys. Rev. Lett. **52**, 1891 (1984).
[189] M. Sahimi and J. D. Goddard, Phys. Rev. B **33**, 7848 (1986).
[190] L. Monette and M. P. Anderson, Modelling Simul. Mater. Sci. Eng. **2**, 53 (1994).
[191] X. P. Xu, A. Needleman, and F. F. Abraham, Modelling Simul. Mater. Sci. Eng. **5**, 489 (1997).
[192] W. Xuan, W. A. Curtin, and A. Needleman, Engineering Fracture Mechanics **70**, 1869 (2003).
[193] V. Tomar, J. Zhai, and M. Zhou, International Journal for Numerical Methods inEngineering **61**, 1894 (2004).
[194] V. Tomar and M. Zhou, Engineering Fracture Mechanics **72**, 1920 (2005).
[195] J. W. Chung, J. T. M. D. Hosson, and E. van der Giessen, Phys. Rev. B **64**, 064202 (2001).
[196] J. W. Chung and J. T. M. D. Hosson, Phys. Rev. B **66**, 064206 (2002).
[197] J. W. Chung, J. T. M. D. Hosson, and E. van der Giessen, Phys. Rev. B **65**, 094104 (2002).
[198] I. A. Kunin, *Elastic Media with Microstructure I* (Springer-Verlag, Berlin, Germany, 1982).
[199] H. Dai and G. Frantziskonis, Mechanics of Materials **18**, 103 (1994).

[200] G. N. Frantziskonis, A. A. Konstantinidis, and E. C. Aifantis, European Journal of Mechanics A/Solids **20**, 925 (2001).
[201] B. Budiansky and R. J. O'Connell, Int. J. Solids Structures **12**, 81 (1976).
[202] T. Belytschko and T. Black, International Journal for Numerical Methods in Engineering **45**, 601 (1999).
[203] A. Hillerborg, M. Modeer, and P. E. Petersson, Cement Concrete Res. **6**, 773 (1976).
[204] R. de Borst, L. J. Sluys, H.-B. Muhlhaus, and J. Pamin, Engng. Comput. **10**, 99 (1993).
[205] G. Pijaudier-Cabot and Z. P. Bazant, ASCE J. Eng. Mech. **113**, 1512 (1988).
[206] R. Peerlings, R. de Borst, W. A. M. Brekelmans, and M. G. D. Geers, International Journal for Numerical Methods in Engineering **39**, 3391 (1996).
[207] M. A. Gutierrez and R. de Borst, International Journal for Numerical Methods in Engineering **44**, 1823 (1999).
[208] J. Oliver, International Journal for Numerical Methods in Engineering **39**, 3601 (1996).
[209] G. N. Wells and L. J. Sluys, International Journal for Numerical Methods in Engineering **50**, 2667 (2001).
[210] J. C. Simo and M. S. Rifai, International Journal for Numerical Methods in Engineering **29**, 1595 (1990).
[211] C. Daux *et al.*, International Journal for Numerical Methods in Engineering **45**, 1741 (2000).
[212] J. M. Malenk and I. Babuska, Computer Methods in Applied Mechanics and Engineering **39**, 289 (1996).
[213] N. Sukumar and J. H. Prevost, International Journal for Numerical Methods in Engineering **40**, 7513 (2003).
[214] E. Budyn, G. Zi, N. Moes, and T. Belytschko, International Journal for Numerical Methods in Engineering **61**, 1741 (2004).
[215] R. Cafiero *et al.*, Phys. Rev. Lett. **79**, 1503 (1997).
[216] G. Caldarelli, R. Cafiero, and A. Gabrielli, Phys. Rev. E **57**, 3878 (1998).
[217] W. A. Curtin, J. Am. Ceram. Soc. **74**, 2837 (1991).
[218] W. A. Curtin and H. Scher, Phys. Rev. Lett. **67**, 2457 (1991).
[219] W. A. Curtin and H. Scher, Phys. Rev. B **45**, 2620 (1992).
[220] W. A. Curtin, J. Mech. Phys. Solids **41**, 217 (1993).
[221] S. Roux, A. Hansen, and E. L. Hinrichsen, Phys. Rev. Lett. **70**, 100 (1993).
[222] W. A. Curtin and H. Scher, Phys. Rev. Lett. **70**, 101 (1993).
[223] W. A. Curtin and H. Scher, Phys. Rev. Lett. **70**, 519 (1993).
[224] W. A. Curtin and H. Scher, Phys. Rev. B **55**, 12038 (1997).
[225] W. A. Curtin, M. Pamel, and H. Scher, Phys. Rev. B **55**, 12051 (1997).
[226] D. Sornette and C. Vanneste, Phys. Rev. Lett. **68**, 612 (1992).
[227] M. Minozzi, G. Caldarelli, L. Pietronero, and S. Zapperi, Eur. Phys. J. B **36**, 203 (2003).
[228] S. Vlastos, E. Liu, I. G. Main, and X.-Y. Li, Geophys. J. Int. **152**, 649 (2003).
[229] E. Bouchaud *et al.*, J. Mech. Phys. Solids **50**, 1703 (2000).
[230] S. Ramanathan, D. Ertas, and D. S. Fisher, Phys. Rev. Lett. **79**, 873 (1997).
[231] B. N. Cox, H. Gao, D. Gross, and D. Rittel, J. Mech. Phys. Solids **53**, 565 (2005).
[232] M. Marder and X. Liu, Phys. Rev. Lett. **71**, 2417 (1993).
[233] A. Karma, D. Kessler, and H. Levine, Phys. Rev. Lett. **87**, 045501 (2001).
[234] I. S. Aranson, V. A. Kalatsky, and V. M. Vinokur, Phys. Rev. Lett. **85**, 118 (2000).
[235] L. O. Eastgate *et al.*, Phys. Rev. E **65**, 036117 (2002).
[236] A. Karma and A. E. Lobkovsky, Phys. Rev. Lett. **92**, 245510 (2004).
[237] T. T. Rautiainen, M. J. Alava, and K. Kaski, Phys. Rev. E **51**, R2727 (1995).
[238] P. Heino and K. Kaski, Phys. Rev. B **54**, 6150 (1996).
[239] P. Heino and K. Kaski, Phys. Rev. E **56**, 4364 (1997).
[240] J. A. Moriarty *et al.*, Journal of Physics: Condensed Matter **14**, 2825 (2002).
[241] R. L. B. Selinger, Z.-G. Wang, W. M. Gelbart, and A. Ben-Saul, Phys. Rev. A **43**, 4396 (1991).
[242] R. L. B. Selinger, Z.-G. Wang, and W. M. Gelbart, J. Chem. Phys **95**, 9128 (1991).
[243] Z.-G. Wang, U. Landman, R. L. B. Selinger, and W. M. Gelbart, Phys. Rev. B **44**, 378 (1991).
[244] F. F. Abraham *et al.*, PNAS **99**, 5777 (2002).
[245] C. D. Lorentz and M. J. Stevens, Phys. Rev. E **68**, 021802 (2003).
[246] G. A. Buxton and A. C. Balazs, Phys. Rev. B **69**, 054101 (2004).
[247] E. Seppala, J. Belak, and R. Rudd, Phys. Rev. Lett. **93**, 245503 (2004).
[248] R. K. Kalia *et al.*, Phys. Rev. Lett. **78**, 2144 (1997).
[249] C. L. Rountree *et al.*, Annual Review of Materials Research **32**, 377 (2002).
[250] R. K. Kalia *et al.*, Int. J. Fracture **121**, 71 (2003).

[251] Q. Lu and B. Bhattacharya, Eng. Fract. Mech. **72**, 2037 (2005).
[252] P. C. Hemmer and A. Hansen, J. Appl. Mech. **59**, 909 (1992).
[253] A. Hansen and P. C. Hemmer, Phys. Lett. A **184**, 394 (1994).
[254] D. Sornette, J. Phys. I France **2**, 2089 (1992).
[255] P. M. Kloster, C. Hemmer, and A. Hansen, Phys. Rev. E **56**, 2615 (1997).
[256] D. G. Harlow and S. L. Phoenix, J. Composite Mater. **12**, 195 (1978).
[257] R. L. Smith, Proc. R. Soc. London A **372**, 179 (1980).
[258] R. L. Smith and S. L. Phoenix, J. Appl. Mech. **48**, 75 (1981).
[259] I. J. Beyerlein and S. L. Phoenix, J. Mech. Phys. Solids **44**, 1997 (1996).
[260] S. L. Phoenix, M. Ibnabdeljalil, and C.-Y. Hui, Int. J. Solids Structures **34**, 545 (1997).
[261] S. L. Phoenix and R. Ra, Acta Metall. Mater. **40**, 2813 (1992).
[262] S. J. Zhou and W. A. Curtin, Acta. Metall. Mater. **43**, 3093 (1995).
[263] P. L. Leath and P. M. Duxbury, Phys. Rev. B **49**, 14905 (1994).
[264] S. Zhang and E. Ding, Phys. Rev. B **53**, 646 (1996).
[265] D. Krajcinovic and M. A. G. Silva, Int. J. Solids Structures **18**, 551 (1982).
[266] B. Fabeny and W. A. Curtin, Acta Materialia **44**, 3439 (1996).
[267] R. C. Hidalgo, F. Kun, and H. J. Herrmann, Phys. Rev. E **65**, 032502 (2002).
[268] F. Kun, R. C. Hidalgo, H. J. Herrmann, and K. F. Pál, Phys. Rev. E **67**, 061802 (2003).
[269] F. Kun, S. Zapperi, and H. J. Herrmann, Eur. Phys. J. B **17**, 269 (2000).
[270] F. Raischel, F. Kun, and H. J. Herrmann, cond-mat/0601290 (2006).
[271] S. Roux, Phys. Rev. E **62**, 6164 (2000).
[272] R. Scorretti, S. Ciliberto, and A. Guarino, Europhys. Lett. **55**, 626 (2001).
[273] A. Politi, S. Ciliberto, and R. Scorretti, Phys. Rev. E **66**, 026107 (2002).
[274] R. da Silveira, Phys. Rev. Lett. **80**, 3157 (1998).
[275] S. Pradhan, A. Hansen, and P. C. Hemmer, Phys.Rev.Lett. **95**, 125501 (2005).
[276] S. Mahesh and S. L. Phoenix, Phys. Rev. E **69**, 026102 (2004).
[277] R. C. Hidalgo, Y. Moreno, F. Kun, and H. J. Herrmann, Phys. Rev. E **65**, 046148 (2002).
[278] S. Pradhan, B. K. Chakrabarti, and A. Hansen, Phys. Rev. E **71**, 036149 (2005).
[279] J. P. Sethna *et al.*, Phys. Rev. Lett. **70**, 3347 (1993).
[280] K. Dahmen and J. P. Sethna, Phys. Rev. B **53**, 14872 (1996).
[281] J. Sethna, K. A. Dahmen, and C. R. Myers, Nature **410**, 242 (2001).
[282] J. B. Rundle and W. Klein, Phys. Rev. Lett. **63**, 171 (1989).
[283] L. Golubovic and S. Feng, Phys. Rev. A **43**, 5223 (1991).
[284] L. Golubovic and A. Pedrera, Phys. Rev. E **51**, 2799 (1995).
[285] A. Buchel and J. P. Sethna, Phys. Rev. E **55**, 7669 (1997).
[286] S. Zapperi, P. Ray, H. E. Stanley, and A. Vespignani, Phys. Rev. Lett. **78**, 1408 (1997).
[287] S. Zapperi, P. Ray, H. E. Stanley, and A. Vespignani, Phys. Rev. E **59**, 5049 (1999).
[288] J. V. Andersen, D. Sornette, and K. W. Leung, Phys. Rev. Lett. **78**, 2140 (1997).
[289] M. Barthelemy, R. da Silveira, and H. Orland, Europhys. Lett. **57**, 831 (2002).
[290] R. Toussaint and S. R. Pride, Phys. Rev. E **71**, 046127 (2005).
[291] J. Schmittbuhl, S. Roux, J. P. Villotte, and K. J. Maloy, Phys. Rev. Lett. **74**, 1787 (1995).
[292] S. Ramanathan and D. S. Fisher, Phys. Rev. Lett. **79**, 877 (1997).
[293] S. Ramanathan and D. S. Fisher, Phys. Rev. B **58**, 6026 (1998).
[294] H. Gao and J. R. Rice, J. Appl. Mech. **56**, 828 (1989).
[295] D. Ertas and M. Kardar, Phys. Rev. E **49**, R2532 (1994).
[296] A. Rosso and W. Krauth, Phys. Rev. E **65**, 025101 (2002).
[297] J. Schmittbuhl and J. P. Villotte, Physica A **270**, 42 (1999).
[298] S. Zapperi, H. J. Herrmann, and S. Roux, Eur. Phys. J. B **17**, 131 (2000).
[299] J. A. Aström, M. J. Alava, and J. Timonen, Phys. Rev. E **62**, 2878 (2000).
[300] J. Schmittbuhl, A. Hansen, and G. G. Batrouni, Phys. Rev. Lett. **90**, 045505 (2003).
[301] E. Bouchbinder, J. Mathiesen, and I. Procaccia, Phys. Rev. Lett. **92**, 245505 (2004).
[302] P. L. Doussal, K. J. Wiese, E. Raphael, and R. Golestanian, cond-mat/0411652 (2004).
[303] A. Rosso, A. K. Hartmann, and W. Krauth, Phys. Rev. E **67**, 021602 (2003).
[304] L. H. Tang and H. Leshhorn, Phys. Rev. A **45**, R8309 (1992).
[305] S. V. Buldyrev *et al.*, 45 **R8313**, (1992).
[306] S. Prades *et al.*, Int. J. Sol. Struct. **42**, 637 (2004).
[307] D. Stauffer and A. Aharony, *Introduction to Percolation Theory* (Revised second edition, Taylor and Francis, 1994).
[308] P. Grassberger, Physica A **262**, 251 (1999).
[309] J. P. Clerc, V. A. Podolskiy, and A. K. Sarychev, Eur. Phys. J. B **15**, 507 (2000).

[310] C. Moukarzel, P. M. Duxbury, and P. L. Leath, Phys. Rev. Lett. **78**, 1480 (1997).
[311] S. Feng, B. I. Halperin, and P. N. Sen, Phys. Rev. B **35**, 1897 (1987).
[312] O. Stenull and H. K. Janssen, Phys. Rev. E **64**, 056105 (2001).
[313] M. J. Alava and C. F. Moukarzel, Phys. Rev. E **67**, 056106 (2003).
[314] S. Roux, A. Hansen, H. J. Herrmann, and E. Guyon, J. Stat. Phys. **52**, 237 (1988).
[315] C. F. Moukarzel, Int. J. Mod. Phys. C **9**, 887 (1998).
[316] P. M. Duxbury, P. L. Leath, and P. D. Beale, Phys. Rev. B **36**, 367 (1987).
[317] P. M. Duxbury, P. D. Beale, and P. L. Leath, Phys. Rev. Lett. **57**, 1052 (1986).
[318] E. J. Gumbel, *Statistics of Extremes* (Columbia University Press, New York, 2004).
[319] B. Sapoval, M. Rosso, and J. F. Gouyet, J. Physique Lett. (Paris) **46**, L149 (19985).
[320] A. Baldassarri, G. Gabrielli, and B. Sapoval, Europhys. Lett. **59**, 232 (2002).
[321] J. Schmittbuhl, A. Hansen, and G. G. Batrouni, Phys. Rev. Lett. **92**, 049602 (2004).
[322] M. J. Alava and S. Zapperi, Phys. Rev. Lett. **92**, 049601 (2004).
[323] J. Asikainen, S. Majaniemi, M. Dubé, and T. A. Nissila, Phys. Rev. Lett. **65**, 052104 (2002).
[324] A. Hansen and J. Schmittbuhl, Phys. Rev. Lett. **90**, 045504 (2003).
[325] P. K. V. V. Nukala, S. Simunovic, and S. Zapperi, J. Stat. Mech. P08001 (2004).
[326] L. de Arcangelis, A. Hansen, H. J. Herrmann, and S. Roux, Phys. Rev. B **40**, 877 (1989).
[327] D. Krajcinovic and A. Rinaldi, J. Appl. Mech. **72**, 76 (2005).
[328] M. Sahimi and S. Arbabi, Phys. Rev. B **47**, 713 (1993).
[329] M. Sahimi, Physics Reports **306**, 213 (1998).
[330] S. Arbabi and M. Sahimi, Phys. Rev. B **41**, 772 (1990).
[331] A. Delaplace, G. Pijaudier-Cabot, and S. Roux, J. Mech. Phys. Solids **44**, 99 (1996).
[332] L. de Arcangelis and H. J. Herrmann, Phys. Rev. B **39**, 2678 (1989).
[333] F. Reurings and M. J. Alava, Eur. Phys. J. B **47**, 85 (2005).
[334] S. Zapperi and P. K. V. V. Nukala, Int. J. Fracture (in press, 2006).
[335] V. I. Räisänen, E. T. Seppala, M. J. Alava, and P. M. Duxbury, Phys. Rev. Lett. **80**, 329 (1998).
[336] T. Ramstad *et al.*, Phys. Rev. E **70**, 036123 (2004).
[337] J. O. H. Bakke *et al.*, Physica Scripta **T106**, 65 (2003).
[338] P. K. V. V. Nukala, S. Zapperi, and S. Simunovic, unpublished (2006).
[339] P. M. Duxbury and P. L. Leath, Phys. Rev. Lett. **72**, 2805 (1994).
[340] P. M. Duxbury, S. G. Kim, and P. L. Leath, Materials Science and Engineering A **176**, 25 (1994).
[341] S. Nukala, P. K. V. V. Nukala, S. Simunovic, and F. Guess, Phys. Rev. E in press (2006).
[342] R. F. Smalley, D. L. Turcotte, and S. A. Solla, Journal of Geophysical Research **90**, 1894 (1985).
[343] W. I. Newman and A. M. Gabrielov, Int. J. Fracture **50**, 1 (1991).
[344] W. I. Newman *et al.*, Physica D **77**, 200 (1994).
[345] P. D. Beale and D. J. Srolovitz, Phys. Rev. B **37**, 5500 (1988).
[346] P. K. V. V. Nukala and S. Simunovic, Eur. Phys. J. B **37**, 91 (2004).
[347] E. T. Seppälä, V. I. Räisänen, and M. J. Alava, Phys. Rev. E **61**, 6312 (2000).
[348] Z. P. Bazant and A. Yavari, Eng. Fract. Mech. **72**, 1 (2005).
[349] A. Hansen, E. L. Hinrichsen, and S. Roux, Phys. Rev. Lett. **66**, 2476 (1991).
[350] S. Zapperi, P. K. V. V. Nukala, and S. Simunovic, Phys. Rev. E **71**, 026106 (2005).
[351] G. G. Batrouni and A. Hansen, Phys. Rev. Lett. **80**, 325 (1998).
[352] V. I. Räisänen, M. J. Alava, and R. M. Nieminen, Phys. Rev. B **58**, 14288 (1998).
[353] B. Skjetne, T. Helle, and A. Hansen, Phys. Rev. Lett. **87**, 125503 (2001).
[354] A. Parisi, G. Caldarelli, and L. Pietronero, Europhys. Lett. **52**, 304 (2000).
[355] G. Foltin *et al.*, Phys. Rev. E **50**, R639 (1994).
[356] A. Rosso *et al.*, Phys. Rev. E **68**, 036128 (2003).
[357] S. Zapperi, P. K. V. V. Nukala, and S. Simunovic, Physica A **357**, 129 (2005).
[358] G. Meacci, A. Politi, and M. Zei, Europhys. Lett. **66**, 55 (2004).
[359] G. Caldarelli, C. Castellano, and A. Petri, Phil. Mag. B **79**, 1939 (1999).
[360] G. Caldarelli, F. di Tolla, and A. Petri, Phys. Rev. Lett. **77**, 2503 (1996).
[361] J. Andersen and D. Sornette, cond-mat/0508549 (2005).
[362] R. Barrett *et al.*, *Templates for the Solution of Linear Systems: Building Blocks for Iterative Methods, 2nd Edition* (SIAM, Philadelphia, 1994).
[363] W. L. Briggs, V. E. Henson, and S. F. McCormick, *A Multigrid Tutorial, 2nd Edition* (SIAM, Philadelphia, 2000).
[364] G. G. Batrouni, A. Hansen, and M. Nelkin, Phys. Rev. Lett. **57**, 1336 (1986).
[365] G. G. Batrouni and A. Hansen, Journal of Statistical Physics **52**, 747 (1988).
[366] D. G. Luenberger, *Linear and Nonlinear Programming, 2nd Edition* (Addison-Wesley Publish-

ing Company, Reading, 1984).
[367] O'Shaughnessy and I. Procaccia, Phys. Rev. Lett. **54**, 455 (1985).
[368] O'Shaughnessy and I. Procaccia, Phys. Rev. A **32**, 3073 (1985).
[369] T. Chan, SIAM J. Sci. Stat. Comput. **9**, 766 (1988).
[370] R. H. Chan, SIAM J. Matrix Anal. Appl. **10**, 542 (1989).
[371] R. Chan and T. Chan, Numerical Linear Algebra Applications **1**, 77 (1992).
[372] R. H. Chan and M. K. Ng, SIAM Review **38**, 427 (1996).
[373] E. Tyrtyshnikov, SIAM J. Matrix Anal. Appl. **13**, 459 (1992).
[374] G. H. Golub and C. F. van Loan, *Matrix Computations* (The Johns Hopkins University Press, 1996).
[375] A. Gupta, M. Joshi, and V. Kumar, Technical Report RC 22038 (98932), IBM T. J. Watson Research Center, Yorktown Heights, NY (2001).
[376] P. R. Amestoy, I. S. Duff, J.-Y. L'Excellent, and J. Koster, SIAM Journal on Matrix Analysis and Applications **23**, 15 (2001).
[377] S. Toledo, D. Chen, and V. Rotkin, http://www.tau.ac.il∼stoledo/taucs/ (2001).
[378] P. K. V. V. Nukala and S. Simunovic, J. Phys. A: Math. Gen. **36**, 11403 (2003).
[379] T. A. Davis and W. W. Hager, SIAM J. Matrix Anal. Appl. **20**, 606 (1999).
[380] T. A. Davis and W. W. Hager, SIAM J. Matrix Anal. Appl. **22**, 997 (2001).
[381] P. K. V. V. Nukala and S. Simunovic, J. Phys. A: Math. Gen. **37**, 2093 (2004).